

Imperial College London

Blackett Laboratory

High Energy Physics

**Measurement of the  $W \rightarrow e\nu$  cross section  
with early data from the CMS experiment  
at CERN**

Nikolaos Rompotis

A thesis submitted to Imperial College London  
for the degree of Doctor of Philosophy  
and the Diploma of Imperial College.

January 2011



## Abstract

The Compact Muon Solenoid (CMS) is a general purpose detector designed to study proton-proton collisions, and heavy ion collisions, delivered by the Large Hadron Collider (LHC) at the European Laboratory for High Energy Physics (CERN). This thesis describes a measurement of the inclusive  $W \rightarrow e\nu$  cross section at 7 TeV centre of mass energy with  $2.88 \pm 0.32 \text{ pb}^{-1}$  of LHC collision data recorded by CMS between March and September 2010.

W boson decays are identified by the presence of a high- $p_T$  electron that satisfies selection criteria in order to reject electron candidates due to background processes. Electron selection variables are studied with collision data and found to be in agreement with expectations from simulation. A fast iterative technique is developed to tune electron selections based on these variables. Electron efficiency is determined from simulation and it is corrected from data using an electron sample from Z decays. The number of W candidates is corrected for remaining background events using a fit to the missing transverse energy distribution. The measured value for the inclusive W production cross section times the branching ratio of the W decay in the electron channel is:

$$\sigma(pp \rightarrow W + X) \times BR(W \rightarrow e\nu) = 10.04 \pm 0.10(\text{stat}) \pm 0.52(\text{syst}) \pm 1.10(\text{luminosity}) \text{ nb},$$

which is in excellent agreement with theoretical expectations.



## Declaration

This thesis describes research that has been done within the Compact Muon Solenoid (CMS) Collaboration and in which the author has made a significant contribution. In particular, the author had the responsibility of commissioning the electron identification variables (Chapter 5) and the development of the electron selection that was used in the measurement (Chapter 4). In addition, the author was developer and administrator of the official collaboration software package of the  $W \rightarrow e\nu$  and  $Z \rightarrow ee$  analyses and played an important role in the development of the electron efficiency measurement method using  $Z \rightarrow ee$  decays. The author had a significant contribution also in the  $W \rightarrow e\nu$  signal extraction and in particular in the development of a data-driven jet template and a method to extract the signal based on the extrapolation of the jet shape from a jet-rich region to a signal-rich region of the phase space. Finally, the author has contributed to the ECAL data certification that were used in the measurement.

Any research result that has been obtained by others and is discussed in this thesis is appropriately referenced and attributed to its original authors.

This thesis has not been submitted for another qualification to this or any other university. This thesis does not exceed the word limit specified in the College Regulations.

The copyright of this thesis rests with the author and no quotation from it or information derived from it may be published without the prior written consent of the author.

Nikolaos Rompotis



## Acknowledgements

There is a big number of people to whom I would like to express my gratitude for helping me to understand a little bit about research in physical sciences and complete a thesis.

First of all, I would like to thank my advisor, Chris Seez, with whom I had the honour to work all these years. I have definitely benefitted by his guidance, but also by his own way of viewing things. I hope that one day I will manage to imitate some of his ways.

I am very grateful to Georgios Daskalakis for the so many hours that we worked together and our almost daily conversations for such a long time. The exchange of ideas with him has been an important source of inspiration without which my thesis would have definitely been much different.

Many thanks to Jon Hays, David Futyan, Jim Virdee and Monica Vazquez for all their advice and support and to my co-students David Wardrope, Costas Petridis, Jad Marrouche, Christos Anastopoulos, Ioannis Florakis, Spyros Sotiriadis, Sotiris Paraskevopoulos, Spyros Argyropoulos and Eleni Petrakou for various physics discussions that helped me to revive my interest in physics and making my PhD more enjoyable. Special thanks to Claire Timlin for introducing me to particle physics research in such a gentle and supporting way and to Anne-Marie Magnan, Mat Noy, Greg Iles, Giannis Papaioannou and Paschalis Vichoudis for being good friends while I was in Geneva.

I would also like to thank Costas Fountas for recruiting me as an Imperial College PhD student, Geoff Hall and Jordan Nash for sending me on LTA at CERN and all the people with whom I have worked in the past and without them I would never have managed to complete a PhD thesis: Leo Resvanis, Athanasios Lahanas, Lev Kantorovitch, Dimitri Fratzeskakis and Aikaterini Chiou-Lahana.

I would like to acknowledge all the financial support that I have received from the Alexander S. Onassis Foundation, the Leventis Foundation and the Science and Technology Facilities Council (STFC).

Finally, I would like to thank my parents and my sister to whom I dedicate this thesis.

## Dedication

This thesis is dedicated to my parents and my sister.

*A little knowledge that acts is worth infinitely more than much knowledge that is idle.*

Khalil Gibran

(quoted in "*A Second Treasury by Khalil Gibran*", 1962)

# Contents

<b>Abstract</b>	<b>3</b>
<b>Declaration</b>	<b>5</b>
<b>Acknowledgements</b>	<b>7</b>
<b>1 Theoretical Background</b>	<b>29</b>
1.1 The Standard Model of Particle Physics . . . . .	29
1.1.1 Quantum Electrodynamics . . . . .	30
1.1.2 The Weak Interaction and the Electroweak Unification . . . . .	32
1.1.3 Higgs-Kibble Mechanism . . . . .	36
1.1.4 Standard Model and Beyond . . . . .	38
1.2 Physics of W and Z Bosons . . . . .	40
1.3 W Production in Proton-Proton Collisions . . . . .	46
<b>2 The CMS Experiment</b>	<b>49</b>
2.1 Introducing the Large Hadron Collider . . . . .	49

---

2.2	The CMS Experiment . . . . .	52
2.2.1	The Superconducting Solenoid Magnet . . . . .	53
2.2.2	The Inner Tracking System . . . . .	54
2.2.3	The Electromagnetic Calorimeter (ECAL) . . . . .	57
2.2.4	The Hadronic Calorimeter (HCAL) . . . . .	58
2.2.5	The Muon System . . . . .	59
2.2.6	The Trigger . . . . .	60
2.2.7	The CMS Computing Model . . . . .	63
2.3	The CMS ECAL . . . . .	64
2.3.1	Lead Tungstate Crystals . . . . .	64
2.3.2	ECAL Layout . . . . .	65
2.3.3	ECAL Photodetectors, Electronics and Trigger . . . . .	67
2.3.4	Calibration and Performance . . . . .	68
<b>3</b>	<b>Electrons in CMS</b>	<b>72</b>
3.1	Electron Trigger and Electron Reconstruction in CMS . . . . .	72
3.1.1	Triggering on Electrons in CMS . . . . .	73
3.1.2	Electron Reconstruction in CMS . . . . .	74
3.2	Backgrounds to Prompt Electrons . . . . .	77
3.3	Electron Identification Variables . . . . .	79
3.4	Simulation of Events Containing Electron Candidates . . . . .	83

---

3.4.1	Simulation of Jet Background from Light Flavour Quarks and Gluons . . . . .	84
<b>4</b>	<b>Electron Selection</b>	<b>87</b>
4.1	Classification in the Context of Classical Statistics . . . . .	87
4.1.1	Cut-Based Analysis and Cut Tuning . . . . .	89
4.2	The Iterative Technique . . . . .	91
4.3	Selection Tuning with the Iterative Technique . . . . .	97
<b>5</b>	<b>Electron Commissioning with Collision Data</b>	<b>103</b>
5.1	Data Samples . . . . .	103
5.2	Electrons and Electron Identification in Data . . . . .	105
5.3	Future prospects with the Iterative Technique . . . . .	113
<b>6</b>	<b><math>W \rightarrow e\nu</math> Cross Section Measurement at CMS</b>	<b>117</b>
6.1	Introduction . . . . .	117
6.2	Samples and Event Selection . . . . .	118
6.3	Acceptance . . . . .	119
6.4	Efficiency Determination . . . . .	122
6.4.1	The Tag-and-Probe Method . . . . .	123
6.4.2	Efficiency for the $W \rightarrow e\nu$ Electron Selection . . . . .	125
6.5	Luminosity . . . . .	128

6.6	Signal Extraction . . . . .	129
6.7	Results . . . . .	135
<b>7</b>	<b>Summary and Conclusions</b>	<b>138</b>
	<b>Bibliography</b>	<b>142</b>
<b>A</b>	<b>Electron Candidates after WP80 and <math>\cancel{E}_T &gt; 30</math> GeV</b>	<b>153</b>
<b>B</b>	<b>Electron Candidates after WP80</b>	<b>160</b>

# List of Tables

3.1	Seed matching windows definitions used in electron reconstruction (offline) and in the “start-up” trigger configuration. Asymmetric $\phi$ windows are shown here for the positive charge hypothesis. In the offline reconstruction the first window in $\phi$ is (supercluster) $E_T$ -dependent and it is shown for an electron with $E_T$ 10 and 35 GeV. . . . .	76
3.2	Summary of the simulated samples details that were used for this study. PYTHIA6 cross sections ( $\sigma$ ) for electroweak processes are scaled to the POWHEG cross sections in the data-simulation comparison plots. . .	83
4.1	Sets of cuts derived from simulated data using the Iterative Technique. See text for details. . . . .	101
5.1	HLT trigger paths together with their Level-1 (L1) trigger seed $E_T$ thresholds for different run ranges used for the first $2.88 \text{ pb}^{-1}$ of data taking. The integrated luminosity ( $\mathcal{L}$ ) for data corresponding to different run ranges are quoted separately. The total integrated luminosity is $2.88 \text{ pb}^{-1}$ .	104
5.2	Summary of the requested criteria on the single electron event sample.	105
6.1	Summary of the theoretical uncertainties in the acceptance calculation.	121

6.2	The calculated values for the $W \rightarrow e\nu$ signal acceptance ( $A_W$ ) from the simulation. The statistical uncertainties on these numbers are negligible ( $< 0.2\%$ ). . . . .	122
6.3	Results from the efficiency calculation with the tag-and-probe method. Quoted uncertainties are of statistical nature only apart from the last row. The combined ECAL efficiency (barrel+endcaps) is calculated by re-weighting the efficiencies with the acceptance values quoted in Table 6.2. . . . .	126
6.4	Efficiency of the W selection criteria calculated directly from $W \rightarrow e\nu$ simulated events for the ECAL barrel, endcaps and combined. Statistical uncertainties on these numbers are negligible. . . . .	127
6.5	Electroweak contributions to the backgrounds in the $W \rightarrow e\nu$ cross section measurement as estimated from simulation. . . . .	133
6.6	Numerical values of the terms that appear in Eq. (6.8). The uncertainties shown here include both statistical and systematic uncertainties apart from $N_W$ , where the uncertainty is purely statistical. . . . .	135
6.7	List of systematic uncertainties for the $W \rightarrow e\nu$ cross section measurement as a percentage of the final cross section result. The luminosity error is considered separately and is not shown here. . . . .	136

# List of Figures

1.1	The cross section of electron-positron annihilation to hadrons as predicted by SM (continuous line) and as it is measured by various experiments [22].	44
1.2	The cross section of hadron production around the Z resonance from LEP [34]. The continuous curves indicate the predicted cross section for 2, 3 and 4 neutrino species with SM couplings and negligible mass. . .	44
1.3	Precision measurements of various observables. The experimental results are compared to the Standard Model values, which are derived by a fit that includes further observables. The difference of the fit value from the measurement (pull) is also quoted. For more details see [23]. . . . .	45
1.4	WW production cross section as measured at LEP with the OPAL detector (points) compared with the SM expectation (line). The shaded error shows the theoretical uncertainty. For more details see [35]. . . .	46
1.5	Higgs mass restrictions from measurements of the W and top quark masses in (a) [5] and limits from direct searches at LEP and the Tevatron experiments and expected values from EWK precision tests [23]. . . . .	47
2.1	The LHC accelerator complex. . . . .	50

2.2	The integrated luminosity delivered by the LHC with 7 TeV proton-proton collisions from March till November 2010 as a function of time (red line). In the same plot it is shown also which part of these data were actually recorded by the CMS detector (blue line). . . . .	51
2.3	The layout of the CMS detector. It is 21.6 m long and has a diameter of 14.6 m. Its total weight is 12 500 t. (reproduced from [46]). . . . .	52
2.4	The CMS inner tracking system layout (from [53]). . . . .	54
2.5	Transverse momentum resolution for single muons with transverse momentum 1, 10 and 100 GeV (reproduced from [46]). . . . .	56
2.6	Tracking performance with collision data. (a) Reconstruction of the $\Lambda^0$ resonance with 2009 collision data (from [54]). (b) Transverse impact parameter resolution with 7 TeV data (from [55]). . . . .	56
2.7	Jet transverse energy resolution in (a) and missing transverse energy resolution in (b) with CMS collision data. For more details see [58]. . . . .	59
2.8	Muon transverse momentum ( $p_T$ ) resolution as a function of $p_T$ using the muon system only, the inner tracking only, and both. In (a) the resolution is plotted for muons in $ \eta  < 0.8$ and in (b) for muons in $1.2 <  \eta  < 2.4$ . Plot reproduced from [46] . . . . .	60
2.9	The di-muon invariant mass distribution (black points) as measured at CMS with $2.9 \text{ pb}^{-1}$ of data compared with a simulated $Z \rightarrow \mu\mu$ di-muon invariant mass distribution [72]. . . . .	61
2.10	Proton-proton cross sections for various processes in centre of mass energy relevant to LHC physics. Reproduced from [50]. . . . .	62
2.11	Map showing the geographical distribution of CMS Tier-1 (red dots) and Tier-2 (blue squares) centers. Reproduced from [56]. . . . .	64

- 2.12 The CMS ECAL layout. The detector is 7.8 m long and has a diameter of 3.5 m. The total crystal volume is 8.14 m<sup>3</sup> in the ECAL barrel and 3.04 m<sup>3</sup> in the ECAL endcaps. This corresponds to a total crystal weight of about 90 t. . . . . 66
- 2.13 Cross sectional view of the upper part of the ECAL. The component on the left-hand side of this figure is an ECAL supermodule, which is about 3 m in length and 0.5 m in height. On the right-hand side of the figure the ECAL barrel-endcaps transition region is visible along with the upper part of the ECAL endcaps and the ECAL preshower. . . . . 66
- 2.14 The ECAL supermodule energy resolution in the test beam (from [46]). The upper continuous curve corresponds to events taken with a 20×20 mm<sup>2</sup> trigger and reconstructed using a containment correction that is described in more detail in [46]. The lower dashed curve corresponds to events selected to fall within a 4×4 mm<sup>2</sup> region. The energy is measured in a 3×3 crystal array with electrons impacting the central crystal. . . . . 69
- 2.15 ECAL performance demonstrated with the measurement of physical processes. (a) The  $\pi^0 \rightarrow \gamma\gamma$  resonance for photons reconstructed in the ECAL barrel [102]. (b) The  $Z \rightarrow ee$  resonance [72]. . . . . 70
- 3.1 The CMS Inner Tracking System material budget in radiation lengths as a function of the pseudorapidity ( $\eta$ ) from [46]. . . . . 75
- 3.2 Dist is the two dimensional distance between points B1 and B2 in the x-y plane as seen above. At these points, the two tracks from the photon conversion are parallel. Dist is defined to be negative when the two tracks overlap, and is positive otherwise. . . . . 82

- 4.1 Schematic representation of the approximation to the steepest descend method that is discussed in Section 4.1.1. Each point in this 2-dimensional grid represents a pair of cut values. The ideal path that minimises Eq. (4.3) is the curved line. The approximation described in the text tries to approximate this line by moving one variable at a time creating a line composed of straight segments. . . . . 91
- 4.2 Tests of the Iterative Technique performance. (a) The performance of selections obtained by the Iterative Technique (continuous red line) is compared to the performance of selections optimised with a genetic algorithm implementation (black points connected with straight segments). (b) Performance of the iterative technique selections versus randomly generated points. See text for details. . . . . 93
- 4.3 Tests of the Iterative Technique performance. A single set of cuts has been chosen and the cuts on a particular variable are moved generating the dashed line connecting the red triangles. These points perform worse than the Iterative Technique derived selections (back round markers) as expected. In (a) the variable is ECAL isolation for EB, whereas in (b) it is the  $\Delta\eta_{in}$  for EE. . . . . 95
- 4.4 Dependence of the performance of the Iterative Technique on the parameters of the method. (a) Variation of the step in background rejection. (b) variation of initial cut values. . . . . 97
- 4.5 Application of the Iterative Technique on simulated electron samples with different cuts in electron supercluster  $E_T$ . (a) Comparison of tunings starting from different  $E_T$  cuts. (b) Application of selections tuned with 25 GeV cut on samples with a 20 GeV cut (markers connected with straight line segments) and comparison with selections tuned on samples with a 20 GeV cut. Both plots use the tight conversion rejection criteria. 99

- 4.6 The performance of selection tuning with simulated samples for selections used on data. The markers indicate the selections of Table 4.1 without the  $\Delta\eta_{in}$  cut applied in the ECAL endcap region. Lines show the Iterative Technique tuning curves that are obtained including the  $\Delta\eta_{in}$  in the ECAL endcaps. The loosest working point (WP95) was chosen from the curve with loose conversion rejection, WP90 and WP85 from the medium conversion rejection curve and the rest from the tight conversion curve. 100
- 5.1 The distribution of the event transverse missing energy ( $\cancel{E}_T$ ) in (a) and the electron candidate  $E_T$  in (b) for all events and electrons in the single electron sample fulfilling the criteria in Table 5.2. Black points correspond to collision data and histograms to simulated samples. . . . . 106
- 5.2 (a) The distribution of transverse missing energy ( $\cancel{E}_T$ ) for all events in the single electron sample that satisfy the criteria in Table 5.2 and pass a jet veto. (b) The electron candidate  $E_T$  distribution of the events shown in (a) that pass in addition a missing transverse energy cut:  $\cancel{E}_T > 30$  GeV. Black points correspond to collision data and histograms to simulated samples. . . . . 107
- 5.3 The  $\Delta\phi_{in}$  distribution for reconstructed electrons in the ECAL barrel (a) and ECAL endcaps (b) for events that pass a jet veto and a  $\cancel{E}_T$  cut. Black points correspond to collision data and histograms to simulated samples. . . . . 108

5.4	(a) The $\Delta\eta_{in}$ mean value as a function of supercluster $\phi$ for electrons reconstructed in the ECAL endcap ( $z > 0$ ). The vertical axis error bars correspond to the standard deviation of the $\Delta\eta_{in}$ values in that $\phi$ bin. The yellow band corresponds to the expectation from simulation. (b) The distribution of $\Delta\eta_{in}$ for reconstructed electrons for the same sample. Black points correspond to collision data and histograms to simulated samples. The events in both plots pass a jet veto and a $\cancel{E}_T$ cut.	109
5.5	$\cancel{E}_T$ distributions of the events in the single electron sample of Section 5.1 after the application of the electron selections of Table 4.1. Black points correspond to collision data and histograms to simulated samples. . .	110
5.6	$E_T$ and supercluster $\eta$ distributions of electron candidates that pass WP80 and they are contained in events with high $\cancel{E}_T$ . Black points correspond to collision data and histograms to simulated samples. . .	111
5.7	$\Delta\phi_{in}$ distribution for electrons reconstructed in (a) the ECAL barrel and (b) the ECAL endcaps for electrons passing the WP80 cuts on all the variables apart from $\Delta\phi_{in}$ . A further requirement of $\cancel{E}_T > 30$ GeV is applied. Black points correspond to collision data and histograms to simulated samples. . . . .	112
5.8	ECAL isolation distribution for electrons reconstructed in the ECAL barrel (a) and ECAL endcaps (b) for electrons passing the WP80 cuts apart on all the variables from the ECAL isolation. Black points correspond to collision data and histograms to simulated samples. . . . .	112
5.9	Test of the data driven set up for the Iterative Technique with simulated data. See text for details. . . . .	114

- 5.10 Test of the Iterative Technique with real data. Filled red rectangles correspond to the simulation defined selections of Table 4.1. Signal efficiency ( $\epsilon_{Signal}$ ) is measured from data using electrons from  $Z$  decays (see Section 6.4) and the background efficiency ( $\epsilon_{Bkg}$ ) is taken simply as the efficiency in the background sample obtained with the  $\cancel{E}_T < 20$  GeV cut. The integrated luminosity of the data sample used is  $850 \pm 94$  nb $^{-1}$ . See text for details. . . . . 115
- 6.1 (a) The electron transverse energy,  $E_T$ , and (b) the supercluster pseudorapidity,  $\eta_{sc}$ , distributions of the  $W \rightarrow e\nu$  selected candidate events. . . . . 119
- 6.2 The difference between the efficiency of selections calculated directly from  $W \rightarrow e\nu$  simulated events ( $\epsilon_W$ ) and the tag-and-probe method ( $\epsilon_{TP}$ ) on simulated  $Z \rightarrow ee$  events. Black points connected with straight line segments refer to the pure tag-and-probe result. The remaining lines show the tag-and-probe result after a rescaling of the kinematic distributions of the probe electrons in bins of  $\eta$ - $E_T$  such that they agree with the ones of the  $W$  electrons. The binning in  $\eta$ - $E_T$  becomes finer and finer with 7, 10, 13 and 20  $\eta$  bins and 8, 10, 15 and 20  $E_T$  bins respectively. . . . . 124
- 6.3 Example of fits to the tag-probe invariant mass distribution for the efficiency calculation. The probes are reconstructed electrons. On the left (right) the distribution of the probe electrons that pass (fail) the WP80 selection cuts is shown. In the plots data are shown with black points, the signal template with a black line, the background template with a red line and the combined result of the fit with a blue line. . . . . 125

6.4	The $\cancel{E}_T$ template based on a modified Rayleigh function of Eq. 6.6 fitted to a distribution derived from data by inverting track-ECAL cluster matching electron identification cuts. . . . .	130
6.5	The $\cancel{E}_T$ distribution for the selected $W \rightarrow e\nu$ candidate sample. The markers represent the data. The component contributions of the fitted template of Eq. (6.7). are also shown. . . . .	133
6.6	(a) Comparison of the $\cancel{E}_T$ shape of the jet enriched sample described in the text (black points) with the jet distribution after the WP80 selection cuts (histogram). Both distributions are derived from simulated jet events. (b) The data $\cancel{E}_T$ distribution after the WP80 selection criteria (black points). The result of the maximum likelihood fit is shown in histograms with the contribution of each component shown. The fit is performed in bins of 1 GeV. . . . .	134
A.1	Distributions of shower shape and track-supercluster matching variables used in electron identification for electrons in the ECAL barrel that pass the cuts of the WP80 selection excluding the cut on the variable that is being plotted. A further requirement of $\cancel{E}_T > 30$ GeV is applied. See Section 5.2 for details. . . . .	154
A.2	Distributions of $\Delta \cot \theta$ and Dist variables for electrons with a conversion partner track candidate in the ECAL barrel that pass the cuts of the WP80 selection without the conversion rejection criterion based on the identification of a conversion partner track. A further requirement of $\cancel{E}_T > 30$ GeV is applied. See Section 5.2 for details. . . . .	155

- A.3 Distributions of isolation variables and missing inner hits used in electron identification for electrons in the ECAL barrel that pass the cuts of the WP80 selection excluding the cut on the variable that is being plotted. A further requirement of  $\cancel{E}_T > 30$  GeV is applied. See Section 5.2 for details. . . . . 156
- A.4 Distributions of shower shape and track-supercluster matching variables used in electron identification for electrons in the ECAL endcaps that pass the cuts of the WP80 selection excluding the cut on the variable that is being plotted. The  $\Delta\eta_{in}$  variable is corrected using an *ad hoc* correction, which, however, is not perfect. A further requirement of  $\cancel{E}_T > 30$  GeV is applied. See Section 5.2 for details. . . . . 157
- A.5 Distributions of  $\Delta \cot \theta$  and Dist variables for electrons with a conversion partner track candidate in the ECAL endcaps that pass the cuts of the WP80 selection without the conversion rejection criterion based on the identification of a conversion partner track. A further requirement of  $\cancel{E}_T > 30$  GeV is applied. See Section 5.2 for details. . . . . 158
- A.6 Distributions of isolation variables and inner missing hits used in electron identification for electrons in the ECAL endcaps that pass the cuts of the WP80 selection excluding the cut on the variable that is being plotted. A further requirement of  $\cancel{E}_T > 30$  GeV is applied. See Section 5.2 for details. . . . . 159

- B.1 Distributions of shower shape and track-supercluster matching variables used in electron identification for electrons in the ECAL barrel that pass the cuts of the WP80 selection excluding the cut on the variable that is being plotted. The discrepancy in the high values of  $\sigma_{i\eta i\eta}$  is due to the trigger path that is used in the data, which implements a loose cut, as far as prompt electrons are concerned, on this variable (see Section 5.1). This cut is not applied on the simulated data. See Section 5.2 for details. 161
- B.2 Distributions of  $\Delta \cot \theta$  and Dist variables for electrons with a conversion partner track candidate in the ECAL barrel that pass the cuts of the WP80 selection without the conversion rejection criterion based on the identification of a conversion partner track. See Section 5.2 for details. 162
- B.3 Distributions of isolation variables and missing inner hits used in electron identification for electrons in the ECAL barrel that pass the cuts of the WP80 selection excluding the cut on the variable that is being plotted. See Section 5.2 for details. . . . . 163
- B.4 Distributions of shower shape and track-supercluster matching variables used in electron identification for electrons in the ECAL endcaps that pass the cuts of the WP80 selection excluding the cut on the variable that is being plotted. The  $\Delta\eta_{in}$  variable is corrected using an *ad hoc* correction, which, however, is not perfect. The discrepancy in the high values of  $\sigma_{i\eta i\eta}$  is due to the trigger path that is used in the data, which implements a loose cut, as far as prompt electrons are concerned, on this variable (see Section 5.1). This cut is not applied on the simulated data. See Section 5.2 for details. . . . . 164

B.5	Distributions of $\Delta \cot \theta$ and Dist variables for electrons with a conversion partner track candidate in the ECAL endcaps that pass the cuts of the WP80 selection without the conversion rejection criterion based on the identification of a conversion partner track. See Section 5.2 for details.	165
B.6	Distributions of isolation variables and inner missing hits used in electron identification for electrons in the ECAL endcaps that pass the cuts of the WP80 selection excluding the cut on the variable that is being plotted. See Section 5.2 for details.	166



# Chapter 1

## Theoretical Background

*It is a capital mistake to theorise before one has data. Insensibly one begins to twist facts to suit theories instead of theories to suit facts.*

“A Scandal in Bohemia”, Sir Arthur Conan Doyle

In this introductory chapter, a short overview of the theoretical foundations of the research related to this thesis is presented, starting from a general description of the Standard Model of particle physics and continuing with the physics of the W and Z bosons.

### 1.1 The Standard Model of Particle Physics

The Standard Model of particle physics (SM) provides a theoretical framework for the description of almost all subnuclear phenomena that occur on an energy scale up to  $\mathcal{O}(100)$  GeV<sup>1</sup>. This section is devoted to a description of the historical development and the mathematical structure of this theory.

---

<sup>1</sup>The word “almost” reflects the fact that the neutrino sector of the theory has still many unresolved issues: the determination of the neutrino mixing angles and possibly the existence or not of CP violation in the neutrino sector, the mass of the neutrino species and the answer to the question whether neutrinos are Dirac or Majorana particles.

### 1.1.1 Quantum Electrodynamics

The development of SM had historically started with the effort to describe the spectra of the atoms and the nuclei. The physical processes that are related to the atom should be described in the framework of quantum mechanics as one can see from the fact that the electrons, which in classical terms are revolving around the nucleus, do not suffer radiative losses that would render the atom unstable. Calculations of the atomic spectra based on the non-relativistic Schroedinger equation were proven to give a good description of the observations. However, certain details such as the fine and hyper-fine structure of the atomic spectra were not properly described in that framework. This fact was not unanticipated, since a proper treatment would involve a proper combination of classical electromagnetism, which is a relativistic theory, and quantum mechanics. Pursuit of this direction led to the development of Dirac's *relativistic quantum mechanics*, which proved capable of describing many previously unexplained details of the spectra. Despite its success, relativistic quantum mechanics could not form the bases of the final theory of electromagnetic interactions in the microcosm. Experimenters were studying the electron magnetic moment,  $\vec{\mu}$ :

$$\vec{\mu} = -g \frac{e}{2m} \vec{S}, \quad (1.1)$$

where  $m$  is the electron mass,  $e$  is the electron charge,  $\vec{S}$  is electron spin and  $g$  the gyromagnetic ratio. The relativistic quantum mechanical prediction for the gyromagnetic ratio is precisely 2, whereas there is experimental evidence of a small deviation from that value. Another discrepancy of Dirac's theory with experiment is the so-called *Lamb shift*: a small energy difference between the energy levels  $^2S_{1/2}$  and  $^2P_{1/2}$  of the hydrogen atom. The difference was first measured by Lamb and Retherford in 1947 [1], whereas according to relativistic quantum mechanics no difference should exist. These discrepancies paved the way for the development of *quantum field theory* (QFT) and a theory of electromagnetic interactions based on QFT, which is known as *quantum elec-*

*rodynamics* (QED). QED not only solved Dirac's theory problems, but also became one of the theories with the most precisely verified predictions.

QED is a gauge theory, which means that the electromagnetic interaction is introduced in a way that respects gauge invariance. The normal Dirac lagrangian:

$$\mathcal{L} = \bar{\psi}(i\partial - m)\psi, \quad (1.2)$$

where  $\psi$  is the electron field,  $\bar{\psi}$  its conjugate and  $m$  the electron mass, is not invariant under the local gauge transformation:

$$\psi \rightarrow \psi' = e^{-i\alpha(x)}\psi. \quad (1.3)$$

However, the introduction of the gauge field  $A_\mu$  through the *minimal coupling*:

$$D_\mu = \partial_\mu + ieA_\mu, \quad (1.4)$$

will respect the symmetry as long as  $A_\mu$  transforms like:

$$A_\mu \rightarrow A_\mu + \frac{1}{e}\partial_\mu\alpha. \quad (1.5)$$

Hence, the coupling between electrons and the gauge field  $A_\mu$ , which is the electromagnetic field, arises naturally when we require the invariance under local gauge transformations.

The complete QED lagrangian includes also the electromagnetic stress tensor  $F_{\mu\nu} \equiv \partial_\mu A_\nu - \partial_\nu A_\mu$ , which can be also shown to be gauge invariant. The final form of the lagrangian is:

$$\mathcal{L} = -\frac{1}{4}F_{\mu\nu}F^{\mu\nu} + \bar{\psi}(i\partial - e\mathcal{A} - m)\psi \quad (1.6)$$

### 1.1.2 The Weak Interaction and the Electroweak Unification

One of the seminal developments in fundamental physics during the early 20th century was the discovery of interactions in nature that are different from electromagnetism and gravity.

The discovery of the continuous spectrum of beta decay in 1913 by Chadwick [2] and the proposal of the existence of the neutrino by Pauli in 1930 [3] required the existence of a new kind of force in nature. That force was dubbed the *weak force*, due to the fact that it appeared to be weaker than the electromagnetic force.

In order to elucidate this statement the following example will be given [4]. Neutral Sigma Hyperon decays can decay to a channel that can be described electromagnetically, i.e. QED can be used to calculate the decay rate:

$$\Sigma^0 \rightarrow \Lambda + \gamma. \quad (1.7)$$

The decay time for this channel is found to be  $\sim 10^{-19}$  sec, which is a typical time scale for electromagnetic interactions. The charged hyperon, however, can decay in the channel:

$$\Sigma^- \rightarrow n + \pi^-, \quad (1.8)$$

with a decay time for this reaction of  $\sim 10^{-10}$  s. This decay is performed through the intervention of the weak force, as detailed calculations can also confirm. In general, the weak force is responsible for the decay of particles with abnormally long life times with respect to the typical time scale of electromagnetic interactions. Such particle decays are the neutron decay, strange particle decays (like  $\Sigma$ ), the muon and charged pion decay etc (see [5] for more decay channels).

The first attempt to understand the weak interactions was in the context of beta decay. Fermi in 1934 [6] proposed a 4-body contact interaction among the electron,  $e$ ,

the neutrino  $\nu$ , the proton,  $p$  and the neutron  $n$ , that is described by the following lagrangian:

$$\mathcal{L}_{weak} = \frac{G_F}{\sqrt{2}} (\bar{\psi}_p \gamma_\mu \psi_n) (\bar{\psi}_e \gamma^\mu \psi_\nu). \quad (1.9)$$

In this equation  $G_F$  is the *Fermi constant*, which can be calculated from muon decay life time measurements.

The Fermi lagrangian of Eq. (1.9) suffers from the fact that is not gauge invariant and hence non-renormalizable. This has the important consequence that the theory ceases to give predictions at a scale of  $\mathcal{O}(100)$  GeV. The theory is rescued with the introduction of the concept of *intermediate vector gauge bosons*, which mediate the weak force just as the photons mediate the electromagnetic force. The fact that the gauge bosons are massive is reflected in the observation that the weak force is weaker than the electromagnetic force. One other very important aspect of the theory is that it becomes possible to have a unified description of both the electromagnetic and the weak interactions such that the electromagnetic and the weak coupling constants are not independent. This is known as *electroweak unification*.

The gauge group that was found to be successful in describing the experimental properties of the weak and the electromagnetic forces is a cross product of two groups<sup>2</sup>:

$$SU(2)_L \otimes U(1)_Y. \quad (1.10)$$

The first of them has the index “ $L$ ” to denote that the  $SU(2)$  symmetry refers only to left handed particle components and “ $Y$ ” denotes the weak hypercharge. The gauge fields that correspond to these groups are denoted:

$$SU(2)_L \longrightarrow W_\mu^1, W_\mu^2, W_\mu^3 \quad (1.11)$$

---

<sup>2</sup>An introduction to Lie groups and other group theoretical concepts used in particle physics can be found in Ref. [10].

$$U(1)_Y \longrightarrow B_\mu. \quad (1.12)$$

Particles are organised in left handed doublets and right handed singlets, reflecting the observational fact that there are no right handed neutrinos<sup>3</sup>. For example, in the case of the electron and its neutrino we have

$$L = \begin{pmatrix} \nu_L \\ e_L \end{pmatrix}, \quad R = (e_R). \quad (1.13)$$

The neutrino,  $\nu$ , of the left handed doublet has the third SU(2) isospin projection  $T_3 = +1/2$ . The corresponding value for the electron,  $e$ , is  $T_3 = -1/2$ . Both components of the left handed doublet have hypercharge -1, whereas for the right handed doublet the corresponding value is -2. There is a relationship among the isospin, the hypercharge and the electric charge ( $Q$ ), also known as the Gell-Mann-Nishijima relation:

$$Q = T_3 + \frac{1}{2}Y. \quad (1.14)$$

In order to write the lagrangian for this theory, the covariant derivative definition and the gauge bosons' stress tensors are needed. The covariant derivative for the theory is defined as

$$D_\mu L = \left( \partial_\mu + i\frac{g}{2}\tau^i W_\mu^i + i\frac{g'}{2}Y B_\mu \right) L, \quad (1.15)$$

$$D_\mu R = \left( \partial_\mu + i\frac{g'}{2}Y B_\mu \right) R, \quad (1.16)$$

where  $g$  and  $g'$  are the coupling constants associated with the symmetry group and  $\tau^i$  the SU(2) generators.

The gauge field stress tensors are denoted by  $W_{\mu\nu}^i$  and  $B_{\mu\nu}$  and they are defined as

---

<sup>3</sup>This is known not to be true, since neutrinos are massive particles, as the observation of neutrino oscillations suggest. The inclusion of massive neutrinos is the first evidence for physics beyond the Standard Model, however, the theory related to this very interesting topic is beyond of the scope of this thesis and in the following neutrinos will be considered as massless particles.

follows:

$$W_{\mu\nu}^i \equiv \partial_\mu W_\nu^i - \partial_\nu W_\mu^i + g\epsilon^{ijk}W_\mu^jW_\nu^k, \quad (1.17)$$

$$B_{\mu\nu} = \partial_\mu B_\nu - \partial_\nu B_\mu, \quad (1.18)$$

where  $\epsilon$  is the fully antisymmetric (pseudo)tensor.

Finally, we are ready to write the lagrangian of the theory in the case of one lepton family:

$$\mathcal{L}_{ewk} = \bar{R}i\not{D}R + \bar{L}i\not{D}L - \frac{1}{4}W_{\mu\nu}^iW^{i\mu\nu} - \frac{1}{4}B_{\mu\nu}B^{\mu\nu}. \quad (1.19)$$

This lagrangian is considerably more complicated than the case of simple QED lagrangian of Eq. (1.6). The charged gauge bosons of the weak interactions can be defined such that the Fermi lagrangian of Eq. (1.9) is the low energy limit of Eq. (1.19). In this limit:

$$W_\mu^\pm = \frac{1}{\sqrt{2}}(W_\mu^1 \mp W_\mu^2), \quad (1.20)$$

and the coupling constant  $g$  is related to the Fermi constant  $G_F$  with the formula:

$$\frac{g^2}{4\sqrt{2}} = M_W^2 G_F, \quad (1.21)$$

where  $M_W$  is the mass of the charged gauge boson, which is called the W boson.

The theory is valid only if a neutral heavy boson ( $Z_\mu$ ) exists, along with the massless electromagnetic field,  $A_\mu$ , and they are related in the following way:

$$\begin{pmatrix} A_\mu \\ Z_\mu \end{pmatrix} = \begin{pmatrix} \cos\theta_W & \sin\theta_W \\ -\sin\theta_W & \cos\theta_W \end{pmatrix} \begin{pmatrix} B_\mu \\ W_\mu^3 \end{pmatrix}, \quad (1.22)$$

where  $\theta_W$  is the so called *Weinberg angle*:

$$\cos\theta_W \equiv \frac{g}{\sqrt{g^2 + g'^2}}. \quad (1.23)$$

Finally, the electromagnetic coupling constant, i.e. the electric charge, is given by:

$$e = g \sin\theta_W. \quad (1.24)$$

### 1.1.3 Higgs-Kibble Mechanism

The electroweak lagrangian in Eq. (1.19) does not include mass terms for the particles. This is due to the fact that a mass term violates the gauge symmetry<sup>4</sup>. Hence one has to invent some mechanism that introduces massive particles. The simplest mechanism that has been proposed so far is the so called Higgs-Kibble mechanism [7–9].

The Higgs-Kibble mechanism is based on the observation that the mass term of a scalar field respects the symmetry of the electroweak theory. According to this model, a scalar doublet is introduced:

$$\Phi \equiv \begin{pmatrix} \phi^+ \\ \phi^0 \end{pmatrix}, \quad (1.25)$$

where  $\Phi$  is the so called *Higgs field* and its lagrangian is:

$$\mathcal{L}_{Higgs} = \partial_\mu \Phi^\dagger \partial^\mu \Phi - V(\Phi^\dagger \Phi), \quad (1.26)$$

with the potential given by

$$V(\Phi^\dagger \Phi) = \mu^2 \Phi^\dagger \Phi + \lambda (\Phi^\dagger \Phi)^2 \quad (1.27)$$

In order to maintain invariance the Higgs field should transform like the left handed field in Eq. (1.15) but with hypercharge  $Y = 1$ . The vacuum expectation value of the Higgs field can be chosen to be:

$$\langle \Phi \rangle_0 = \begin{pmatrix} 0 \\ v/\sqrt{2} \end{pmatrix}, \quad (1.28)$$

---

<sup>4</sup>In order to see that remember that a mass term is  $\sim m^2 \bar{\psi} \psi$ . However, the field  $\psi$  contains both the left-handed and the right-handed parts, which are transformed with different rules.

where the parameter  $v$  is such that the Higgs potential in Eq. (1.27) is minimized:

$$v = \sqrt{\frac{-\mu^2}{\lambda}}. \quad (1.29)$$

The choice of the expression in Eq. (1.28) is deliberate so that the electromagnetic  $U(1)$  symmetry is respected and the charge of the vacuum is zero.<sup>5</sup>

Assuming a perturbation around the minimum of the Higgs potential such that  $v \rightarrow v + H$  we can write the Higgs scalar lagrangian of Eq. (1.26) as follows:

$$\mathcal{L}_{Higgs} = \left| D_\mu \frac{v+H}{\sqrt{2}} \begin{pmatrix} 0 \\ 1 \end{pmatrix} \right|^2 - \mu^2 \left( \frac{v+H}{\sqrt{2}} \right)^2 - \lambda \left( \frac{v+H}{\sqrt{2}} \right)^4. \quad (1.30)$$

From this equation and after some lines of algebra the quadratic terms in the vector fields can be found to be:

$$\frac{g^2(v+H)^2}{4} W_\mu^+ W^{-\mu}, \quad \frac{g^2(v+H)^2}{4} \frac{1}{2 \cos^2 \theta_W} Z_\mu Z^\mu \quad (1.31)$$

and hence the masses of the gauge bosons<sup>6</sup> are written as:

$$M_W = \frac{gv}{2}, \quad M_Z = \frac{gv}{2 \cos \theta_W}. \quad (1.32)$$

The mass term of the Higgs field itself can be read from the coefficient of the  $H^2$  term:

$$M_H = \sqrt{-2\mu^2}. \quad (1.33)$$

The mass of the Higgs is *a priori* unknown in the Standard Model and hence there is no real Higgs mass prediction in the SM, although it can be constrained by precision

<sup>5</sup>The charge operator is  $Q = T_3 + Y/2$  as can be easily verified by applying it to a lepton doublet. With this definition it is easy to show that  $Q \langle \Phi \rangle_0 = 0$  and hence the vacuum is invariant under the  $U(1)$  symmetry of electromagnetism.

<sup>6</sup>These masses are the “tree-level” masses and they are modified by radiative corrections. These corrections amount to less than 1% of the “tree-level” mass.

electroweak measurements (see Ref. [23] and Section 1.2).

The Higgs-Kibble mechanism also provides mass to the leptons. This can be achieved in a gauge invariant way by the Yukawa coupling between the leptons with the Higgs field. The lagrangian for this interaction can be written:

$$\mathcal{L}_{yuk} = -G_l[\bar{R}(\Phi^\dagger L) + \text{h.c.}] = -\frac{G_l(v + H)}{\sqrt{2}}(\bar{l}_R l_L + \bar{l}_L l_R), \quad (1.34)$$

where  $G_l$  is the Yukawa constant,  $l$  stands for  $e$ ,  $\mu$  or  $\tau$  and h.c. stands for hermitian conjugate. In this way, neutrinos have zero mass and charged leptons have mass  $M_l = G_l v \sqrt{2}$ . The value of the Yukawa coupling of the lepton with the Higgs is not specified and can be expressed as:

$$C_{lH} = \frac{M_l}{v},$$

which means that the coupling is proportional to the mass of the lepton.

### 1.1.4 Standard Model and Beyond

The discussion so far has ignored the strong interaction and the quarks. The gauge theory of the strong force is based on the  $SU(3)$  gauge group, also referred to as *colour*  $SU(3)$  or  $SU(3)_c$ . The Standard Model is the extension of the electroweak symmetry group with the inclusion of  $SU(3)_c$ , so that the symmetry group is  $SU(3)_c \times SU(2)_l \times U(1)_Y$ .

The mass terms for the quarks can be introduced with a way similar to the leptonic masses. However, there are more complications due to the fact that the quark mass eigenstates are distinct from the weak eigenstates. Details on how quarks are incorporated in the SM are given in many textbooks, e.g. see Refs. [10, 11].

The SM has proven to be a very successful theory describing in a very precise way all calculable subnuclear processes observed so far at least up to the electroweak scale

(i.e.  $\sim 100$  GeV). However, it is not a complete theory of the interactions in nature since it does not include gravity. Moreover, it is likely that just above the electroweak scale there is a wealth of very interesting phenomena. This provides an important motivation for experiments at the Large Hadron Collider (LHC) at CERN (see Chapter 2).

The last piece of standard model that has not been directly observed is the Higgs sector. Precision electroweak measurements suggest a value for the Higgs mass that is very close to the current experimental limits. If a light Higgs boson does not exist, other mechanisms for electroweak symmetry breaking should take its place, like strong WW scattering (see e.g. [12]). In this case new phenomena will be revealed at the *Fermi scale*, i.e.  $\sim 1$  TeV, similar to the strong force behaviour at lower energies. If the Higgs boson exists and it is discovered in the theoretically expected region of the parameter space then another issue appears. The Standard Model as an effective theory should be valid up to a scale  $\Lambda$  and the radiative corrections to the Higgs mass will suffer from divergences that are quadratic in  $\Lambda$ . Assuming  $\Lambda$  to have a very large value implies that the Higgs mass corrections should also be very large, unless some fine tuning mechanism exists. There are some ways to circumvent this problem. The most popular of them is Supersymmetry (SUSY) [13, 14], which is a gauge theory that includes a set of operators that can transform a bosonic field to a fermionic field and vice versa. SUSY models give a natural way to stabilise the Higgs boson mass in the SM expected region and predict many new particles at the Fermi scale. Another reason for the popularity of supersymmetric theories is the fact that the Standard Model is simple direct product of 3 groups and does not unify the couplings of the strong and the electroweak force. Physicists hope for the existence of a more fundamental theory, the so called Grand Unified Theory (GUT), describing all three forces within a simple gauge group with common coupling constants. Within the Standard Model the evolution of coupling constants is such that they do not meet at a single point, but this situation changes if one assumes SUSY at the Fermi scale.

The electroweak scale may also provide clues related to questions of cosmological interest. Modern cosmological observations [15] suggest that less than 5% of the content of the universe consists of ordinary matter. The remaining  $\sim 95\%$  is mostly *dark energy* ( $\sim 72\%$ ) and *dark matter* ( $\sim 23\%$ ). Studies of the theoretical properties of dark matter that are needed to match the astrophysical observations suggest that a particle that interacts weakly and has a mass of the order of the electroweak scale could provide this dark matter (more details can be found in Ref. [16]). These hypothetical particles are known as Weakly Interacting Massive Particles (WIMPs) and if they exist, then it should be possible to be produced in colliders with enough centre of mass energy, like LHC [17].

In summary, although the Standard Model has been a successful theory that is satisfactory up to the electroweak scale there is expectation that new phenomena will arise just above the currently accessible energies. These phenomena, if they exist, will be within the reach of the LHC experiments, which have recently started taking data.

## 1.2 Physics of W and Z Bosons

Some of the most crucial tests of the Standard Model can be done by performing measurements of observables related to the electroweak vector gauge bosons (vector bosons for shorthand). The wealth of experimental and theoretical work in this area is such that only a very small part can be described here. More details can be found elsewhere [18, 22–24].

The masses of the W and Z bosons according to the Standard Model can be calculated approximately using Eqs. (1.21), (1.24) and (1.32). The only unknown quantities in these relations are the values of the Fermi constant and the Weinberg angle. The value of the Fermi constant is known from muon decay experiments and the Weinberg angle can be measured in studies of neutrino-nucleon scattering, which give a value

$\sin^2 \theta_W \sim 0.22$  [33]. This results in W and Z masses that are  $m_W \sim 79$  GeV and  $m_Z \sim 90$  GeV. This was an important prediction of the theory that the experiments had to test.

That was more or less the situation when in the early 1980's CERN's  $Spp\bar{S}$  machine started colliding protons with antiprotons at 540 GeV centre-of-mass energy. The collisions were recorded by 2 general purpose detectors, named *UA1* and *UA2* (see Ref. [19] and references therein). The primary motivation for these experiments was the search for the weak vector bosons and the study of their production through the detection of their decays.

The production of vector bosons in the  $Spp\bar{S}$  was mainly due to quark antiquark annihilation. In the case of the Z boson the relevant reaction is:

$$q\bar{q} \rightarrow Z,$$

where  $q$  is mainly  $u$  and  $d$  quarks, with a small contribution of  $c$ . In the case of the W boson the relevant reaction is:

$$q\bar{q}' \rightarrow W,$$

where the quark pair is mainly  $(u, \bar{d})$  (or  $(d, \bar{u})$  depending on the charge of the produced W). There are also other production channels, where gluons are involved, which however, contribute less to the total production cross section.

The weak vector bosons decay through several channels, which may include leptons or quarks. In a hadron collider environment, the easiest way to detect them is through their leptonic decays and in particular through:

$$W \rightarrow e\nu_\mu \text{ or } \mu\nu_\mu, \quad Z \rightarrow ee \text{ or } \mu\mu.$$

Simple counting, assuming 3 colour charges, 5 quark flavours and 3 lepton families,

estimates that the branching ratio for  $W \rightarrow e\nu$  or  $W \rightarrow \mu\nu$  is about 1/9 for each of them, whereas for  $Z \rightarrow ee$  and  $Z \rightarrow \mu\mu$  is about 1/18. In order to study these channels the experiments should be able to identify and measure the properties of charged leptons, as well as the neutrino that accompanies the W boson decay. Neutrino identification is performed by measuring an imbalance of momentum in the transverse plane with respect to the beam. This demand requires an instrumented region that spans a large solid angle and consequently increases the cost of the detector.

The W boson was finally discovered in 1983 by identifying events with a high transverse energy electron plus some missing transverse energy in the calorimeter [20]. The Z boson was also discovered in the same year through its  $Z \rightarrow ee$  decay channel. However, these signatures are not enough to prove that the produced particle is indeed the long sought weak vector bosons. Strong evidence that the produced particle is indeed the long-sought W boson is provided by the measurement of the asymmetry in the angular distribution of the measured electrons [21]. This is because the weak interaction favours left-handed particles and right-handed anti-particles. This means that in W production through quark anti-quark annihilation the produced  $W^+$  bosons should have spin in the direction of the anti-proton beam, whereas the opposite is true for  $W^-$ . By the same token, assuming a left-handed neutrino and a right-handed positron (or a left-handed electron and a right-handed antineutrino) one would expect an asymmetry in the angular distribution of the produced charged lepton. The observation of this asymmetry reassures us that indeed the process is related to the weak force and also that the spin of the particle is 1.

Precision measurements of Z and W observables were performed at the LEP [25] experiments at CERN, the SLD (see references in [34]) experiment at SLC (Stanford Linear Collider) [26] and the Tevatron experiments at Fermilab (see [23, 24] and references therein). The LHC experiments will also perform measurements of Z and W observables.

LEP was an electron-positron collider, which operated initially at centre of mass energy close to the Z pole and later close to the WW production threshold. It was operated from 1989 till 2000 with four experiments (ALEPH [27], DELPHI [28], L3 [29] and OPAL [30]), which collected more than  $15 \times 10^6$  hadronic Z decays,  $1.7 \times 10^6$  leptonic Z decays and about 40 000  $ee \rightarrow WW$  events. SLC was a linear electron-positron collider, which was operated close to the Z pole and had the unique feature of providing polarised beams. SLC had one experiment (SLD - Stanford Linear Detector), which managed to collect 150 000 Z decays with about 77% polarised beam and 70 thousand decays with lower beam polarisation. Finally, the Tevatron is a proton-antiproton collider operating currently at 1.96 TeV centre-of-mass energy. The two Tevatron experiments (CDF [31] and D0 [32]) have collected about  $10 \text{ fb}^{-1}$  of integrated luminosity so far. In the following a quick and incomplete review of some of most important results of these experiments that are related to Z and W observables will be given.

The cross section of the electron-positron annihilation to fermions can be calculated theoretically assuming SM interactions only and it can be measured experimentally. In Fig. 1.1 the result of this comparison for hadronic final states is shown as measured by several experiments. The results show a very good agreement with the SM over a wide range of energies. In the same figure is also shown a glimpse of the Z line shape measurement at LEP. By running LEP at a range of different energies around the Z pole and measuring the cross section at each energy the “line shape” can be determined. The width of this shape depends on the invisible width of the Z and hence on the number of light neutrino species. This dependence is illustrated in Fig. 1.2 where the measured cross sections of hadron production for different energies around the Z pole are shown, along with SM predictions with 2,3 and 4 light neutrino species. The experimental results favour 3 neutrino species. The same measurement can be also performed with a more direct way by measuring events with initial state radiation where the Z has decayed to 2 neutrinos. The results of this analysis are in agreement with the Z line shape studies, but the precision is an order of magnitude worse [5]. The

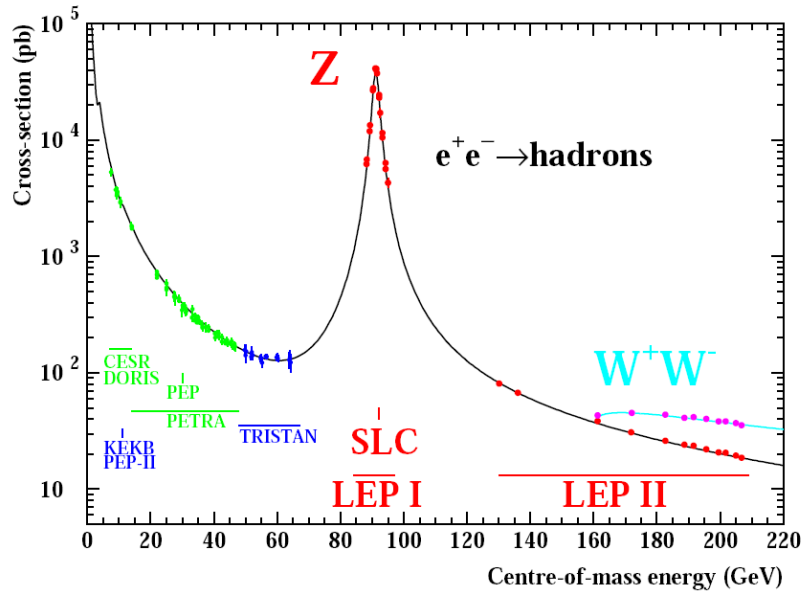


Figure 1.1: The cross section of electron-positron annihilation to hadrons as predicted by SM (continuous line) and as it is measured by various experiments [22].

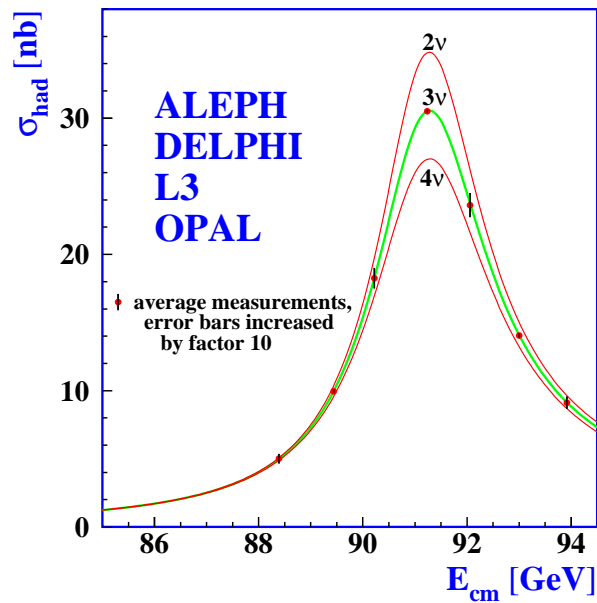


Figure 1.2: The cross section of hadron production around the Z resonance from LEP [34]. The continuous curves indicate the predicted cross section for 2, 3 and 4 neutrino species with SM couplings and negligible mass.

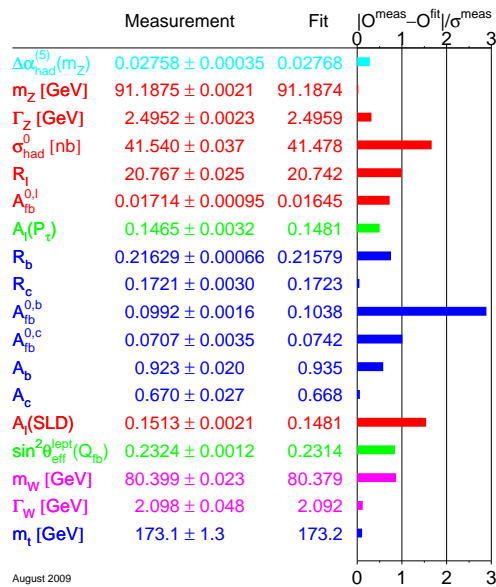


Figure 1.3: Precision measurements of various observables. The experimental results are compared to the Standard Model values, which are derived by a fit that includes further observables. The difference of the fit value from the measurement (pull) is also quoted. For more details see [23].

Z line shape analysis, with the comparison of the width of the Z to hadrons and the corresponding width for leptons, can also provide a measurement of the strong coupling constant,  $\alpha_s$ , at energies close to the Z peak. These measurements provide the value of  $\alpha_s$  at the highest energy so far. Other studies have focused on the asymmetry of the Z pole, features that are related to the fact that the weak force treats left-handed and right-handed particles differently. In Table 1.3, where the summary of the electroweak precision measurements from the LEP, SLD and Tevatron experiments is presented many of the observables are related to these asymmetries. More details can be found in Ref. [23].

LEP has also operated just above the WW production threshold measuring among other observables the WW production cross section (Fig. 1.4). This measurement is an example of how one can distinguish between the SM and similar theories with different

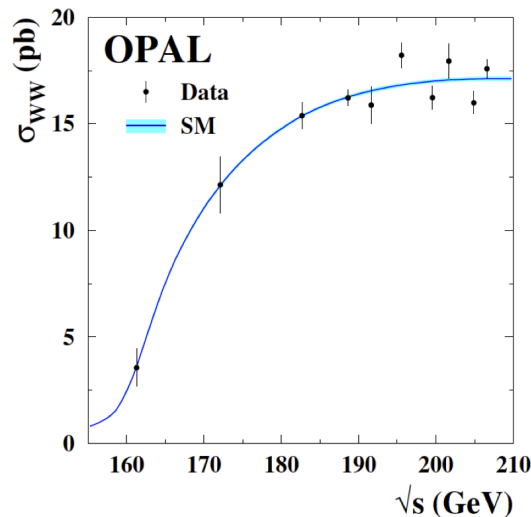


Figure 1.4:  $WW$  production cross section as measured at LEP with the OPAL detector (points) compared with the SM expectation (line). The shaded error shows the theoretical uncertainty. For more details see [35].

features (see e.g. Ref. [22]).

Precision measurements of the  $W$  boson mass that were performed in the Tevatron and LEP experiments can be combined with measurements of the top quark mass measurements from the Tevatron experiments and obtain a restriction on the Higgs mass [36]. A recent compilation of these constraints is shown in Fig. 1.5(a) [5].

In summary, the study of the  $W$  and  $Z$  bosons has played an important role in establishing SM. Measurements of very high precision have been used to constrain SM parameters as for example in Fig. 1.5(b) where the curve shows the best fit for the Higgs mass using the available precision electroweak data.

### 1.3 $W$ Production in Proton-Proton Collisions

In proton-proton collisions the dominant mechanism for vector boson production is via the annihilation of a quark anti-quark pair in the Drell-Yan process [37]. In particular, the dominant interactions in the case of the  $W$  boson are:  $u\bar{d} \rightarrow W^+$  and  $d\bar{u} \rightarrow W^-$ .

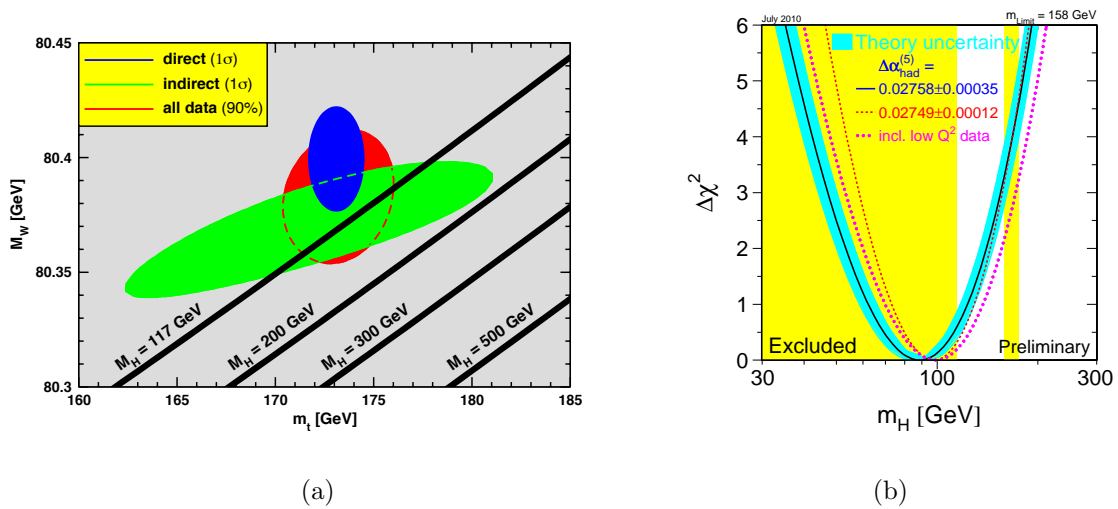


Figure 1.5: Higgs mass restrictions from measurements of the  $W$  and top quark masses in (a) [5] and limits from direct searches at LEP and the Tevatron experiments and expected values from EWK precision tests [23].

Most of the proton's momentum is carried by the valence quarks and there are more valence quarks than anti-quarks. This results in a higher abundance of  $W^+$  than  $W^-$  leading to the charge asymmetry in the high transverse momentum leptons that is observed experimentally (e.g. [38]).

The Drell-Yan process is relatively well understood and the main uncertainties in the  $W$  production are related to the parton distribution functions and higher order QCD effects. Increased precision on gluon parton distribution functions has been obtained from recent measurements at HERA [63]. This contributes to a lower uncertainty on the sea quarks reducing the uncertainty on the theoretical cross-section to 5% [39, 91, 92].

$W$  bosons are unstable particles and they decay to a pair of leptons or a pair of quarks. Leptons can be measured with much better precision than quarks that fragment into jets of particles, which cannot be measured with the precision with which a muon or an electron can be measured. The leptonic decay of a  $W$  can be of three types with each of them having a branching ratio of  $10.75 \pm 0.13\%$  [5]:

$$W^- \rightarrow e^- \bar{\nu}_e, \quad W^- \rightarrow \mu^- \bar{\nu}_\mu, \quad W^- \rightarrow \tau^- \bar{\nu}_\tau,$$

with similar decays for the anti-particles. The first two of these decays are the easier to measure due to their simpler final states in the detector. The work described in this thesis focuses on the decay of  $W$  in the electron channel.

At the LHC the  $W \rightarrow e\nu$  cross section is  $\sim 10$  nb, which is higher than other interesting processes (c.f.  $\sim 1.7$  nb for  $Z \rightarrow e^-e^+$  or  $\sim 0.16$  nb for  $t\bar{t}$ ). In practice, this means that the majority of prompt electrons that are produced in proton proton collisions come from  $W$  boson decays and the study of this particular channel is very important for the commissioning of the electron reconstruction and identification in the experiments.

## Summary

The Standard Model of particle physics (SM) provides a theoretical framework which can describe almost all subnuclear processes occurring on an energy scale up to The last part of this theory yet to be verified by experiment is the Higgs boson, whose existence is also connected to physics beyond the SM. The search for the Higgs boson and physics beyond the SM have been the main motivation for the Large Hadron Collider project at CERN. Many of the precision measurements that led to the establishment of SM are related to the  $W$  and  $Z$  bosons. The leptonic decays of the  $W$  and  $Z$  bosons provide signatures that are easy to identify in a hadron collider environment and the major source of prompt leptons. For this reason, apart from precision measurements and new physics searches, they play an important role in the commissioning of lepton objects in the experiments.

# Chapter 2

## The CMS Experiment

*An observation describes the face of a phenomenon without revealing its nature. An experiment is staged with precisely the aim of understanding the nature of the regularities observed.*

Boris M. Bolotovskii quoting Sergey I. Vavilov

The purpose of this chapter is to introduce the Large Hadron Collider (LHC) project at CERN and the Compact Muon Solenoid (CMS) experiment, which is one of the LHC experiments.

### 2.1 Introducing the Large Hadron Collider

The Large Hadron Collider (LHC) [40, 41] is a 27 km circular particle accelerator at CERN, Switzerland, which is designed to accelerate and collide beams of protons or heavy ions. The design centre-of-mass energy ( $\sqrt{s}$ ) for proton-proton collisions is 14 TeV. The LHC is currently the highest energy accelerator ever constructed.

Proton acceleration starts from a linear accelerator that injects the protons to the Proton Synchrotron (PS), which accelerates them to 25 GeV. In the following stage, the

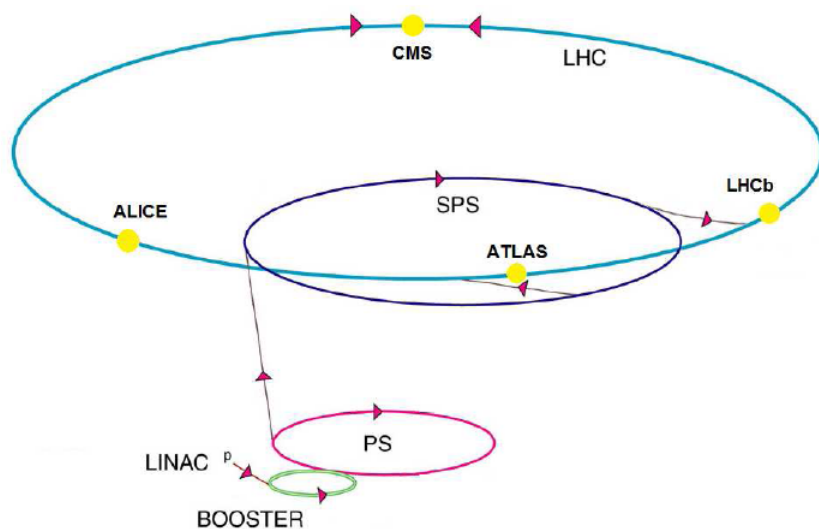


Figure 2.1: The LHC accelerator complex.

Super Proton Synchrotron (SPS) accelerates the beams to 450 GeV and subsequently injects them into the LHC ring (see Fig. 2.1).

The protons in the LHC beam are in cylindrical bunches with a nominal interaction diameter of  $16 \mu\text{m}$  and a length of 8 cm. The nominal bunch separation is 25 ns. The maximum number of possible bunches in the LHC orbit is 3564, however, only 2808 are intended to be used, leaving gaps that are used for dumping the beam and machine synchronisation. LHC is intended to reach an instantaneous luminosity is  $10^{34} \text{ cm}^{-2}\text{s}^{-1}$ .

The LHC was fully commissioned and started operation in September 2008, however, several days after the first beam circulation, the machine had to stop due to technical problems [42]. The accelerator started again in November 2009 running initially at 450 GeV per beam and later (December 2009) at 1.18 TeV per beam. In March 2010 the beam energy was raised to 3.5 TeV and the instantaneous luminosity to about  $10^{27} \text{ cm}^{-2}\text{s}^{-1}$ . Since then the instantaneous luminosity has been steadily increased: in summer 2010 it was about  $10^{30} \text{ cm}^{-2}\text{s}^{-1}$  and by October it reached  $10^{32} \text{ cm}^{-2}\text{s}^{-1}$ . The total luminosity delivered during the LHC proton run in 2010 as a function of time is shown in Fig. 2.2. The current plan is that the LHC will continue running at 3.5 TeV

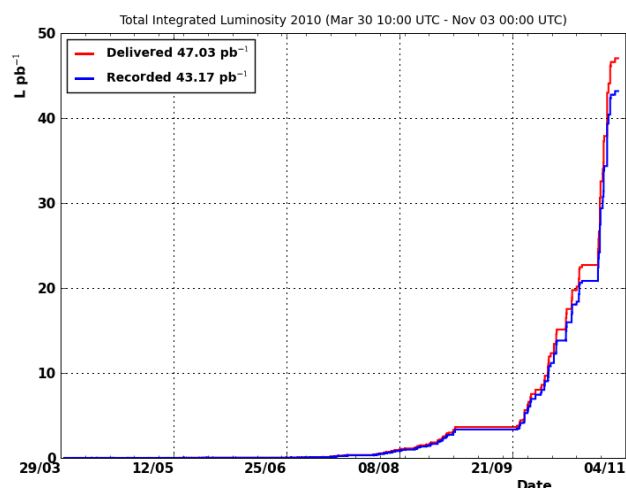


Figure 2.2: The integrated luminosity delivered by the LHC with 7 TeV proton-proton collisions from March till November 2010 as a function of time (red line). In the same plot it is shown also which part of these data were actually recorded by the CMS detector (blue line).

beam energy till the end of 2011. By then it is expected to have delivered collision data of about  $1 \text{ fb}^{-1}$  [43].

The LHC beams can be brought into collision at 4 different points on the LHC ring. Around each of these points detectors have been constructed. The four experiments that are located at these collision points are ALICE (An LHC Heavy Ion Experiment) [44], ATLAS (A Toroidal LHC Apparatus) [45], CMS (Compact Muon Solenoid) [46] and LHCb (LHC beauty experiment) [47]. Two of these experiments (ATLAS and CMS) are general purpose detectors, whereas ALICE is optimised for heavy ion collisions and LHCb for B-hadron physics. Further away from the interaction points there exist two more experiments, LHCf and TOTEM<sup>1</sup>.

<sup>1</sup>TOTEM is designed to measure the total proton-proton cross section and LHCf is dedicated to neutral particles emitted in the very forward regions.

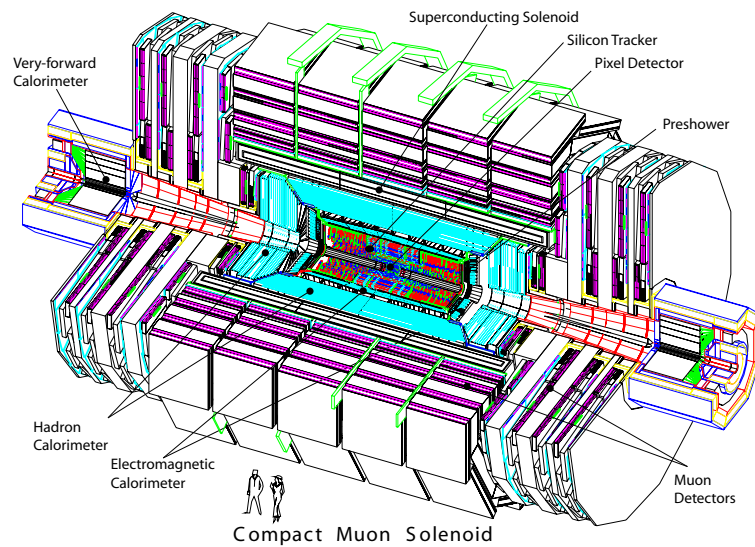


Figure 2.3: The layout of the CMS detector. It is 21.6 m long and has a diameter of 14.6 m. Its total weight is 12 500 t. (reproduced from [46]).

## 2.2 The CMS Experiment

Detectors in collider experiments are composed of layers of material sensitive to the passage of high energy particles, along with the necessary equipment to trigger on, readout, select and store the information produced.

CMS [46] is a general purpose detector that surrounds Interaction Point 5 of the LHC ring. It is designed to study the physics at the Fermi scale ( $\sim 1$  TeV) and in particular the origin of electroweak symmetry breaking and to search for physics beyond the Standard Model. CMS will also study heavy ion collisions. Its design has to take into account the severities of the LHC environment that demand a fast responding detector (beam collisions every 25 ns) in a high radiation environment.

The fundamental concept of the CMS design (see Fig. 2.3) is a solenoid magnet that contains the tracking and the calorimetry systems. This introduces space limitations for the size of the calorimeters and, along with the demand for the best possible electron and photon energy resolution, leads to the choice of a crystal electromagnetic calorimeter (ECAL).

The coordinate convention of CMS has the origin at the interaction point. The y-axis points vertically upwards, the x-axis points radially inwards towards the centre of the LHC ring and the z-axis points along the anticlockwise beam direction. The azimuthal angle  $\phi$  is measured from the x-axis in the x-y plane. The polar angle  $\theta$  is measured from the z-axis. Pseudorapidity is defined as  $\eta = -\ln \tan(\theta/2)$  and distance in  $\eta$ - $\phi$  space is measured by the use of the variable  $\Delta R \equiv \sqrt{\Delta\eta^2 + \Delta\phi^2}$ . Momentum measured in the plane transverse to the beam direction is denoted by  $p_T$  and referred to as transverse momentum. Similarly, transverse energy is defined as  $E_T \equiv E \sin \theta$ .

In the following a short overview of the components of CMS is given.

### 2.2.1 The Superconducting Solenoid Magnet

The LHC physics programme requires high precision momentum and charge measurement. This is achieved with a high resolution tracking system that is immersed in a uniform high magnetic field. This magnetic field in CMS is generated by a superconducting solenoid magnet 12.5 m in length and 6 m in diameter. The magnitude of the generated magnetic field is 3.8 T. The flux is returned through an iron yoke comprising 5 wheels and 2 endcaps, composed of three disks each. The return field in the yoke provides the bending field for the muon system, which is housed between the iron layers.

The precision of the momentum measurement with the CMS inner tracking system depends crucially on the homogeneity of the magnetic field and its precise description. Within the tracker region the field is relatively homogeneous (at about 5% level [51]) and it has been mapped with a precision better than 0.1% [52].

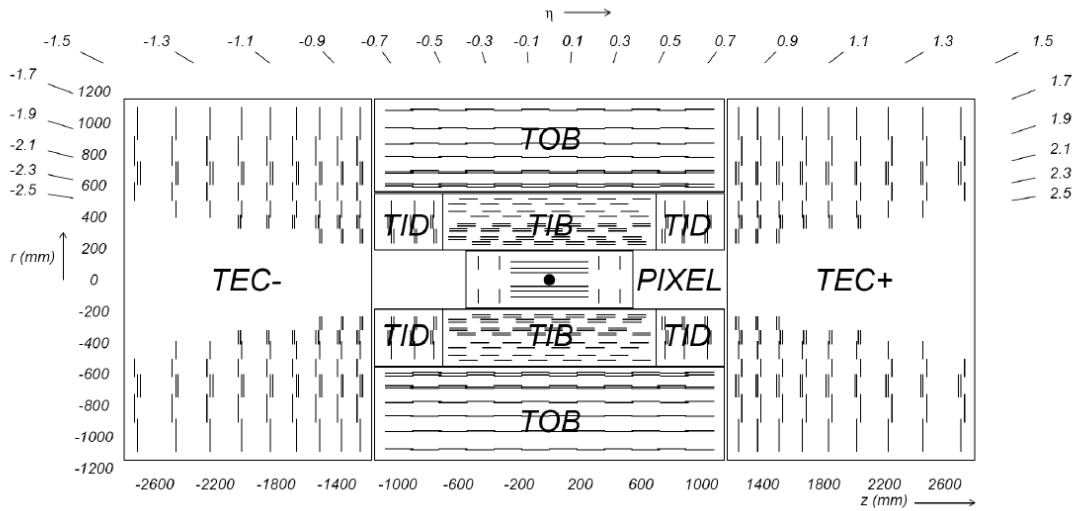


Figure 2.4: The CMS inner tracking system layout (from [53]).

### 2.2.2 The Inner Tracking System

The first detectors that the particles coming from the interaction point pass through are the inner tracking system detectors (ITD), which will be collectively referred to as the “tracker”. The tracker detectors are the Pixel Tracker Detector and the Silicon Tracker Detector (Fig. 2.4). Their purpose is to provide information that can be used to reconstruct the tracks of charged particles and the vertex position.

The pixel detector is the closest detector to the interaction point. It consists of 3 barrel layers and 2 endcap disks on each side. The 3 barrel layers are located at mean radii of 4.4 cm, 7.3 cm and 10.2 cm, and have a length of 53 cm. The 2 endcap disks, extending from 6 to 15 cm in radius, are placed on each side at  $|z| = 34.5$  cm and 46.5 cm. The pixel detector consists of 66 million hybrid pixel elements with an almost square shape of  $100 \times 150 \mu\text{m}$ . This size was chosen in order to achieve optimal vertex position resolution. The spacial resolution is measured to be  $10 \mu\text{m}$  for the  $\rho\text{-}\phi$  measurement and about  $20 \mu\text{m}$  for the  $z$  measurement. The readout uses approximately 16 000 readout chips, which are bump-bonded to the detector modules.

The Silicon Strip Tracker (SST) has also the usual barrel-endcaps geometry. The barrel

is composed of the Tracker Inner Barrel (TIB) and the Tracker Outer Barrel (TOB). The TIB is made of 4 layers and covers up to  $|z| < 65$  cm and the TOB comprises 6 layers with a half length of  $|z| < 110$  cm. The endcaps are divided into the Tracker End Cap (TEC) and the Tracker Inner Disks (TID). Each TEC comprises 9 disks that extend into the region  $120 \text{ cm} < |z| < 280$  cm, and each TID comprises 3 small disks that fill the gap between the TIB and the TEC. SST coverage in pseudorapidity is  $|\eta| < 2.5$ .

The total number of silicon sensors in the strip tracker is 24 244 with about 9.3 million strips. The sensor thickness varies from 320 to 500  $\mu\text{m}$  and the strip pitch from 80 to 180  $\mu\text{m}$  depending on which tracker sub-detector the strip is mounted on. The modules in the first two layers and rings, respectively, of TIB, TIB, TID, and TOB as well as rings 1, 2, and 5 of the TECs carry a second micro-strip detector module which is mounted back-to-back with a stereo angle of 100 mrad in order to provide a measurement of the second co-ordinate ( $z$  in the barrel and  $r$  on the disks). The single point resolution for the TIB is 23-34  $\mu\text{m}$  in the  $\rho$ - $\phi$  direction and 230  $\mu\text{m}$  in  $z$ . For the other parts of the detector single-point resolution becomes worse by up to a factor of 2.

The tracker is used to measure the momentum of charged particles. The momentum resolution varies as a function of the particle  $p_T$  and  $\eta$ . For muons with high momentum ( $p_T = 100 \text{ GeV}/c$ ) it is around 1-2% for  $|\eta| < 1.6$  (see also Fig. 2.5).

The pixel detector can also help in the identification of prompt particles, i.e. particles that come directly from the interaction point. For example a prompt electron candidate reconstruction starts from an energy deposition in the ECAL that is geometrically compatible with hits in the pixel detector.

Reconstructed tracks are used to locate the primary vertex. The primary vertex is associated with the original proton-proton interaction that gave rise to the event under study. The presence of multiple proton-proton interactions in the same bunch crossing, at high luminosity, results in multiple primary vertices. These vertices can be recon-

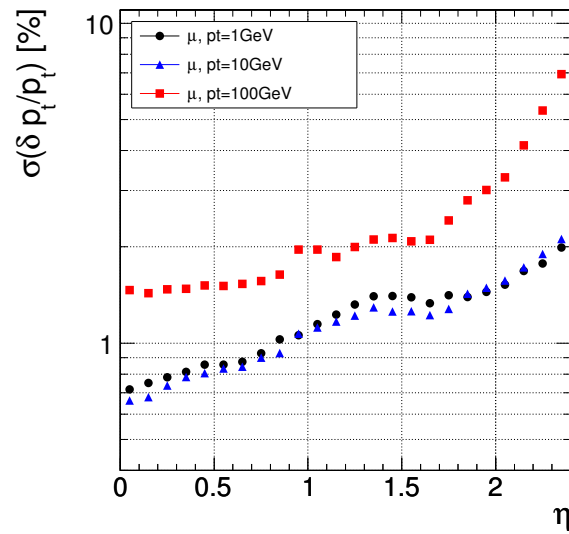


Figure 2.5: Transverse momentum resolution for single muons with transverse momentum 1, 10 and 100 GeV (reproduced from [46]).

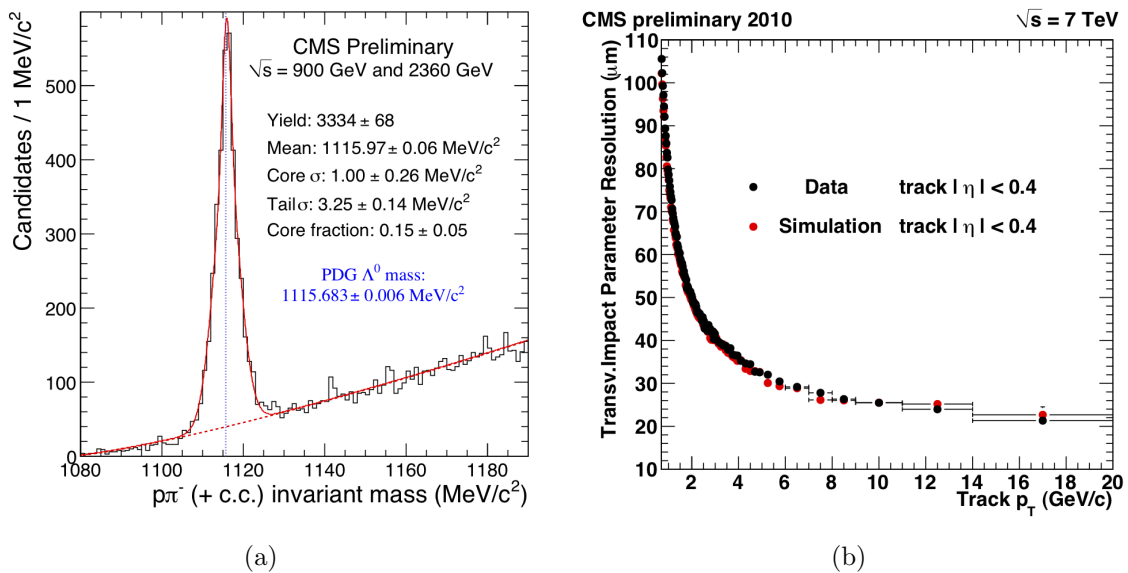


Figure 2.6: Tracking performance with collision data. (a) Reconstruction of the  $\Lambda^0$  resonance with 2009 collision data (from [54]). (b) Transverse impact parameter resolution with 7 TeV data (from [55]).

structed and distinguished by the tracker. Secondary vertices created by the decays of long lived particles are also measured. For example B-hadrons have lifetimes of  $\mathcal{O}(\text{ps})$ , which is considerably longer than other short-lived particles. The reconstruction of tracks from a secondary vertex can be used for b-flavour identification (b-tagging).

The performance of the tracking system has been evaluated with collision data and it is found to be in good agreement with the expectations [54, 55]. A demonstration of the track  $p_T$  resolution is shown in Fig. 2.6(a) where the proton-charged pion invariant mass is plotted in the region of the  $\Lambda^0$  resonance. The transverse impact parameter resolution as it is measured with recent 7 TeV data compared to expectations from simulation is shown in Fig. 2.6(b).

### 2.2.3 The Electromagnetic Calorimeter (ECAL)

The CMS ECAL is a homogeneous lead tungstate ( $\text{PbWO}_4$ ) calorimeter composed of 75 848 truncated-pyramid shaped crystals. ECAL was designed to fulfil the following requirements:

- Compatible with the CMS design: the ECAL is placed inside the HCAL which is itself inside the solenoidal bore, hence a very compact design is needed.
- Best possible energy resolution, benchmarked by performance for  $H \rightarrow \gamma\gamma$ .
- Radiation hard.
- Fast response (c.f. nominal LHC bunch separation 25 ns).

These requirements have led to the choice of a homogeneous calorimeter (excellent energy resolution) made of lead tungstate crystals, which are dense and radiation hard, with a fast scintillation decay time. More details about ECAL can be found in Section 2.3.

### 2.2.4 The Hadronic Calorimeter (HCAL)

The calorimetric system is completed by the CMS Hadronic Calorimeter (HCAL), which provides measurement of hadronic showers and assists in the triggering on, and measurement of, jets and missing transverse energy. It comprises 4 subdetectors: the Hadronic Barrel (HB), the Hadronic Outer (HO), the Hadronic Endcap (HE) and the Hadronic Forward (HF). HB and HE are sampling calorimeters using brass as the absorbing material and plastic scintillator tiles. HB covers the pseudorapidity range  $|\eta| < 1.3$  with granularity  $\Delta\eta \times \Delta\phi = 0.087 \times 0.087$  and HE covers the range  $1.3 < |\eta| < 3.0$  with granularity that varies in  $\eta$  from  $\Delta\eta \times \Delta\phi = 0.087 \times 0.087$  at  $\eta = 1.3$  to  $\Delta\eta \times \Delta\phi = 0.350 \times 0.174$  at  $\eta = 3.0$ . HB is radially restricted between the ECAL outer extent ( $r = 1.77$  m) and the inner extent of the solenoid magnet ( $r = 2.95$  m). This constrains the total amount of material that can be put in to absorb the hadronic shower. For this reason, HO is placed outside the solenoid magnet as a “tail-catcher” and covers the pseudorapidity range  $|\eta| < 1.26$ . It comprises in the central region ( $|\eta| < 0.33$ ) two scintillator layers separated by iron absorber and a single scintillator layer for the rest of the  $\eta$  range and its granularity has a matching  $\Delta\eta \times \Delta\phi$  to HB. Finally, HF is a steel/quartz fibre calorimeter covering the pseudorapidity range  $3.0 < |\eta| < 5.0$  with granularity that varies with  $\eta$  from  $\Delta\eta \times \Delta\phi = 0.111 \times 0.174$  at  $\eta \simeq 3$  to  $\Delta\eta \times \Delta\phi = 0.302 \times 0.348$  at  $\eta \simeq 5$ .

The energy resolution for hadronic jets has been studied using data [58]. The best performance is achieved using particle flow techniques [76, 77]. The  $E_T$  resolution for jets with  $E_T > 40$  GeV is better than 10% as shown in Fig. 2.7(a). For the missing  $E_T$  ( $\cancel{E}_T$ ) performance with the particle flow algorithm, a resolution between 5% and 10% is estimated as shown in Fig. 2.7(b).

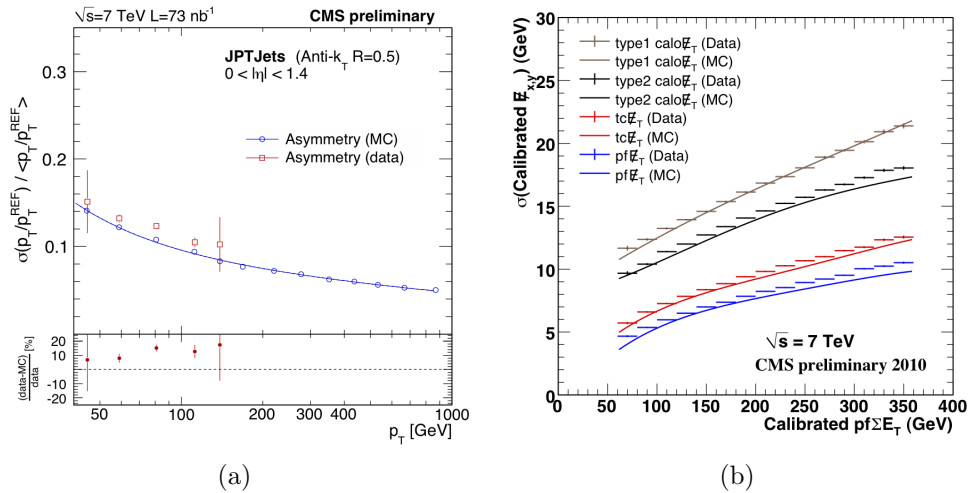


Figure 2.7: Jet transverse energy resolution in (a) and missing transverse energy resolution in (b) with CMS collision data. For more details see [58].

## 2.2.5 The Muon System

The functions of the muon system are muon identification, momentum measurement and triggering. Muon detectors are housed in between the iron plates of the magnet yoke. This provides the magnetic field for the momentum measurement but also serves as a hadron absorber for the identification of muons.

The muon system layout follows the yoke layout and has a cylindrical barrel section and two planar endcap regions. The barrel section covers the pseudorapidity range  $|\eta| < 1.2$ . This region is characterised by a small neutron background, low muon rate and uniform magnetic field mostly contained in the yoke. These properties allow the use of standard drift tube chambers. The barrel drift tube chambers are organised in four stations with part of them measuring the muon coordinate in the  $r$ - $\phi$  bending plane and the remaining measuring the muon  $z$  coordinate. The endcap region covers the pseudorapidity region  $1.2 < |\eta| < 2.4$ , where the backgrounds are large, the muon rates high and the magnetic field large and non-uniform. These features do not allow the use of drift chambers and cathode strip chambers have been used instead. Both drift tubes and cathode strip chambers can trigger on the  $p_T$  of the muons with

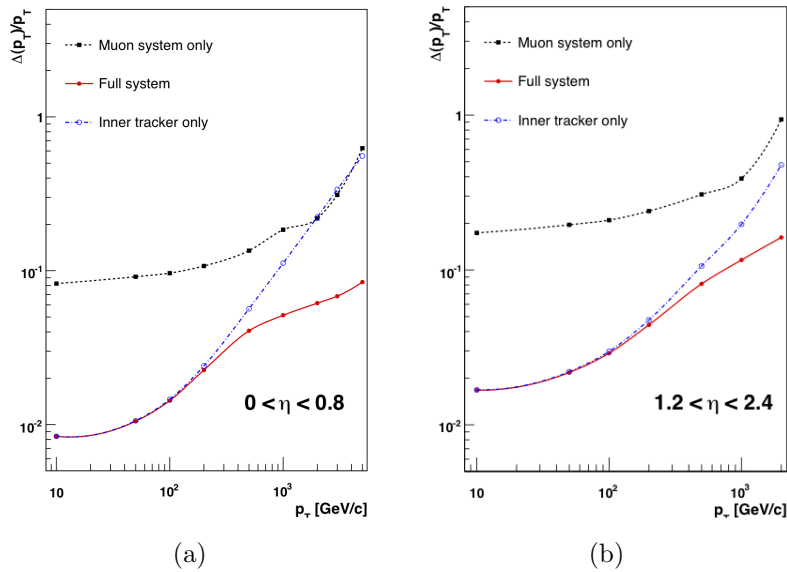


Figure 2.8: Muon transverse momentum ( $p_T$ ) resolution as a function of  $p_T$  using the muon system only, the inner tracking only, and both. In (a) the resolution is plotted for muons in  $|\eta| < 0.8$  and in (b) for muons in  $1.2 < |\eta| < 2.4$ . Plot reproduced from [46]

good efficiency and high background rejection, however, due to the uncertainties in the eventual background rates and the poor time resolution characteristics of the system, a complementary trigger system based on resistive plate chambers was added in both barrel and endcap regions. Resistive plate chambers cover the pseudorapidity range  $|\eta| < 1.6$  and they produce a fast response with good timing resolution but coarser position resolution than the rest of the muon system.

The muon transverse momentum ( $p_T$ ) resolution at CMS is improved for high- $p_T$  muons with the use of the muon system. The expected  $p_T$  resolution performance is shown in Fig. 2.8. Studies with early data have shown that the muon  $p_T$  resolution agrees with the expectation for the start-up conditions (see Fig. 2.9).

## 2.2.6 The Trigger

At high luminosity there is potentially an event in each bunch crossing, i.e. an event rate of 40 MHz for the nominal LHC bunch separation (25 ns). However, events from

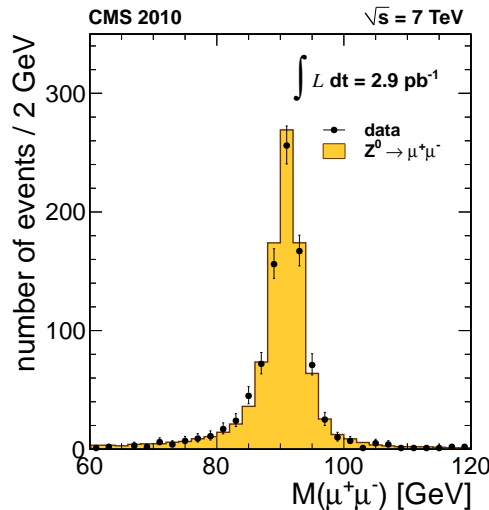


Figure 2.9: The di-muon invariant mass distribution (black points) as measured at CMS with  $2.9 \text{ pb}^{-1}$  of data compared with a simulated  $Z \rightarrow \mu\mu$  di-muon invariant mass distribution [72].

interesting processes, such as weak vector boson or Higgs boson production, are a very small fraction of these events due to the very small production cross sections compared to the total inelastic proton-proton cross section (see Fig. 2.10). In addition, there are technical limitations on handling such a large event rate. Due to the CMS data acquisition (DAQ) bandwidth limitations the event rate<sup>2</sup> that can be handled is up to about 100 kHz. Further limitations to the acceptable event rate are set by the online storage manager capacity (about 1 kHz) and the offline reconstruction and storage facilities ( $\mathcal{O}(100)$  Hz). The task of reducing the event rate to this level, while being efficient in events from interesting processes, is undertaken by the CMS trigger system. The CMS trigger is organised in 2 steps: the Level-1 trigger, which satisfies the DAQ switch fabric limitations, and the High Level Trigger (HLT), which satisfies the storage manager and offline reconstruction and storage limitations.

The Level-1 trigger is hardware based, largely using ASICs<sup>3</sup>, but with widespread use of FPGAs<sup>4</sup> where appropriate. Its electronics are housed partly on the detector, partly

<sup>2</sup>For an event size of about 100 kBytes.

<sup>3</sup>ASIC: Application Specific Integrated Circuit.

<sup>4</sup>FPGA: Field-Programmable Gate Array.

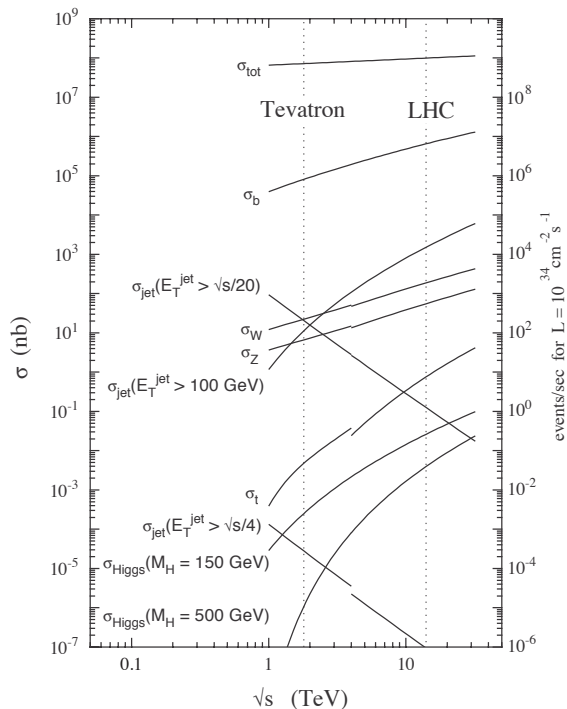


Figure 2.10: Proton-proton cross sections for various processes in centre of mass energy relevant to LHC physics. Reproduced from [50].

in the underground control room located at a distance of 90 m from the experimental cavern. The Level-1 trigger uses coarse local data from the calorimeter and muon systems to make electron/photon, jet, energy sum and muon triggers. The Level-1 trigger was generally operated at about 30 kHz in 2010.

The Level-1 calorimeter trigger is based on trigger towers of size  $0.087 \times 0.087$  in  $\eta$ - $\phi$  space in the central region and somewhat larger for  $|\eta| > 2$ . The electromagnetic trigger works with fully overlapping windows of  $3 \times 3$  trigger towers applying threshold to the sum of two adjacent ECAL towers and possibly further cuts on isolation, hadronic/electromagnetic fraction and/or the lateral shape in the ECAL. The jet trigger is based on  $3 \times 3$  windows of  $4 \times 4$  trigger tower arrays. Three types of jet triggers are defined - central, tau-jet, and forward - depending on the location and the shape of the object. The top four candidates in each class of calorimeter trigger are used for the final Level-1 trigger decision.

The Level-1 muon trigger receives information from the resistive plate chambers, which are fast, dedicated to trigger detectors, complemented by precise position measurements from the drift tubes in the barrel or the cathode strip chambers in the endcaps. The Level-1 muon trigger is programmed to find aligned hits in the muon detectors and create muon candidates from which the four best are used for the final Level-1 trigger decision.

The HLT runs on a farm of commercial processors using code that is as close as possible to the offline analysis code. The HLT takes as input the objects that the Level-1 Trigger produces and decides which events will be finally written to permanent storage. It is designed to reduce the output event rate to  $\mathcal{O}(100)$  Hz so that it satisfies the requirements discussed previously. During 2010 the HLT physics stream output rate was generally limited to about 400 Hz.

### 2.2.7 The CMS Computing Model

By 2011 CMS alone will require over 60 PB of storage [46]. Therefore no single computing centre is capable of providing these level of resources. This motivated the creation of the LHC Computing Grid which groups resources of multiples centres to share the workload both in terms of storage and processing capabilities. The CMS Computing Model makes use of the hierarchy of computing Tiers as proposed by the Models of Networked Analysis at Regional Centres (MONARC) [57] project. This model comprises

- A Tier-0 computing centre at CERN, which is directly connected to the experiment for the initial processing and data archiving. It is responsible for the safe-keeping of the first copy of the RAW experimental data. Furthermore the first reconstruction of the data will be produced and stored there. Finally the Tier-0 will reprocess the data during LHC down-times.
- Data from the Tier-0 will be distributed to 8 Tier-1 centres. Each Tier-1 is



Figure 2.11: Map showing the geographical distribution of CMS Tier-1 (red dots) and Tier-2 (blue squares) centers. Reproduced from [56].

responsible for the safe-keeping of a share of the second copy of the RAW and the reconstructed data. Large amounts of reprocessed data will also be kept there.

- Data from the Tier-1 will be transferred to 38 Tier-2 centres (see Fig. 2.11). These centres store the data for analysis by CMS physicists both local to the associated Tier-2 centre or remote users. Data at Tier-2 centres is not stored indefinitely, but is expected to be analysed and periodically replaced depending on the physics, detector or computing requirements.

## 2.3 The CMS ECAL

### 2.3.1 Lead Tungstate Crystals

Lead tungstate ( $\text{PbWO}_4$ ) [60] forms transparent crystals of very high density ( $8.3 \text{ g/cm}^3$ ). It has a small radiation length ( $0.89 \text{ cm}$ ) and a small Moliere radius ( $2.2 \text{ cm}$ ). These two properties allow for a compact calorimeter design that satisfies the limited space restriction inside the solenoid and the requirement for good spatial resolution. Much development work went into achieving radiation hard crystals [61].

The scintillation light that is emitted by  $\text{PbWO}_4$  is in the blue-green region of the spectrum and has a broad maximum at 420-430 nm. The light emission time is compatible with the LHC bunch crossing time: about 80% of the light is emitted in 25 ns. Despite these advantageous properties,  $\text{PbWO}_4$  has a light output that is considerably smaller than most other scintillators. This property has even lead to mistaken claims that actually  $\text{PbWO}_4$  does not scintillate at all and the produced light is mainly due to Cherenkov radiation [59]. The light output also varies with temperature with a gradient of -2.1% at 18°C [62]. At 18°C the light output gives about 4.5 photoelectrons per MeV in the barrel avalanche photodiodes (APD) and a very similar number in the endcap vacuum phototriodes (VPT) in which the lower quantum efficiency is compensated for by a larger sensitive area.

### 2.3.2 ECAL Layout

The CMS ECAL, as it is shown in Fig. 2.12, is divided into three components: the ECAL barrel (EB), the ECAL endcaps (EE) and the ECAL endcaps preshower detector (ES).

The EB covers the pseudorapidity range  $|\eta| < 1.479$  and its granularity is 360-fold in  $\phi$  and  $(2 \times 85)$ -fold in  $\eta$ . In total, 61 200 crystals with a truncated pyramidal shape, slowly varying with  $\eta$  (17 shapes), are mounted in a quasi-projective geometry to avoid cracks aligned with particle trajectories, so that the crystal axes make a small angle ( $3^\circ$ ) with respect to the vector from the nominal interaction point. The crystal cross section corresponds to approximately  $0.0174 \times 0.0174$  in  $\eta$ - $\phi$  or approximately  $22 \times 22$  mm<sup>2</sup> at the front face of the crystal. The crystal length is 230 mm corresponding to 25.8 radiation lengths ( $X_0$ ). The EB radius is 1.29 m and its total length in the z-direction is 6 m.

The crystals in the EB are organised in 36 “supermodules” (SM). Each supermodule

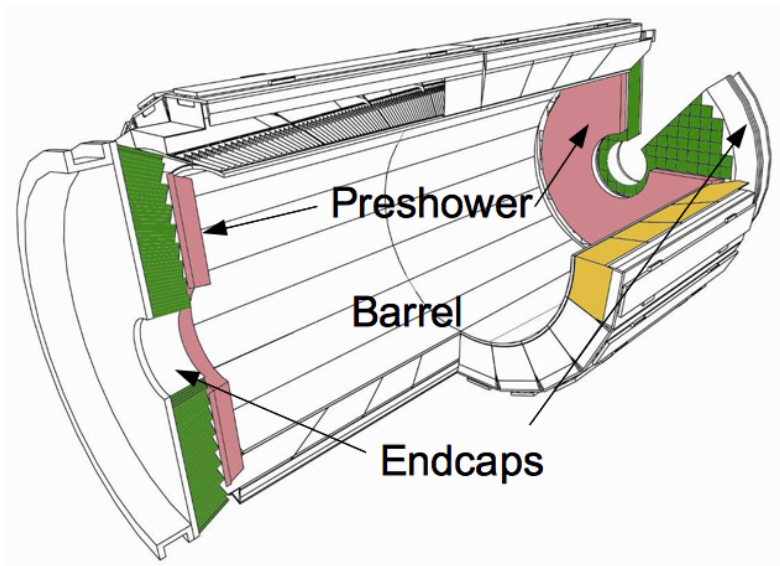


Figure 2.12: The CMS ECAL layout. The detector is 7.8 m long and has a diameter of 3.5 m. The total crystal volume is 8.14 m<sup>3</sup> in the ECAL barrel and 3.04 m<sup>3</sup> in the ECAL endcaps. This corresponds to a total crystal weight of about 90 t.

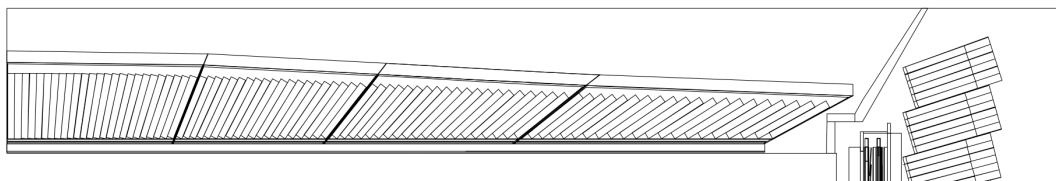


Figure 2.13: Cross sectional view of the upper part of the ECAL. The component on the left-hand side of this figure is an ECAL supermodule, which is about 3 m in length and 0.5 m in height. On the right-hand side of the figure the ECAL barrel-endcaps transition region is visible along with the upper part of the ECAL endcaps and the ECAL preshower.

(see Fig. 2.13) contains  $85 \times 20$  crystals in  $\eta$ - $\phi$  and is further divided in 4 “modules”. The “trigger towers” (TT) consist of  $5 \times 5$  crystals, so that a SM contains  $17 \times 4$  TT in  $\eta$ - $\phi$ .

The ECAL endcaps are two identical detectors on each side of EB covering the pseudo-rapidity range  $1.479 < |\eta| < 3.0$ . The longitudinal distance between the interaction point and the EE envelope is 315.4 cm. The EE crystals are identical and they are grouped in mechanical units of  $5 \times 5$  crystals that are called “supercrystals” (SC). Each endcap is divided in two halves, or “Dees”. There are 3 662 crystals per Dee, contained

in 138 standard SCs and 18 special partial SC on the inner and outer circumference. Trigger towers (TT) in the EE do not contain always the same number of crystals, which varies between 25 at  $|\eta| \sim 1.5$  and 10 at  $|\eta| \sim 2.8$ . The EE crystal length is 220 mm, which corresponds to  $24.7 X_0$ .

The ES is a sampling calorimeter with two sensitive layers after approximately 2 and 3  $X_0$  respectively. It uses lead radiators to initiate and silicon strip sensors to sample the shower. It is placed in front of EE within a fiducial region  $1.653 < |\eta| < 2.6$ . Its main purpose is the identification of neutral pions. The total ES thickness is 20 cm and corresponds to about 3  $X_0$  at  $\eta = 1.653$ .

### 2.3.3 ECAL Photodetectors, Electronics and Trigger

The choice of the ECAL photodetectors is driven by the features of the CMS detector and the LHC environment. The photodetectors should tolerate the radiation conditions in which they operate, perform adequately in the 3.8T-magnetic field of the solenoid and provide adequate electronic gain for the small signals from the lead tungstate. These considerations have lead to the choice of avalanche photodiodes (APDs) in the EB and vacuum phototriodes (VPTs) in the EE. Each crystal in the EB has  $25 \times 5 \text{ mm}^2$  APDs and each crystal in the EE has 1 VPT, attached to the rear of the crystals.

The photodetector signals are further processed by the front-end and the off-detector electronics. The front-end electronics amplify the photodetector pulses, digitize them at the LHC bunch crossing rate, calculate trigger primitives, buffer the data until the trigger decision is available and send the data to the off-detector electronics. The front-end electronics are located on the detector, whereas the off-detector electronics are housed in underground counting rooms and communicate with the front-end electronics through 90-m-long high-speed optical links, operated at 800MB/s.

The calorimeter Level-1 trigger uses ECAL trigger primitives. Each trigger primitive

refers to one TT. It contains the sum of the deposited transverse energy together with a bit describing the lateral extension of the electromagnetic shower.

The ECAL data size is reduced to about 100 kB per event. In order to achieve this data reduction a selective readout algorithm is implemented by the Selective Readout Processor (SRP), which is an off-detector-electronics component. The term “selective readout” refers to a set of algorithms that receive the trigger primitives and decide the level of suppression with which each TT is finally read out. In the current implementation for EB the trigger primitive transverse energy ( $E_T$ ) is compared to 2 thresholds and the TT is classified as high interest if its energy exceeds the high  $E_T$  threshold, medium interest, if its energy is between the high and the low  $E_T$  threshold, and low interest if its energy is lower than the low  $E_T$  threshold. High interest towers along with all their neighbouring TT (i.e. 9 TT in total) are readout without suppression. Medium interest TT are readout without suppression too. Low interest towers are readout with a zero suppression threshold, unless they are neighbours of a high interest TT. The implementation in the EE is very similar, but slightly more complicated due to the complex overlapping mapping of trigger towers and onto the supercrystals.

### 2.3.4 Calibration and Performance

The ECAL energy resolution has been measured in an electron beam in 2004 and 2006 for 9 complete barrel SM fully equipped with electronics in the CERN H4 beam, which provided high energy electrons in the range 20-250 GeV. The measured energy resolution can be parameterised in the form:

$$\left(\frac{\sigma}{E}\right)^2 = \left(\frac{S}{\sqrt{E}}\right)^2 + \left(\frac{N}{E}\right)^2 + C^2 \quad (2.1)$$

where  $S$  is the stochastic term,  $N$  the noise and  $C$  the constant term. The noise term is due to electronics noise. This noise is independent of the energy of the physical object.

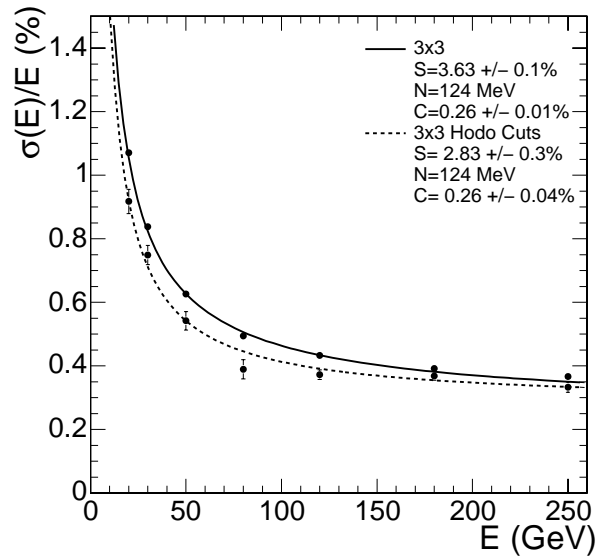


Figure 2.14: The ECAL supermodule energy resolution in the test beam (from [46]). The upper continuous curve corresponds to events taken with a  $20 \times 20 \text{ mm}^2$  trigger and reconstructed using a containment correction that is described in more detail in [46]. The lower dashed curve corresponds to events selected to fall within a  $4 \times 4 \text{ mm}^2$  region. The energy is measured in a  $3 \times 3$  crystal array with electrons impacting the central crystal.

The constant term is the term that limits the ECAL performance for high energies. In the test beam it is dominated by longitudinal non-uniformity of light collection. In collision data crystal-to-crystal intercalibration errors will be the most important contribution. Finally, the stochastic term is due to statistical fluctuations in the output signal and fluctuations in the lateral containment of the electrons. The obtained values of these parameters in the test beam are shown in Fig. 2.14.

The excellent resolution measured in test beam will be approached for unconverted photons as the intercalibration precision is improved. For electrons the resolution *in situ* is dominated by the effect of the tracker material.

The ECAL energy resolution has been extensively studied with data [101, 102]. The observations are in good agreement with the expectations from simulation for start-up calibration conditions as shown in Fig. 2.15.

The ECAL calibration has as target the achievement of the most accurate measure-

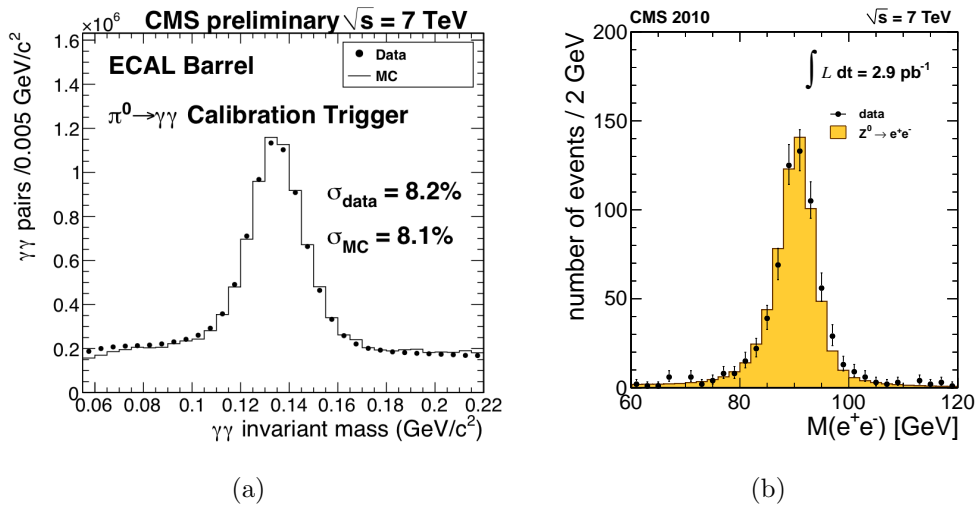


Figure 2.15: ECAL performance demonstrated with the measurement of physical processes. (a) The  $\pi^0 \rightarrow \gamma\gamma$  resonance for photons reconstructed in the ECAL barrel [102]. (b) The  $Z \rightarrow ee$  resonance [72].

ment possible of the energy of electron and photons. The reconstructed energy can be calculated using the crystal amplitudes  $A_i$  and the following formula:

$$E_{e,\gamma} = G \times \mathcal{F} \times \sum_i c_i \times A_i. \quad (2.2)$$

In this formula the factor  $G$  refers to a global absolute scale. Test beam studies provided a good starting value for  $G$ , which has subsequently been improved using reconstructed  $\pi^0$ s in data. The factor  $\mathcal{F}$  takes account of radiation in the tracker material and the effects of clustering.

The intercalibration coefficients,  $c_i$ , refer to the channel-to-channel response variation. An initial estimation of them can be done with laboratory measurements of crystal light yield, test beam and cosmic studies. With the first collision data, more accurate estimation was obtained imposing  $\phi$ -independence of deposited energy in the calorimeter, using neutral pions etc [102].

## Summary

The LHC is a high luminosity hadron collider that can collide proton beams in centre-of-mass energy relevant to the physics of the electroweak symmetry breaking. The LHC in 2010 was colliding protons at 7 TeV centre-of-mass energy and delivered about 40  $\text{pb}^{-1}$  of integrated luminosity. CMS is a general purpose detector designed to measure particles produced in LHC collisions. Its design is based on a superconducting solenoid magnet that surrounds the inner tracking and the electromagnetic (ECAL) and hadronic (HCAL) calorimeters. The magnet iron yoke is instrumented with muon detectors covering most of the  $4\pi$  solid angle. Forward calorimeters extend the solid angle coverage assuring good hermeticity. The CMS ECAL is a lead-tungstate scintillating-crystals electromagnetic calorimeter designed to fit in the overall CMS layout and provide good energy resolution for electrons and photons.

# Chapter 3

## Electrons in CMS

*No, no, you're not thinking, you're just being logical.*

Niels Bohr

Electrons are particles of high importance in a hadron collider environment because they provide signatures that are easy to identify and their energy is measured in the electromagnetic calorimeter with good resolution. For this reason, special attention is given in having efficient electron reconstruction algorithms and effective identification that will enable the collection of high purity electron samples with small efficiency loss. In this chapter an overview of the CMS electron algorithms and identification variables is given and the sources of prompt electrons and their backgrounds in hadronic collisions are discussed.

### 3.1 Electron Trigger and Electron Reconstruction in CMS

Events with one or more electron signatures may be selected by the CMS trigger and recorded for further study. The electron reconstruction used in subsequent analysis

(“offline”) is almost exactly the same as that used in the High Level Trigger (“online”).

### 3.1.1 Triggering on Electrons in CMS

The CMS trigger (see also Section 2.2.6) has the capability to select events with electron-like signatures. The selection of electrons by the trigger proceeds in two steps which are outlined below.

In the first step, the Level-1 trigger selects events containing a high- $E_T$  electromagnetic shower in the ECAL. This is performed by a sliding  $3 \times 3$  trigger tower window technique, which identifies high- $E_T$  trigger towers. The Level-1 electromagnetic trigger object  $E_T$  is the  $E_T$  sum of a trigger tower and its highest- $E_T$  neighbour. An isolation requirement, based on the amount of energy deposited in the trigger towers around the central one, is used to separate the Level-1 trigger candidates into isolated and non isolated candidates. Finally, the four most energetic candidates from each category are used in the final Level-1 trigger decision.

In the second step, the High Level Trigger (HLT) takes the events that pass the Level-1 trigger and decides whether or not the event is to be written to permanent storage. In the HLT, raw data from regions of the ECAL around Level-1 electromagnetic candidates are unpacked and clustered into “superclusters” with the same algorithms as are used in full offline reconstruction. Trigger thresholds are imposed on the  $E_T$  calculated from these superclusters. The HLT object so far can become a seed for an HLT photon object. Further requirements on the cluster shape and/or the isolation of the supercluster can be imposed. Specifically for electron triggers the supercluster is requested to be matched to hits in the inner tracking detectors. If the hits are found they serve as a seed for track reconstruction, which is performed with a Kalman Filter algorithm [64]. Given the track, further requirements in the track-supercluster geometrical matching can be applied.

### 3.1.2 Electron Reconstruction in CMS

The electron reconstruction algorithm starts by identifying clustered depositions of energy in the ECAL, which are subsequently matched to reconstructed tracks.

Electron reconstruction starts by reconstructing clusters seeded by a local maximum energy deposition passing a threshold cut. These clusters are used to form superclusters in order to take into account the fact that electrons may radiate in the tracker material, resulting in an ECAL energy profile that has a spread in  $\phi$ . This is a significant effect, since the material budget of the tracker, shown in Fig. 3.1, peaks at pseudorapidity  $\eta \sim 1.5$  at about  $2 X_0$ . In the ECAL barrel the “hybrid” algorithm [46] is used, which groups dominos of 5 crystals in  $\eta$  within a  $\phi$  window extending to  $\pm 0.3$  rad around the highest-energy crystal. A domino threshold and a sub-cluster threshold control which dominoes get accepted into the supercluster. In the ECAL endcaps the algorithm collects the energy deposited in the crystals within  $5 \times 5$  matrices. The supercluster is formed by grouping such clusters whose position lies within a  $\phi$  road extending to  $\pm 0.3$  rad in  $\phi$  and  $\pm 0.07$  in  $\eta$  centred on a local maximum. Superclusters with transverse energy greater than 4 GeV and passing a hadronic veto cut are used in the next step of electron reconstruction. The hadronic veto is defined by the ratio of the hadronic energy in HCAL towers whose centre lies within a radius of  $\Delta R = 0.15$  with respect to the supercluster position<sup>1</sup> over the supercluster energy (H/E). The cut value that is applied is such that  $H/E < 0.15$ .

The next step is the geometrical matching of the superclusters with trajectory seeds built from pairs or triplets of hits in the pixel and inner strip tracker layers. It is required that both hits are matched in the case of a trajectory seed composed of a pair of hits and two out of three hits are matched in the case of a trajectory seed composed of three hits. The way the matching is done is explained in the following. The supercluster position is extrapolated towards the primary vertex on a helical path whose bending

<sup>1</sup>This is the energy weighted position of the supercluster as defined in [46].

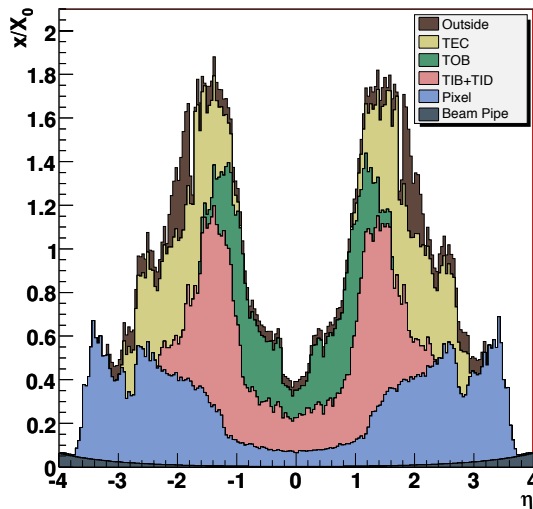


Figure 3.1: The CMS Inner Tracking System material budget in radiation lengths as a function of the pseudorapidity ( $\eta$ ) from [46].

is calculated from the supercluster  $E_T$ . A first compatible hit is then looked for in the innermost tracker layers within a loose window in  $\phi$  and  $z$  (or in the transverse radius  $r_T$  in the forward region) taking into account both charge hypotheses. Once the first hit is found, this information is used to improve the helical path parameters and a second hit in the next tracker layers is looked for using smaller windows. The currently used window parameters in the supercluster-tracker hit matching are shown in Table 3.1. The matched trajectory seed initiates a dedicated electron track building algorithm, which is based on a combinatorial Kalman Filter with a dedicated Bethe-Heitler modelling of bremsstrahlung emission [65]. The hits collected in this way are passed to a Gaussian Sum Filter (GSF) for the final estimation of the track parameters, which in effect approximates the energy loss in each layer by a weighted sum of Gaussian distributions. The track parameters can be approximated by using the mean of these components or the highest weight component, which will be referred to as the *mode*. It has been shown (see Ref. [66]) that the mode estimate is more accurate than the mean estimate and hence the mode estimate is used to measure electron track parameters.

The electron candidates that are built from the superclusters and their associated GSF tracks are further preselected to form a reconstructed GSF electron by demanding good

Table 3.1: Seed matching windows definitions used in electron reconstruction (offline) and in the “start-up” trigger configuration. Asymmetric  $\phi$  windows are shown here for the positive charge hypothesis. In the offline reconstruction the first window in  $\phi$  is (supercluster)  $E_T$ -dependent and it is shown for an electron with  $E_T$  10 and 35 GeV.

	1st window		2nd window			
	$\delta z$ or $\delta r_T$ (cm)	$\delta\phi$ (rad)	$\delta z$ (cm)	$\delta r_T$ (PXF) (cm)	$\delta r_T$ (TEC) (cm)	$\delta\phi$ (rad)
Offline, 10 GeV	$\pm 5\sigma_z$	[-0.14,0.08]	$\pm 0.09$	$\pm 0.15$	$\pm 0.2$	$\pm 0.004$
Offline, 35 GeV	$\pm 5\sigma_z$	[-0.05,0.03]	$\pm 0.09$	$\pm 0.15$	$\pm 0.2$	$\pm 0.004$
Start-up	$\pm 5\sigma_z$	[-0.04,0.08]	$\pm 0.05$	$\pm 0.08$	$\pm 0.11$	$\pm 0.004$

track-supercluster matching as defined by the following criteria:

- $|\Delta\eta_{in}| \equiv |\eta_{sc} - \eta_{in}^{extr}| < 0.02$ , where  $\eta_{sc}$  is the energy weighted position in  $\eta$  of the supercluster and  $\eta_{in}^{extr}$  is the  $\eta$  coordinate of the position of closest approach to the supercluster position, extrapolating from the innermost track position and direction.
- $|\Delta\phi_{in}| \equiv |\phi_{sc} - \phi_{in}^{extr}| < 0.15$ , where  $\phi_{sc}$  is the energy weighted position in  $\phi$  of the supercluster and  $\phi_{in}^{extr}$  is the  $\phi$  coordinate of the position of closest approach to the supercluster position, extrapolating from the innermost track position and direction.

The few electron candidates that fail these preselection criteria ( $\sim 1\%$  for isolated electrons) are still allowed to be promoted to GSF electrons if they pass a loose multivariate selection that was developed in the context of the CMS particle flow algorithm and it is described in detail in Ref. [76]. This choice is made in order to maintain consistency with the CMS particle flow objects and has been verified that it does not affect the study that is presented here.

The electrons that are reconstructed with the procedure just described are known as ECAL-driven electrons because the algorithm starts from energy depositions in

the ECAL. Another algorithm starts from tracks (tracker-driven electrons) [77]. The tracker-driven algorithm is more efficient in finding low- $p_T$  electrons and performs better in reconstructing electrons in jets, whereas the ECAL-driven algorithm is more efficient for high- $p_T$  electrons and performs better in reconstructing their energy. In this study, only electrons reconstructed by the ECAL-driven algorithm will be considered. The reason for this choice is that the signal acceptance and the reconstruction efficiency can be cleanly defined in terms of ECAL superclusters (see Chapter 6).

## 3.2 Backgrounds to Prompt Electrons

The electron reconstruction algorithm will not only pick up patterns that are created by prompt electrons but also similar patterns that are produced by other processes. The main physical mechanisms that produce electron-like patterns are the following:

- **Charged hadrons that shower early in the ECAL.** For example a charged pion will leave a track and if the hadronic shower starts early in the ECAL the deposited energy can be mistaken for an electromagnetic shower. In the extreme case of a charge exchange reaction:

$$\pi^- + p \rightarrow n + \pi^0 \quad \text{or} \quad \pi^+ + n \rightarrow p + \pi^0$$

the produced  $\pi^0$  will decay to a photon pair, resulting in an electromagnetic shower that may be almost indistinguishable from an electron shower. Electron candidates that are created by early showering hadrons have a non-radiating track and a calorimetric energy measurement that tends to underestimate the energy of the interacting hadron due to partial shower containment in the ECAL and the fact that the ECAL pion response is lower than the electron response.

- **$\pi^\pm$ - $\pi^0$  overlap.** The charged and neutral hadrons within a jet may have little spatial separation. If the electromagnetic cluster resulting from the pair of photons of a  $\pi^0$  is matched geometrically to a track from a charged hadron, then an electron candidate is formed. These electron candidates tend to have a large E/p ratio, where E is the energy deposited in the ECAL and p the track momentum. This is due to a combination of the fact that the pion  $p_T$  spectrum falls steeply and the electron energy measurement is made with the ECAL cluster.
- **Electrons from hadronic decays.** Semileptonic decays of heavy flavour quarks produce real electrons, which are background in many physics studies. These electrons are less isolated than the prompt electrons from W decays. Moreover, electrons from b-quark decays have a significant impact parameter due to the fact that the life times of hadrons that contain a b quark are such that on average they decay a measurable distance away from the interaction point.
- **Electrons from conversions.** Neutral pion disintegration to photons and the subsequent conversion of one or both of them in the tracker material will produce real electrons. These electron candidates tend to have a track with missing inner hits, i.e. hits that a prompt electron would leave in the tracker layers that are close to the beam spot. Moreover, close to the candidate there is the conversion partner track, which, if it is successfully reconstructed, provides a powerful indication that the candidate comes from a photon conversion.

The jet cross section ( $\sim \mu\text{b}$ ) is huge when compared to the dominant source of prompt high- $p_T$  electrons, which is the  $W \rightarrow e\nu$  decay ( $\sim 10 \text{ nb}$ , see also Fig. 2.10). In a sample of reconstructed electrons after preselection and without any further selection criteria the vast majority of the reconstructed electrons come from jets.

A further source of electron candidates that is a significant source of background to  $W \rightarrow e\nu$  are the fake or real electrons arising from tau ( $\tau$ ) decay. Tau decay to

electron plus neutrinos gives an electron in the final state, which is however, low in  $p_T$  due to the kinematics of the three body decay. Hadronic  $\tau$  decays, which are also known as  $\tau$ -jets, are more collimated and more isolated than an average jet and hence they are more likely to produce reconstructed electrons. The correct modelling of this source of reconstructed electrons is important in order to obtain an unbiased estimate of the  $W \rightarrow e\nu$  cross section.

### 3.3 Electron Identification Variables

The most powerful handle for electron identification is isolation. Hadrons that are misidentified as electrons are usually accompanied by other particles nearby in contrast to prompt electrons that are well isolated. The isolation variables that are used in this study are defined in the following:

- Tracker isolation: the sum of the  $p_T$  of Kalman Filter tracks [64] reconstructed in the CMS tracker with  $p_T > 0.7$  GeV in a cone centred on the electron candidate direction within  $\Delta R < 0.4$  and with tracks pointing to a narrow strip in the  $\phi$  direction of width  $\Delta R = 0.015$  excluded. Cuts on the tracker isolation are applied on this track  $p_T$  sum divided by the electron candidate  $p_T$ .
- ECAL isolation: the sum of the energy deposited in the ECAL crystals around the centre of the electron supercluster within a cone  $\Delta R < 0.3$  and excluding a strip along  $\phi$  with total width of the size of 3 crystals. Only crystals with energy greater than 0.08 GeV in the ECAL barrel and  $E_T > 0.1$  GeV in the ECAL endcaps are considered. Cuts on the ECAL isolation are applied on this crystal  $E_T$  sum divided by the electron candidate  $p_T$ .
- HCAL isolation: the sum of the energy deposited in the HCAL towers in a hollow cone of  $0.15 < \Delta R < 0.3$  centred on the electron supercluster. The HCAL

towers that are summed have energy more than 0.7 GeV in the HCAL barrel and 0.8 GeV in the HCAL endcaps. Cuts on the HCAL isolation are applied on this tower  $E_T$  sum divided by the electron candidate  $p_T$ .

Accidental track-supercluster matching can be reduced by applying tighter cuts on the  $\Delta\eta_{in}$  and  $\Delta\phi_{in}$  variables that were defined in the discussion of electron preselection in Section 3.1.2. Moreover, tightening the demand on the H/E variable that was also used in preselection provides some discrimination against electron candidates where the track results from a charged pion, since even if the hadronic shower starts in the ECAL, some energy will tend to leak into the HCAL. Shower shape properties can be also used to discriminate prompt electrons from jets, since an electron shower has a smaller lateral width than a hadronic shower or showers induced by photon pairs from  $\pi_0$  decays. In CMS, the shower shape variable used is defined as the root mean square of the shower width in  $\eta$  in a  $5\times 5$  crystal array centred on the highest-energy crystal of the supercluster (seed crystal):

$$\sigma_{\eta\eta} = \frac{\sum_{i \in 5 \times 5} w_i (\eta_i - \eta_{seed})^2 \Delta\eta_{xtal}^2}{\sum_{i \in 5 \times 5} w_i}, \quad (3.1)$$

where the distance of crystal  $i$  from the seed crystal,  $\eta_i - \eta_{seed}$ , is multiplied by the crystal width in  $\eta$ ,  $\Delta\eta_{xtal}$  and the weight for a crystal  $i$  with energy  $E_i$  is defined to be:

$$w_i = \max(0, 4.7 + \log(E_i/E_{5 \times 5})),$$

where by  $E_{5 \times 5}$  is defined the total energy in the  $5 \times 5$  array around the seed crystal. This implementation of the weighted energy sum is such that it puts a cutoff in the crystal energy that is used in the shower shape calculation, which corresponds approximately to  $E_i/E_{5 \times 5} > 0.9\%$ . This cutoff makes the width variable definition more robust to effects like noise and hence improves the electron identification performance.

Information from tracker data provides extra handles to identify electrons from photon conversions in the tracker material. This is a considerable source of non prompt electrons because of the large material budget of the tracker that exceeds one radiation length. Electrons from photons converting further into the tracker than the first sensitive layer result in tracks without hits in the first layers. This can be quantified by extrapolating the track to the beam line and counting how many layers before the first recorded hit should have been transversed (number of missing inner hits). Moreover the other leg of a conversion may be reconstructed as a track. Conversion partner tracks can be sought in the collection of Kalman Filter tracks that are within  $\Delta R < 0.3$  of the electron candidate and have charge opposite to the GSF track of the electron. For each of these tracks the following quantities are defined:

- $\Delta \cot \theta \equiv \cot(\theta_{KF}) - \cot(\theta_{GSF})$ , where  $\theta_{KF}$  is the polar angle of the Kalman Filter track of the conversion partner candidate and  $\theta_{GSF}$  is the polar angle of the GSF track of the electron.
- Dist is defined as the two-dimensional distance (x-y plane) between the two tracks when the Kalman Filter track in question and the electron's GSF track would be parallel when extrapolated. This distance is calculated analytically by a simple intersection of helices method using the track parameters of the two tracks as input. Figure 3.2 shows the definition of Dist, as well as the sign convention used.

It is important to avoid picking up the Kalman Filter track that corresponds to the one made by the electron itself. This track is identified by looking at all tracks in a cone of  $\Delta R < 0.3$  around the electron, and for each Kalman Filter track, we define the fraction of shared tracker hits between the electron GSF track and the Kalman Filter track as:

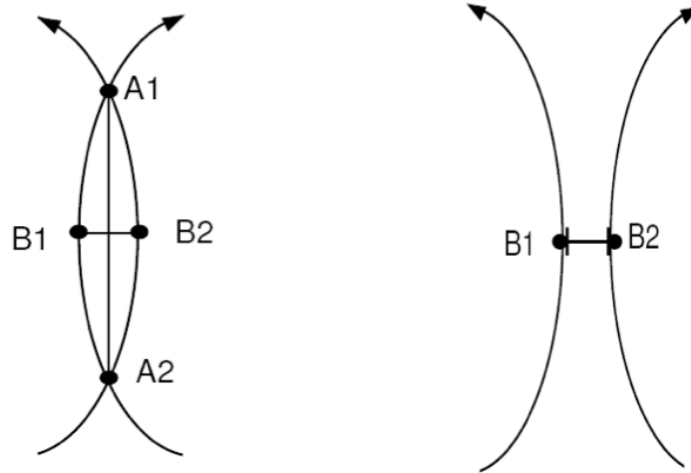


Figure 3.2:  $Dist$  is the two dimensional distance between points B1 and B2 in the x-y plane as seen above. At these points, the two tracks from the photon conversion are parallel.  $Dist$  is defined to be negative when the two tracks overlap, and is positive otherwise.

$$\frac{\text{Number of inner hits}}{\min(\text{Number of inner Kalman Filter track hits, Number of inner GSF track hits})}$$

The Kalman Filter track whose fraction of shared hits with the electron GSF track is greater than that of any other Kalman Filter track in the cone around the electron and is also greater than 0.45 is considered to be the Kalman Filter track made by the electron and is not considered as a possible conversion partner to the GSF track.

Electrons with a conversion partner track satisfying:

$$|Dist| < 0.02 \text{ cm and } |\Delta \cot \theta| < 0.02, \quad (3.2)$$

are rejected as electrons from conversions. This choice is made on grounds of the very high conversion rejection that can be achieved with these cuts (more than 90% of electron fakes from  $\pi_0$  are rejected) combined with the fact that a relatively small fraction of real electrons (less than 10%) have any conversion partner track at all.

Table 3.2: Summary of the simulated samples details that were used for this study. PYTHIA6 cross sections ( $\sigma$ ) for electroweak processes are scaled to the POWHEG cross sections in the data-simulation comparison plots.

Process	Generator	$\sigma$ (pb)	Events
EWK processes:			
$W^+ \rightarrow e^+\nu$	POWHEG	5,825	700,000
$W^- \rightarrow e^-\bar{\nu}$	POWHEG	3,954	700,000
$Z \rightarrow ee, m_{ee} > 20$ GeV	POWHEG	1,631	1,200,000
$W \rightarrow \tau\nu$	PYTHIA6+TAUOLA	7,899	2,000,000
$Z \rightarrow \tau\tau, m_{\tau\tau} > 20$ GeV	PYTHIA6+TAUOLA	1300	2,000,000
$t\bar{t}$	PYTHIA6	94	500,000
Light Flavour Jets:			
$20 < \hat{p}_T < 30$ GeV/c	PYTHIA6	$1.7 \times 10^6$	30,000,000
$30 < \hat{p}_T < 80$ GeV/c		$3.5 \times 10^6$	40,000,000
$80 < \hat{p}_T < 170$ GeV/c		$1.3 \times 10^5$	5,000,000
Heavy Flavour Jets:			
$20 < \hat{p}_T < 30$ GeV	PYTHIA6	$1.1 \times 10^5$	3,000,000
$30 < \hat{p}_T < 80$ GeV		$1.4 \times 10^5$	2,500,000
$80 < \hat{p}_T < 170$ GeV		9,442	1,200,000
$\gamma$ +jets	PYTHIA6	$1.9 \times 10^5$	1,200,000

### 3.4 Simulation of Events Containing Electron Candidates

Simulated samples of events have been used extensively both in the study of the electron selection and in the  $W \rightarrow e\nu$  cross-section measurement. There follows a short description of the relevant details of the event simulation.

The first stage of the simulation is the generation of events from relevant physical processes. The physical processes that were considered here are:

- Electroweak processes:  $W \rightarrow e\nu$ ,  $Z \rightarrow ee$ ,  $W \rightarrow \tau\nu$  and  $Z \rightarrow \tau\tau$ .
- Jet production, both from gluon and light flavour quarks, and from heavy flavour quarks simulated with  $\hat{p}_T$  range: 20-180 GeV/c. For the simulation of jets due to gluon and light flavour quarks (u, d, s) a special electromagnetic enrichment

procedure is used, which will be discussed in detail later in Section 3.4.1.

- $\gamma$ +jet events simulated with  $\hat{p}_T$  range: 15-300 GeV/c.
- inclusive  $t\bar{t}$ .

Events from electroweak processes were generated with POWHEG [79, 80], apart from processes with taus in the final state. For the latter, PYTHIA6 [73] is used interfaced with TAUOLA [103] for the correct description of tau decay. All the other samples were generated with PYTHIA6. A summary of the generated samples along with their cross sections is shown in Table 3.2. It has to be noted that the simulated W sample does not include properly contributions from  $W\gamma$  production. The scale of this effect is about 2 orders of magnitude smaller than the inclusive W production cross section [74] and this omission will not affect this study.

The second stage is the simulation of the interactions of the particles in the detector material, the tracking in the magnetic field, the energy deposition in electromagnetic and hadronic showers etc. The detector simulation is based on the GEANT4 framework, which is described in detail in Ref. [75].

Finally, the third stage is the emulation of the detector signal processing. This emulates the response time, the digitisation, the trigger and the readout. A comprehensive description of the detector simulation and the signal processing emulation can be found in Ref. [46]. The version of the software that was used for this study is CMSSW\_3\_1\_6patch4.

### 3.4.1 Simulation of Jet Background from Light Flavour Quarks and Gluons

The simulation of the background to prompt electrons from jets due to gluons or light flavour quarks is particularly difficult and will be discussed here in more detail.

The main problem in the simulation of this background component stems from a combination of the very high jet cross-section production and the fact that only a tiny fraction of jets have electron-like properties. Hence in order to simulate enough jets that fake electrons, i.e. comparable to the number seen in the data used for this study, a large number of events has to be simulated. This task proves to be too demanding in terms of both simulation time and storage space and a shortcut has to be used. This shortcut is the implementation of a procedure, which is such that the events are examined at the stage of the event generation and only events likely to result in an electromagnetic candidate are propagated to detector simulation.

The generated jet events are searched for properties that are indicative of (fake or real) isolated electromagnetic showers or isolated hadrons that fell in the CMS tracker and ECAL acceptance ( $|\eta| < 2.4$ ). For the former case the criterion that is taken into account is the existence of electrons or photons with  $E_T > 5$  GeV, which have neighbouring particles such that an isolated ECAL cluster with  $E_T > 20$  GeV has a high probability to be reconstructed. For the latter case the criterion is the existence of an isolated charged pion or hadron with  $E_T > 20$  GeV.

This enrichment procedure makes possible the generation of simulated samples of jets due to gluons and light flavour quarks with reasonable integrated luminosity ( $\sim 20 \text{ pb}^{-1}$ ) for the studies that are presented here. However, it has an associated efficiency in selecting events with jets that will be finally reconstructed as electrons. It is estimated from comparisons with small jet samples that were generated without applying this enrichment procedure that the jet contribution in an inclusive electron sample is underestimated by a factor of about 1.4 if the electromagnetic enrichment procedure is used. This factor is expected to be lower for isolated electrons. In all the plots that are to be shown in this study with the simulation sample distributions normalised to integrated luminosity of the data sample the gluon/light-flavour-quark jet component is rescaled with a multiplicative factor ( $\geq 1$ ), which is such that that the agreement between the

distributions of the transverse missing energy ( $\cancel{E}_T$ ) in data and simulation is the best possible, with the figure of merit being a  $\chi^2$ -function minimisation. This multiplicative factor is about 1.2 when the electron selection is applied to the single electron sample with electron  $E_T > 20$  GeV and without any further kinematic or  $\cancel{E}_T$  requirements.

## Summary

Electron finding algorithms in CMS match ECAL energy depositions to tracks to form an electron candidate. The majority of the electron candidates in a single electron sample are not prompt electrons but come from background processes, mainly from jets that are misidentified as electrons. Prompt electron properties like isolation, tight track-ECAL cluster matching, shower shape and shower length can be used to define an electron selection. The use of these variables to construct electron selections that can be used to select pure electron samples with high efficiency will be described in the next chapter.

# Chapter 4

## Electron Selection

*“Excellent!” I cried.*

*“Elementary,” said he.*

“The Crooked Man”, Sir Arthur Conan Doyle

### 4.1 Classification in the Context of Classical Statistics

Electron selection is a specific case of a classification problem. The latter, in the context of classical statistics (e.g. see [67]) is treated using hypothesis testing concepts. More specifically, the null hypothesis,  $H_0$ , is that the candidate is a prompt electron and the alternative hypothesis,  $H_1$ , is that the candidate is due to some process that is background to prompt electrons.

The analysis proceeds by defining a test statistic,  $t(\vec{x})$ , which is a function of the properties of the candidate,  $\vec{x}$ , that are considered to be useful in discriminating it from other non-prompt electron objects. The distribution of  $t(\vec{x})$ , given that  $H_0$  holds,  $f(t; H_0)$ , can be used to make the inference. This can be done if the experimenter decides

in advance a specific set of values for  $t(\vec{x})$ :  $\{t\} \in \mathcal{T}(\alpha)$  with  $\alpha = \int_{\mathcal{T}(\alpha)} f(t; H_0) dt$ , such that if the observed value for  $t$  is included in the set  $\mathcal{T}(\alpha)$ , then  $H_0$  is rejected. The parameter  $\alpha$ , which is also known as the “size” of the test, is the probability that the test rejects  $H_0$ , although  $H_0$  is true. Another parameter that characterises a hypothesis test is the power of the test,  $1 - \beta$ , where  $\beta$  is the probability that  $H_0$  is accepted as true, while in fact  $H_1$  is the correct hypothesis. In the particular problem of electron selection the significance of the test,  $\alpha$ , is related to the signal efficiency of the particular selection and the power of the test,  $1 - \beta$ , is related to the background rejection that we can achieve with this selection.

The performance of a particular test is given by the interplay between the power and the significance of the test and depends on the choice of the test statistic on which the test is performed. The Neyman-Pearson Lemma (see e.g. Ref. [67]) states that the most optimal test statistic, i.e. the one that gives the highest power for a given significance, is the likelihood ratio:

$$t(\vec{x}) = \frac{L(\vec{x}; H_0)}{L(\vec{x}; H_1)},$$

where  $L(\vec{x}; H_0)$  ( $L(\vec{x}; H_1)$ ) is the likelihood of the observed candidate properties  $\vec{x}$  under the assumption of  $H_0$  ( $H_1$ ).

Despite the mathematical strength of the Neyman-Pearson Lemma, in practice it is often difficult to construct the likelihood and it is more common to use some ansatz for the functional form of the test statistic, which is then optimised such that the optimum combination of power and significance is achieved. One example of this ansatz method to approximate the optimal test statistic that is widely used in many classification problems is the multilayer perceptron (MLP), which is a specific case of an artificial neural network. An MLP with 2 layers uses an ansatz of the form:

$$t(\vec{x}; \{\vec{w}\}) = \sigma \left( \sum_j \left( w_j^{(2)} \sum_i \vec{w}_j^{(1)} \cdot \vec{x} \right) \right), \quad (4.1)$$

where  $\sigma$  denotes a linear or non-linear function (referred to as “activation” function) and  $\{\vec{w}\}$  is a set of weights. MLP-based classification includes an iterative technique to optimise the weights, which is known as MLP learning rule (see for example Ref. [68] for more details).

### 4.1.1 Cut-Based Analysis and Cut Tuning

Neural networks and other similar complex classifiers have the potential of approximating the likelihood ratio very well, however, they are usually not appropriate for early data analyses, where the attention is shifted from the best performing classification to the commissioning of the reconstruction objects and the quick identification and treatment of data-simulation discrepancies. This is the reason behind the popularity in high energy physics of a much simpler classifier based on cuts on selection variables (cut-based analysis). The cut-based analysis strategy consists of constructing a test statistic of the following functional form:

$$t(\vec{x}; \vec{c}) = \prod_i H(c_i - x_i), \quad (4.2)$$

where  $\vec{c}$  is the set of cut values whose values have to be optimised and  $H$  denotes the Heaviside function:

$$H(y) = \begin{cases} 0 & \text{if } y < 0 \\ 1 & \text{if } y \geq 0 \end{cases}$$

The objective of the cut-based analysis tuning is to derive sets of cuts that give the highest background rejection (i.e. the highest power of the test) for a given signal efficiency (i.e. given significance of the test). This corresponds to a constrained minimisation problem, where one has to find the set of cut values that minimises the following function

for a given number of signal events  $S$ :

$$f(\vec{c}; \{\vec{x}\}, S) = \sum_{j \in Bkg} t(\vec{x}_j; \vec{c}) + \lambda \left( \sum_{i \in Sig} t(\vec{x}_i; \vec{c}) - S \right). \quad (4.3)$$

In this function,  $\{\vec{x}\}$  denotes the set of data used for training the classifier, in other words candidates for which the class that they belong to is known. The first (second) sum is over candidates that belong to the background (signal) class and  $\lambda$  is the Lagrange multiplier that imposes the condition that the number of signal events,  $S$ , or equivalently the signal efficiency is kept constant.

The minimisation of Eq. (4.3) can proceed in various ways. The most common way in the literature to tackle this problem is the use of a local search technique such as conjugate gradient, steepest descend etc. This may be sometimes very time-consuming and some approximation has to be invented (e.g. as in the training of a neural network [68]). Suppose that a minimum of Eq. (4.3) has been found for a given signal yield,  $\vec{c}(S_\tau)$ , then another minimum for a slightly different signal yield  $S_\tau - \delta S$  can be written:

$$\vec{c}(S_\tau - \delta S) = \vec{c}(S_\tau) - \delta S \left. \frac{\partial \vec{c}}{\partial S} \right|_{S_\tau}, \quad (4.4)$$

or equivalently:

$$\vec{c}_{\tau+1} = \vec{c}_\tau - \vec{\epsilon}_\tau, \quad (4.5)$$

where we have used the shorthands  $\vec{c}(S_\tau - \delta S) = \vec{c}_{\tau+1}$ ,  $\vec{c}(S_\tau) = \vec{c}_\tau$  and  $\delta S (\partial \vec{c} / \partial S)_{S_\tau} = \vec{\epsilon}_\tau$ .

A simple approximation to the steepest descend method is to assume that

$$\vec{\epsilon}_\tau \equiv (\epsilon_0, \epsilon_1, \dots, \epsilon_{N-1}) \approx (0, 0, \dots, \epsilon'_J, \dots, 0), \quad (4.6)$$

i.e. to approximate the  $N$ -component vector with a single component vector. One solution is to find for fixed final signal yield the vectors  $(0, 0, \dots, \epsilon_k, \dots)$ , where  $k = 0, \dots, N - 1$  and select the one that culminates in the highest background rejection.

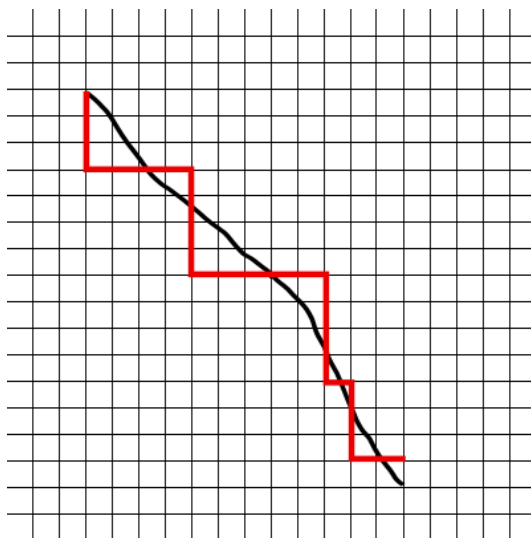


Figure 4.1: Schematic representation of the approximation to the steepest descent method that is discussed in Section 4.1.1. Each point in this 2-dimensional grid represents a pair of cut values. The ideal path that minimises Eq. (4.3) is the curved line. The approximation described in the text tries to approximate this line by moving one variable at a time creating a line composed of straight segments.

Essentially, what this method does is to approximate the steepest descent path, which is normally a curve in a multidimensional space, to another path that is composed by straight lines (see Fig 4.1 for a schematic representation in the case of 2 dimensions). This approximation will be used in the next section to construct a simple iterative algorithm to perform the selection tuning.

## 4.2 The Iterative Technique

The approximation to the steepest descent path that was discussed in the previous session is used for the construction of an algorithm for selection tuning, which will be referred to henceforth as the “Iterative Technique”. This technique, to the author’s knowledge, has never been used in the particle physics literature before. In order to apply this algorithm, two separate electron samples, one for signal and one for background, have to be defined - details on how this is done are given later on. The Iterative Technique uses these two samples and follows the steps:

1. Start from a configuration with no or very loose cuts.
2. Calculate a measure of background rejection,  $r_{bkg}$ , and set a target that is slightly higher than the current one:  $r_{bkg} + \delta r$ .
3. Try to achieve the new target in background rejection by making a tighter cut in a single variable. Find which variable can achieve this background rejection target with the smallest loss of signal and move this variable only to obtain a new selection.
4. Return to Step 2 and repeat the procedure.

As the iterations proceed, the continually updated list of cut values refer to a series of closely separated points in signal efficiency versus background rejection space.

The sets of cuts that the Iterative Technique produces correspond to selections with the highest possible background rejection for a given signal efficiency, as explained in the previous section. This result has been verified in a number of ways.

A popular method in the literature for solving optimisation problems like this is by implementing a technique based on a genetic algorithm. Genetic algorithms (see for instance Ref. [69]) are based on an idea inspired by Darwinian evolution. They start by finding an appropriate representation of a solution to the problem in question (“chromosome”) and defining a set of these representations, the “initial population”. This population is evolved by means of “mutation” and “cross-over” operators and after each iteration, usually referred to as “generation”, only configurations that fit some predefined quality criteria survive. In the cut-tuning procedure an appropriate representation of a solution is a vector that is composed of cut values. “Mutation” operation is simply a stochastic procedure of randomly moving one or more cut values in a chromosome. “Cross-over” operation randomly interchanges the cut values of two chromosomes, thus creating new chromosomes.

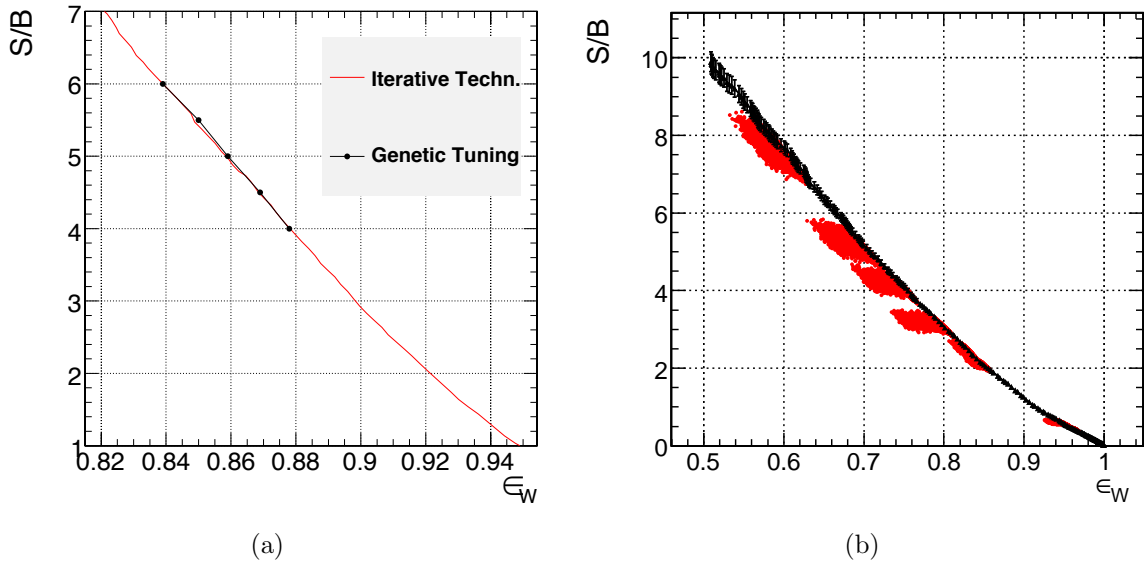


Figure 4.2: Tests of the Iterative Technique performance. (a) The performance of selections obtained by the Iterative Technique (continuous red line) is compared to the performance of selections optimised with a genetic algorithm implementation (black points connected with straight segments). (b) Performance of the iterative technique selections versus randomly generated points. See text for details.

In Fig. 4.2(a) the output of a genetic optimisation technique, set up to maximise the background rejection while keeping constant the signal efficiency is compared to the results of the Iterative Technique. The measure of background rejection that is used here is the ratio of the number of electrons in the signal sample over the number of electrons in the background sample (S/B). The variables that are used in this example to discriminate signal and background are  $\Delta\phi_{in}$ ,  $\Delta\eta_{in}$ ,  $\sigma_{in\eta}$ , H/E, Tracker, ECAL and HCAL isolations. This test was made using electrons that are reconstructed in the ECAL barrel with supercluster  $|\eta| < 1.4442$  and with corrected supercluster transverse energy,  $E_T > 30$  GeV. The signal electrons are taken from the simulated  $W \rightarrow e\nu$  sample and the background electrons from a simulated jet sample. In Fig. 4.2(a) it is shown that the points that are obtained with the Iterative Technique have the same performance, in terms of background rejection for a given efficiency, as the genetic algorithm optimised selections.

Two further tests were made to verify that, within statistical errors, the trajectory in background rejection versus efficiency space obtained with the iterative technique represents sets of cuts that give the highest background rejection for any given signal efficiency. These tests were performed with the simulated samples and the electron identification and isolation variables that were used in Ref. [70]. Reconstructed electrons from  $W \rightarrow e\nu$  samples were used as signal electrons. The background electrons were taken as all the reconstructed electrons in a comprehensive simulation of the background to  $W \rightarrow e\nu$  [70]. The most significant contribution to the background electron sample comes from jets.

In the first test a series of representative points on the trajectory (at signal efficiency 97%, 95%, 85%, 83%, 80%, 75%, 70% and 60%) were chosen. At each point the corresponding cuts were varied randomly and simultaneously so as to generate for each point 5000 new sets of cuts. The signal efficiency and S/B of each of these new selections was then plotted on the same axes as the trajectory. The result is shown in Fig. 4.2(b). The statistical errors on the trajectory points correspond to the signal and background sample size used ( $10 \text{ pb}^{-1}$ ). The randomly chosen selections give either less good performance or performance that is the same (within the statistical errors) as the selections whose performance is mapped out by the trajectory found by the algorithm.

In the second test a single point on the trajectory was chosen at signal efficiency 80%. Each cut value was then scanned, varying its value by small steps in both directions. The sub-trajectories mapped out by these variations were then plotted on the same axes as the trajectory given by the algorithm. The result for the case of the cut on the ECAL isolation variable for electrons with superclusters in the ECAL barrel and the  $\Delta\eta_{in}$  for electrons with superclusters in the ECAL endcaps is shown in Fig. 4.3. All other selection variables were also studied in this way and show the same behaviour. The statistical errors on the trajectory points correspond to sample statistics of  $10 \text{ pb}^{-1}$ . The scan points are shown by triangles, joined by a line and their starting point is a

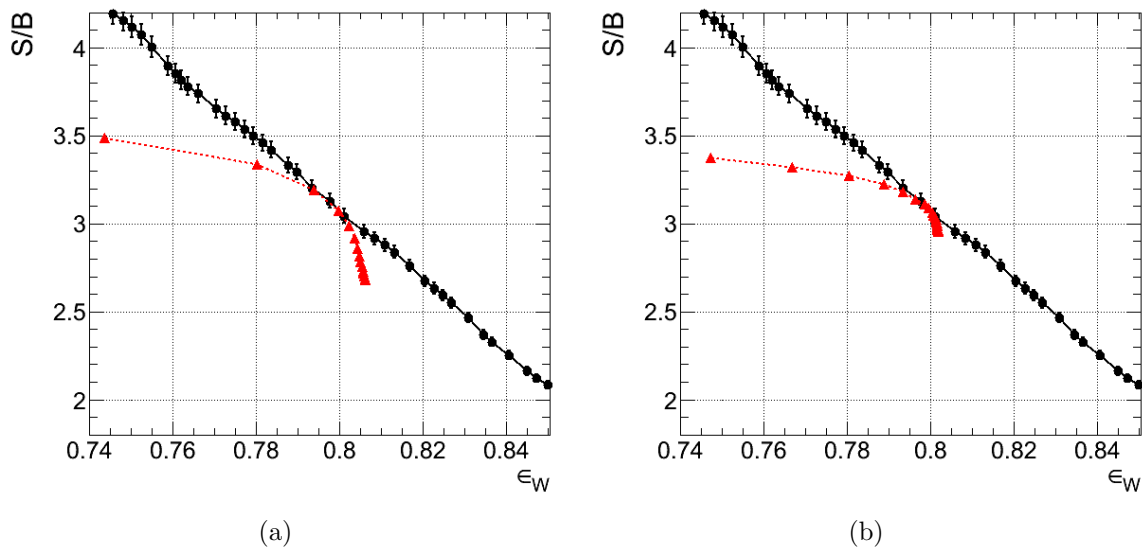


Figure 4.3: Tests of the Iterative Technique performance. A single set of cuts has been chosen and the cuts on a particular variable are moved generating the dashed line connecting the red triangles. These points perform worse than the Iterative Technique derived selections (back round markers) as expected. In (a) the variable is ECAL isolation for EB, whereas in (b) it is the  $\Delta\eta_{in}$  for EE.

configuration with the cut on the variable completely removed. As expected the selections obtained by the variations move away from the trajectory given by the algorithm in the direction of worse performance.

The performance of the Iterative Technique is affected by the step size. In each iteration the target at the background rejection is increased by a certain step that has to be chosen beforehand. The size of this step plays an important role in the algorithm performance. The step cannot be too big, because the steps in Fig. 4.1 will be big and the method will fail to approximate well the path of the steepest descend. On the other hand, very small steps will be affected by statistical fluctuations, and ultimately the demand to reduce the number of signal events by less than one. In Fig. 4.4(a) the effect of different step sizes is shown for the same samples and variables that were used in Ref. [70]. In these tests the step size was considered to be a fraction of the current background rejection measure. The two lower curves correspond to an increase of S/B of 5% and 3% respectively, whereas in the upper curve the step is 3% with the further demand

that the step never becomes smaller than 0.04 in S/B. This last choice was found to perform adequately for all the cases considered here and has been used as the default step size, unless it is explicitly stated otherwise.

Another factor affecting the algorithm performance is the choice of the initial cut values. The algorithm is guaranteed to follow the optimal path as long as it starts from a point that is already optimal. For this reason it has to be verified that if the starting is not optimal, then the algorithm will finally converge to the optimal path. This is illustrated in Fig. 4.4(b). It has to be highlighted that in the Iterative Technique the cut values can only become tighter and tighter and consequently if a cut starts from a value that it is too tight the algorithm will never converge to the optimal point. This facts motivates the use of a starting point without any cuts. In that case any optimal point can be reached by simply tightening some of the cut values. However, in practice this is not easy to achieve, since already at the electron preselection level there are some cuts, which are loose but there no guarantee that they are close to optimal. For this reason it is really important to demonstrate that the algorithm converges even if the starting point is not an optimal point.

The Iterative Technique has a number of advantages over other minimisation techniques. First of all, it is a straightforward and simple way to minimise Eq. 4.3 based on the well-known steepest descend algorithm. It is easy to implement and it is rather fast, since the outcome of each iteration is a different tuned selection, whereas with most other methods the same or similar amount of time is needed for the extraction of a single selection. Moreover, the selections that it produces are such that tighter selections correspond to electron samples that are always sub-sets of looser selections. On the negative side, the Iterative Technique will not perform adequately if the number of variables in the selection is too big, unless the training sample population is adequately large such that an adequately small step is possible. This downside is not relevant for the particular problem that is under study here and hence the advantages that were

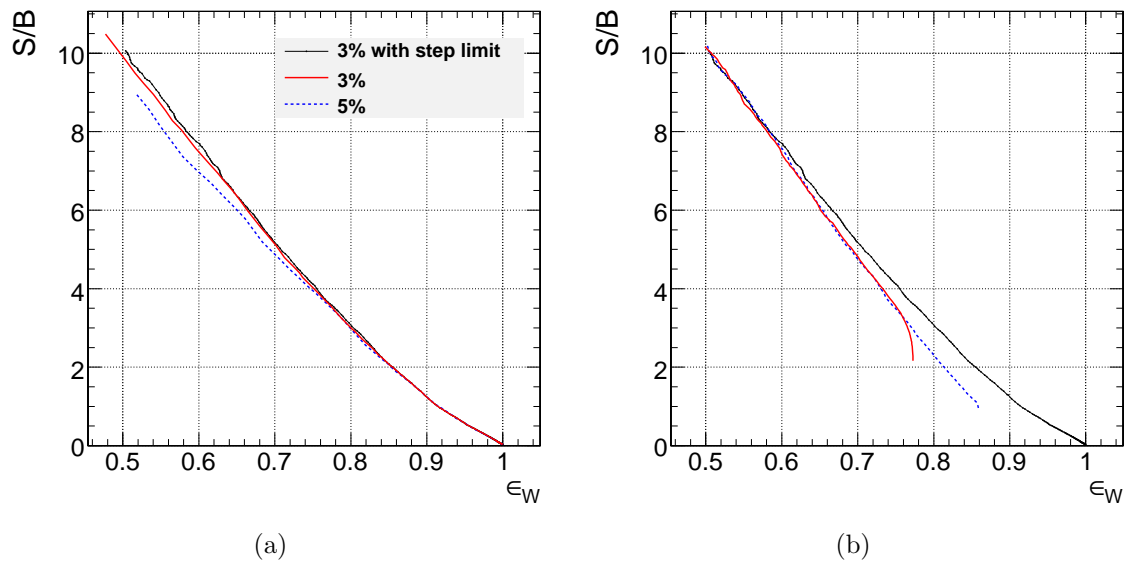


Figure 4.4: Dependence of the performance of the Iterative Technique on the parameters of the method. (a) Variation of the step in background rejection. (b) variation of initial cut values.

discussed previously have lead to the choice of this technique for the tuning of electron selections based on simple cuts.

### 4.3 Selection Tuning with the Iterative Technique

The Iterative Technique was used to derive benchmark electron selections to be tested with the 2010 LHC collision data. The first approach that was adopted was based on the simulated event samples that were described in Section 3.4.

In order to construct the signal and background samples of electrons that are to serve as inputs to the Iterative Technique a sample of events with a high- $E_T$  ( $E_T > 25$  GeV) reconstructed electron were selected. The signal sample was taken from simulated  $W \rightarrow e\nu$  samples and the background sample from jet,  $W \rightarrow \tau\nu$ ,  $Z \rightarrow \tau\tau$  and  $t\bar{t}$  simulated samples.

The selection variables used were those discussed in Chapter 3:

- isolation sums in Tracker, ECAL and HCAL normalised to the electron candidate  $p_T$
- $\Delta\eta_{in}$ ,  $\Delta\phi_{in}$ , H/E and  $\sigma_{in\eta}$

The conversion rejection criteria are applied on the signal and background samples once and they are not tuned. Three different combinations have been tried, which are listed here, ordered in increasing tightness:

- At most 1 missing inner hit
- At most 1 missing inner hit and no conversion partner track
- No missing inner hits and no conversion partner track

Starting from these three different cases the 3 isolation and 4 electron identification variables were tuned, subject to the condition that  $|\Delta\phi_{in}| > 0.02$ . This restriction was applied in order to avoid tight selections with large variations in the efficiency as a function of the electron supercluster  $\eta$ . Further restrictions were imposed due to concerns that the calorimeter noise in simulation does not describe properly the noise in data. Random cone isolation studies with very early data suggested that a reasonable lower limit for ECAL and HCAL isolations would be 0.2 and for H/E: 0.025. These restrictions were applied in the tuning in addition of the  $\Delta\phi_{in}$  restriction.

The tuning was performed with different cuts on the electron supercluster  $E_T$ . The results are shown in Fig. 4.5(a). In this figure the “signal efficiency” is defined as the ratio of electrons that pass the selection criteria and the  $E_T$  cut over the electrons that pass the  $E_T > 20$  GeV cut. The measure of background rejection is the ratio of signal over background events defined in the same way, i.e. with respect to the  $E_T > 20$  GeV cut. As expected, very high “purity” (but low “efficiency”) samples can best be obtained by cutting harder in  $E_T$ , whereas the maximum electron “efficiency”

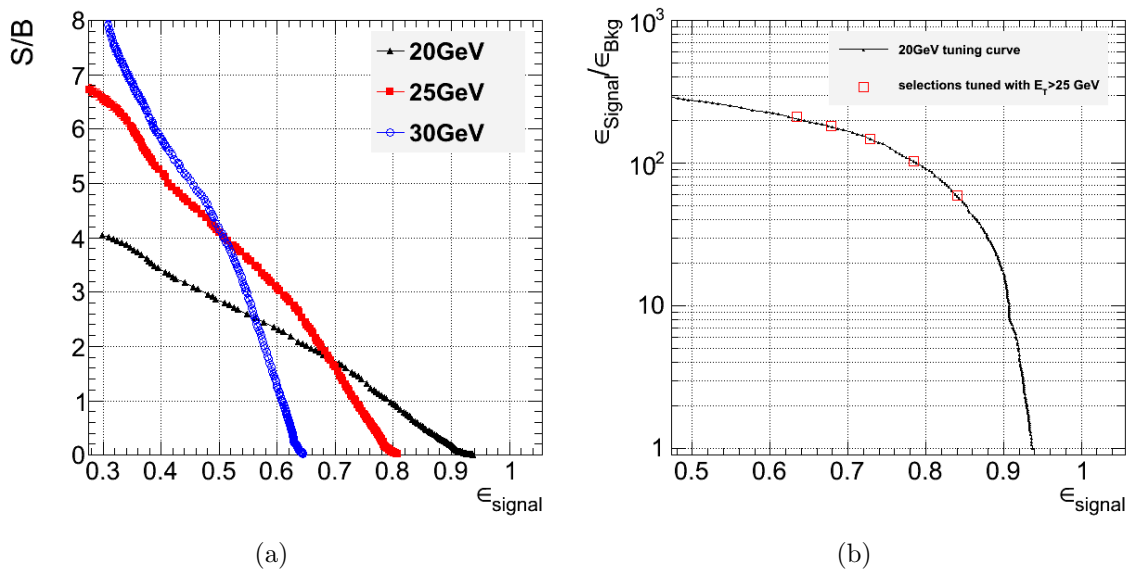


Figure 4.5: Application of the Iterative Technique on simulated electron samples with different cuts in electron supercluster  $E_T$ . (a) Comparison of tunings starting from different  $E_T$  cuts. (b) Application of selections tuned with 25 GeV cut on samples with a 20 GeV cut (markers connected with straight line segments) and comparison with selections tuned on samples with a 20 GeV cut. Both plots use the tight conversion rejection criteria.

(at the price of larger background contamination) can be best achieved with lower  $E_T$  thresholds.

Further studies have shown that if the selections that are tuned for electrons with  $E_T > 25$  GeV are applied to an electron set with  $E_T > 20$  GeV, then these selections have very similar performance as the selections that were tuned using the  $E_T > 20$  GeV cut. This effect is shown in Fig. 4.5(b). Motivated by these results, all the tunings presented here are performed with a 25 GeV cut, irrespective of the  $E_T$  cut that will be used on the data on which the selection cuts will be used.

The three curves corresponding to tunings starting from the different conversion rejection combinations are shown in Fig. 4.6. The signal efficiency and the background rejection are measured with electrons with supercluster  $E_T > 25$  GeV. As expected, for high signal efficiency, the loosest conversion rejection gives the best performance. From these curves, six test selections or working points (WPs) were chosen. The values

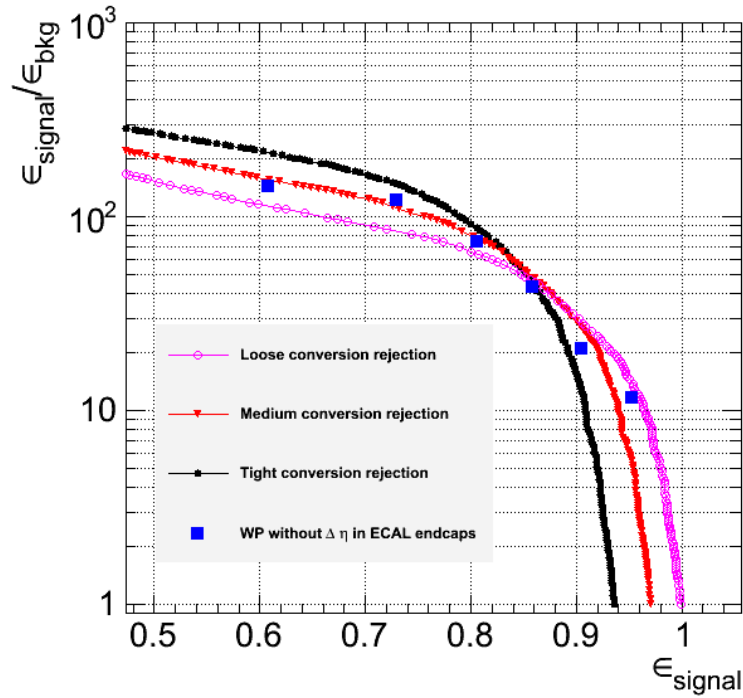


Figure 4.6: The performance of selection tuning with simulated samples for selections used on data. The markers indicate the selections of Table 4.1 without the  $\Delta\eta_{in}$  cut applied in the ECAL endcap region. Lines show the Iterative Technique tuning curves that are obtained including the  $\Delta\eta_{in}$  in the ECAL endcaps. The loosest working point (WP95) was chosen from the curve with loose conversion rejection, WP90 and WP85 from the medium conversion rejection curve and the rest from the tight conversion curve.

of the cuts at each of the working points are shown in Table 4.1. The working points are chosen to correspond to signal efficiencies of about 95%, 90%, 85%, 80%, 70% and 60% and will be referred to for convenience as WP95, WP90 and so on. The square filled markers in Fig. 4.6 correspond to these working points but without the  $\Delta\eta_{in}$  cut applied to electron candidates reconstructed in the ECAL endcaps. The reason for such a choice will be discussed in the next chapter, where these selections are tested with data.

## Summary

There is a trade-off between the electron efficiency and the background rejection that is achieved with an electron selection. The electron selection parameters need to be tuned

Table 4.1: Sets of cuts derived from simulated data using the Iterative Technique. See text for details.

<b>Selection</b>	WP95	WP90	WP85	WP80	WP70	WP60
<b>Conversion Rejection</b>						
missing hits $\leq$	1	1	1	0	0	0
Dist	N/A	0.02	0.02	0.02	0.02	0.02
$\Delta \cot \theta$	N/A	0.02	0.02	0.02	0.02	0.02
<b>ECAL BARREL</b>						
<b>Electron Isolation</b>						
Track isolation	0.15	0.12	0.09	0.09	0.05	0.04
ECAL isolation	N/A	0.09	0.08	0.07	0.06	0.04
HCAL isolation	0.12	0.10	0.10	0.10	0.03	0.03
<b>Electron Identification</b>						
$\sigma_{in\eta}$	0.01	0.01	0.01	0.01	0.01	0.01
$\Delta\phi_{in}$	N/A	N/A	0.06	0.06	0.03	0.025
$\Delta\eta_{in}$	0.007	0.007	0.006	0.004	0.004	0.004
$HoE$	0.15	0.12	0.04	0.04	0.025	0.025
<b>ECAL ENDCAPS</b>						
<b>Electron Isolation</b>						
Track isolation	0.08	0.05	0.05	0.04	0.025	0.025
ECAL isolation	0.06	0.06	0.05	0.05	0.025	0.02
HCAL isolation	0.05	0.03	0.025	0.025	0.02	0.02
<b>Electron Identification</b>						
$\sigma_{in\eta}$	0.03	0.03	0.03	0.03	0.03	0.03
$\Delta\phi_{in}$	N/A	N/A	0.04	0.03	0.02	0.02
$\Delta\eta_{in}$	0.01	0.009	0.007	0.007	0.005	0.005
$HoE$	0.07	0.05	0.025	0.025	0.025	0.025

such that the highest background rejection is achieved for a given signal efficiency. This can be done with a simple, easy-to-implement and fast iterative technique, which has been used to derive electron selections from simulation.

# Chapter 5

## Electron Commissioning with

## Collision Data

*May every young scientist remember and not fail to keep his eyes open  
for the possibility that an irritating failure of his apparatus to give  
consistent results may once or twice in a lifetime conceal an important  
discovery.*

Patrick Blackett

### 5.1 Data Samples

The LHC luminosity evolved rapidly in 2010, increasing from  $10^{28}$  to  $10^{30}$   $\text{cm}^{-2}\text{s}^{-1}$  between March and October. For this reason, the inclusive single electron dataset, which was used for these studies, has been defined by a number of different trigger paths, all of which have proven to be almost 100% efficient for high- $p_T$  ( $p_T > 20$  GeV/c), isolated electrons. All the triggers that have been used in this study were seeded on the Level-1 ECAL triggers with  $E_T > 5$  or 8 GeV threshold. For the early runs (see Table 5.1), the LHC instantaneous luminosity was low enough to allow un-

Table 5.1: HLT trigger paths together with their Level-1 (L1) trigger seed  $E_T$  thresholds for different run ranges used for the first  $2.88 \text{ pb}^{-1}$  of data taking. The integrated luminosity ( $\mathcal{L}$ ) for data corresponding to different run ranges are quoted separately. The total integrated luminosity is  $2.88 \text{ pb}^{-1}$ .

Run Range	HLT trigger path	L1 $E_T$ threshold	$\mathcal{L}$
132440-137028	HLT_Photon10_L1R	5 GeV	$13 \text{ nb}^{-1}$
138564-140401	HLT_Photon15_Cleaned_L1R	8 GeV	$0.27 \text{ pb}^{-1}$
141956-144114	HLT_Ele15_SW_CaloEleId_L1R	5 GeV	$2.60 \text{ pb}^{-1}$

prescaled<sup>1</sup> photon triggers with threshold below 20 GeV. During this low instantaneous luminosity period, events firing the HLT\_Photon10\_L1R trigger path initially and the HLT\_Photon15\_Cleaned\_L1R trigger path later were selected. The former (latter) requests the HLT supercluster to have  $E_T > 10 \text{ GeV}$  ( $E_T > 15 \text{ GeV}$ ). For later runs (see Table 5.1), a single electron HLT path was chosen: HLT\_Ele15\_SW\_CaloEleId\_L1R. This path requires an HLT supercluster with  $E_T > 15 \text{ GeV}$  that passes a loose  $\sigma_{i\eta i\eta}$  cut (0.014 in the ECAL Barrel and 0.035 in the ECAL endcaps) and is matched to a Kalman Filter track. The geometrical supercluster-pixel hit matching uses start-up windows (SW), which were set up especially for early data taking to allow for uncertainties about the detector alignment and beam spot variability and their sizes are shown in Table 3.1. This trigger choice was measured to be about 99% efficient for high- $p_T$  ( $p_T > 20 \text{ GeV}/c$ ), isolated electrons (see [72] and also Section 6.4).

From the events that are selected by these trigger paths, a further selection was made of events passing the criteria listed in Table 5.2. The ECAL fiducial region<sup>2</sup> is such that the electron supercluster  $\eta$  is  $|\eta| < 1.4442$  or  $1.566 < |\eta| < 2.5$ . The electron  $E_T$  here and in the rest of this study will be calculated as

$$E_T \equiv E_{SC} \sin \theta_{GSF}, \quad (5.1)$$

<sup>1</sup>Trigger prescaling is the action of discarding all but a fraction of the events selected by the trigger in question.

<sup>2</sup>For the definition of the ECAL fiducial  $\eta$  range the standard CMS notation is used in which the ECAL barrel-endcaps gap limits in  $\eta$  are quoted with 5 and 4 significant figures. This does not mean that the ECAL higher limit in  $\eta$  is not known with similar precision.

where  $E_{SC}$  is the corrected supercluster energy and  $\theta_{GSF}$  the polar angle of the electron GSF track to vertex.

Table 5.2: Summary of the requested criteria on the single electron event sample.

- Electron  $E_T > 20$  GeV in fiducial.
- Electron supercluster matched geometrically within  $\Delta R < 0.1$  to the electromagnetic HLT object.
- **Z veto:**  
there is no other reconstructed electron in the event with  $E_T > 20$  GeV passing loose electron identification criteria (WP95 - see Section 4.3).
- **Anomalous ECAL energy deposit veto :**  
the electron supercluster in the ECAL barrel is not seeded by a crystal for which:  
$$1 - s4/e1 > 0.95,$$
where  $e1$  is the seed crystal energy and  $s4$  is the sum of the energies of the 4 crystals that are adjacent to the seed crystal [101].

An important quantity that characterises the  $W \rightarrow e\nu$  process, is the event missing transverse energy ( $\cancel{E}_T$ ).  $\cancel{E}_T$  is reconstructed using the CMS particle flow algorithm, which uses information from all detectors and aims to reconstruct and identify all particles in an event optimally. In particular the momentum of low- $p_T$  charged hadrons is measured by the tracking system hence the reconstructed  $\cancel{E}_T$  is less sensitive to the relatively poor hadronic energy measurement of the calorimetry system. More details on the CMS particle flow algorithm can be found in Ref. [76].

## 5.2 Electrons and Electron Identification in Data

The reconstructed electrons in the samples of Table 5.1 that satisfy the requirements of Table 5.2 are mostly from jets. Figs. 5.1(a) and 5.1(b) show the  $\cancel{E}_T$  distribution of the events and the  $E_T$  distribution of the electron candidates respectively for the single electron sample. In the figure black points correspond to collision data and

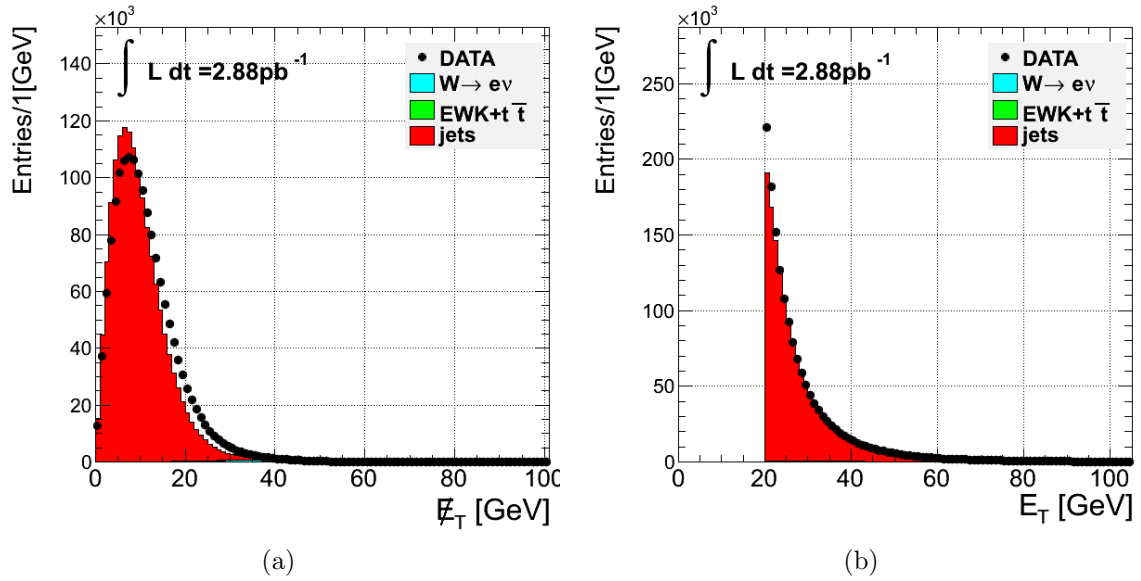


Figure 5.1: The distribution of the event transverse missing energy ( $E_T^{\text{miss}}$ ) in (a) and the electron candidate  $E_T$  in (b) for all events and electrons in the single electron sample fulfilling the criteria in Table 5.2. Black points correspond to collision data and histograms to simulated samples.

histograms to simulated sample distributions (see Section 3.4). The histograms are normalised to the data integrated luminosity. The same convention will be followed for all plots presented in this thesis that show data points and simulation histograms. The distributions show the expected  $E_T^{\text{miss}}$  spectrum for jet events, where  $E_T^{\text{miss}}$  is mainly due to the uncertainty in the jet energy measurement, and a steeply falling  $E_T$  spectrum, which characterises the hadronic processes.

It is possible to increase the fraction of prompt electrons in the data sample in a very simple way by vetoing events with reconstructed jets, since a typical hadronic event with a reconstructed electron contains a pair of jets. The event fails the veto if there is at least one jet with  $E_T > 15$  GeV. The jets are reconstructed with the anti- $k_T$  algorithm [78] with a cone size of  $\Delta R = 0.5$  and using the particle flow event description [76]. The vetoing jet is required to be separated from the electron candidate by  $\Delta R(\text{electron} - \text{jet}) > 0.3$ , to avoid double counting of the object as both an electron and a jet. The  $E_T^{\text{miss}}$  distribution of the events passing the jet veto is shown in Fig. 5.2(a), where a bump due to  $W$  production is visible in the high- $E_T^{\text{miss}}$  region. The electron  $E_T$

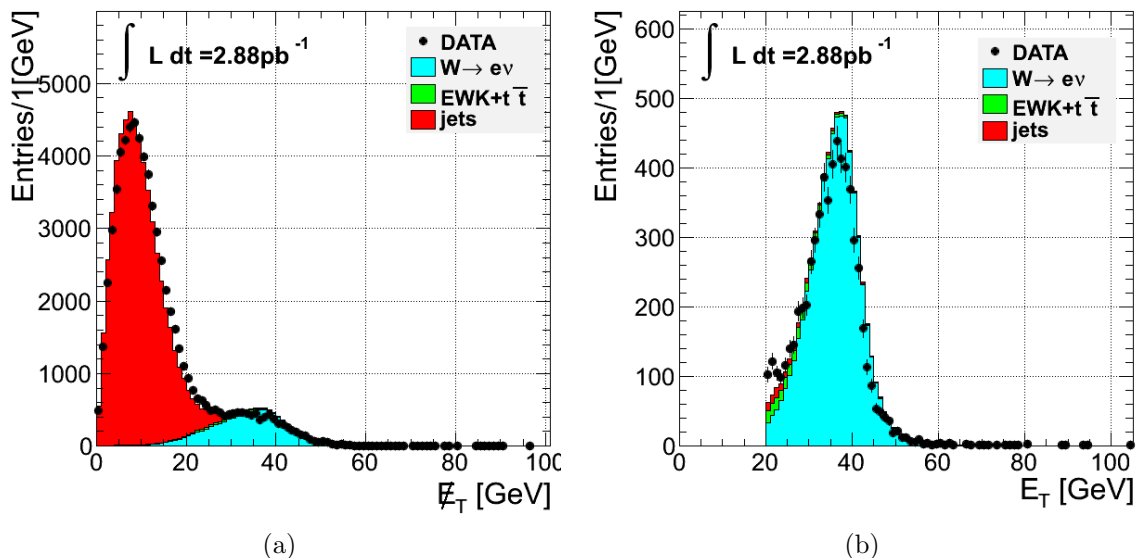


Figure 5.2: (a) The distribution of transverse missing energy ( $E_T$ ) for all events in the single electron sample that satisfy the criteria in Table 5.2 and pass a jet veto. (b) The electron candidate  $E_T$  distribution of the events shown in (a) that pass in addition a missing transverse energy cut:  $E_T > 30$  GeV. Black points correspond to collision data and histograms to simulated samples.

distribution for events with  $E_T > 30$  GeV, in addition to the jet veto, is shown in Fig. 5.2(b). The distinctive Jacobian peak in the  $E_T$  spectrum that is expected from  $W \rightarrow e\nu$  decays is observed. This result provides strong evidence that the high- $E_T$  pattern in Fig. 5.2(a) is due to W events.

The pure electron sample that is obtained using the jet veto and the  $E_T$  cut can be used to test the electron properties and identify problems. In general, the behaviour of the electron identification variables that were discussed in Section 3.3 agrees very well with the expectation from simulation. For example, the  $\Delta\phi_{in}$  distribution for reconstructed electrons in the ECAL barrel and ECAL endcaps is shown in Figs. 5.3(a) and 5.3(b) respectively.

An important feature that was revealed during electron commissioning was a misalignment between the ECAL endcaps and the tracker. This misalignment is visible in Fig. 5.4(a) where the  $\Delta\eta_{in}$  variable is examined for electrons reconstructed in one ECAL endcap. The figure shows a sinusoidal behaviour of  $\Delta\eta_{in}$  as a function of  $\phi$ , which is

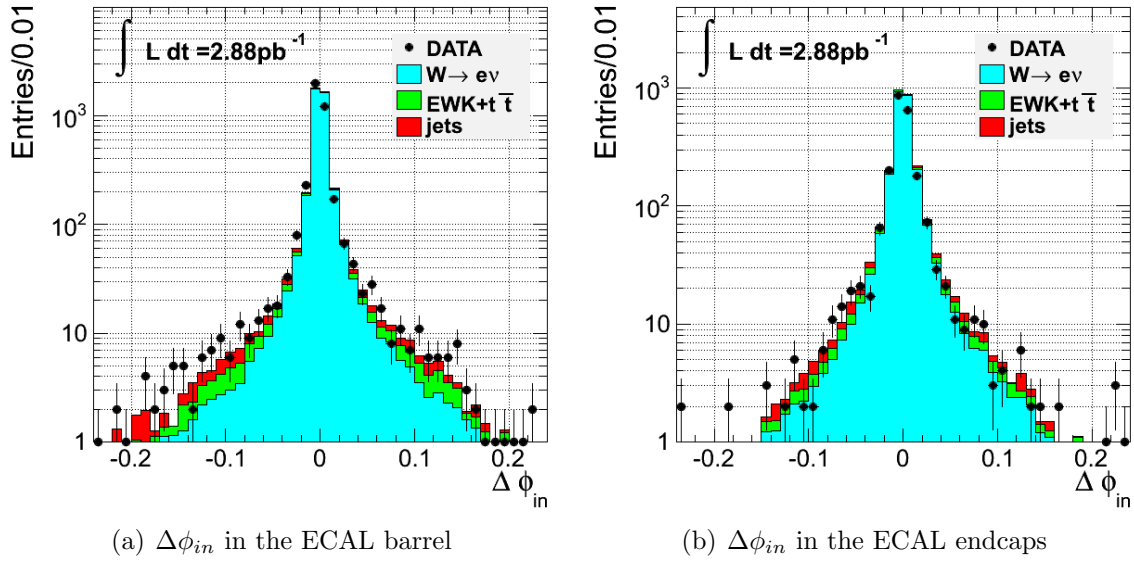


Figure 5.3: The  $\Delta\phi_{in}$  distribution for reconstructed electrons in the ECAL barrel (a) and ECAL endcaps (b) for events that pass a jet veto and a  $\cancel{E}_T$  cut. Black points correspond to collision data and histograms to simulated samples.

indicative of a linear displacement of the ECAL endcap with respect to the tracker. The effect of the misalignment on the  $\Delta\eta_{in}$  variable distribution is shown in Fig. 5.4(b). The figure shows that the distribution is much broader than expected. The corresponding plots for electrons reconstructed in the other ECAL endcap show similar features. An *ad hoc* correction has been applied to correct for this misalignment, however, it was believed that it was not perfect and for this reason the  $\Delta\eta_{in}$  cut was removed from the selection cuts applied to electrons in the ECAL endcaps.

Because of the excellent agreement between simulation and data in the electron identification variables it was not necessary to further tune the electron selection cuts used for early analyses. The cut values of Table 4.1 will be used with the  $\Delta\eta_{in}$  cut in the ECAL endcaps omitted. Figs. 5.5(a)-5.5(f) show the  $\cancel{E}_T$  distribution of the events remaining after successive application of tighter and tighter selections. As the selection becomes tighter the events in the low- $\cancel{E}_T$  region are reduced by a large factor, whereas few high- $\cancel{E}_T$  events are lost. This behaviour is exactly what is expected. The successive plots show the background rejection and signal efficiency expected if the data population is

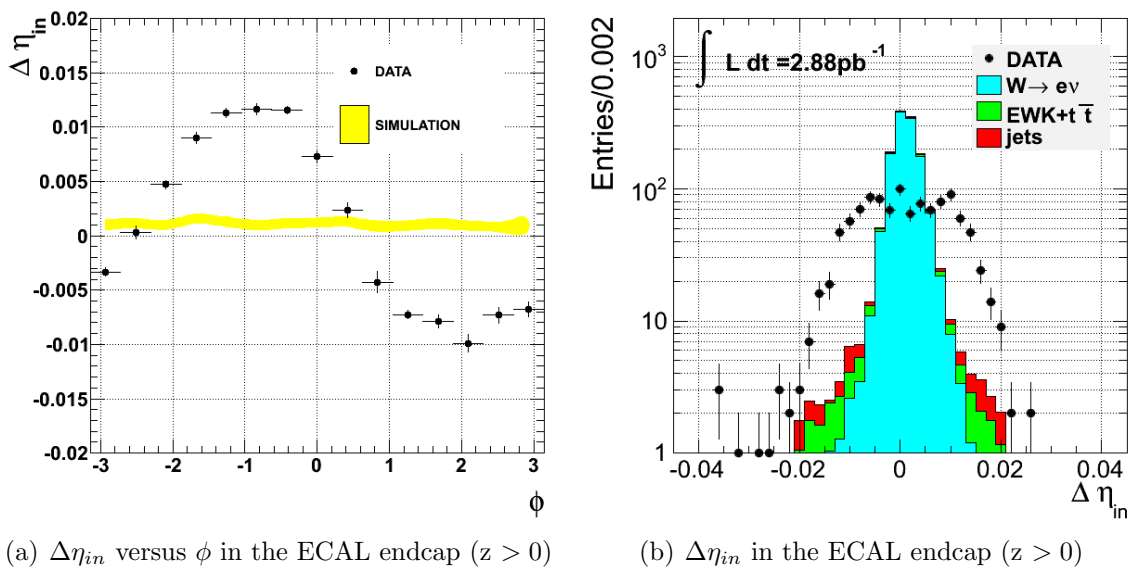


Figure 5.4: (a) The  $\Delta\eta_{in}$  mean value as a function of supercluster  $\phi$  for electrons reconstructed in the ECAL endcap ( $z > 0$ ). The vertical axis error bars correspond to the standard deviation of the  $\Delta\eta_{in}$  values in that  $\phi$  bin. The yellow band corresponds to the expectation from simulation. (b) The distribution of  $\Delta\eta_{in}$  for reconstructed electrons for the same sample. Black points correspond to collision data and histograms to simulated samples. The events in both plots pass a jet veto and a  $\cancel{E}_T$  cut.

as predicted by the simulation histograms. The observed discrepancy in the high- $\cancel{E}_T$  region signifies a worse  $\cancel{E}_T$  resolution in data, which is due to the poor performance of the simulation in describing the detector response to low- $p_T$  hadrons that are produced along with the W boson. This effect will be corrected for when a simulation-driven W template will be constructed for the cross-section measurement in Chapter 6.

The performance of the simulation in describing electrons can be tested in detail using the high- $\cancel{E}_T$  region for events with reconstructed electrons that pass some electron selection. In the following, the electron identification variables are studied for electrons passing WP80 cuts in events with  $\cancel{E}_T > 30$  GeV. The  $E_T$  and supercluster  $\eta$  distributions of the electron candidates are shown in Fig. 5.6. The distribution of the electron identification variables are plotted after the application of all other cuts in WP80 apart from the cut on the variable that is plotted. An example of such a distribution for the  $\Delta\phi_{in}$  variable is shown in Figs. 5.7(a) and 5.7(b) for electrons reconstructed in the ECAL barrel and ECAL endcaps respectively. Distributions for all the variables are

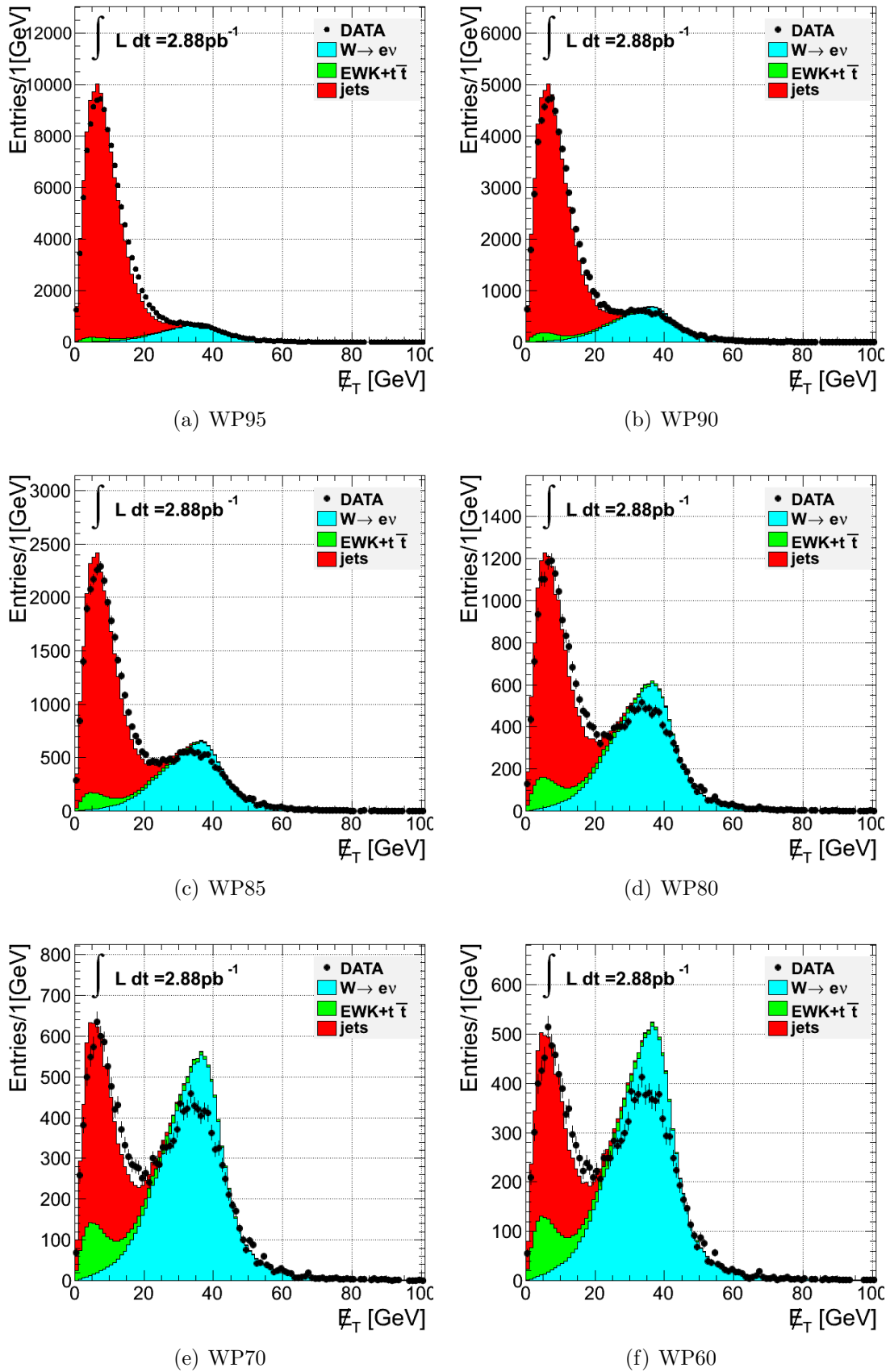


Figure 5.5:  $E_T$  distributions of the events in the single electron sample of Section 5.1 after the application of the electron selections of Table 4.1. Black points correspond to collision data and histograms to simulated samples.

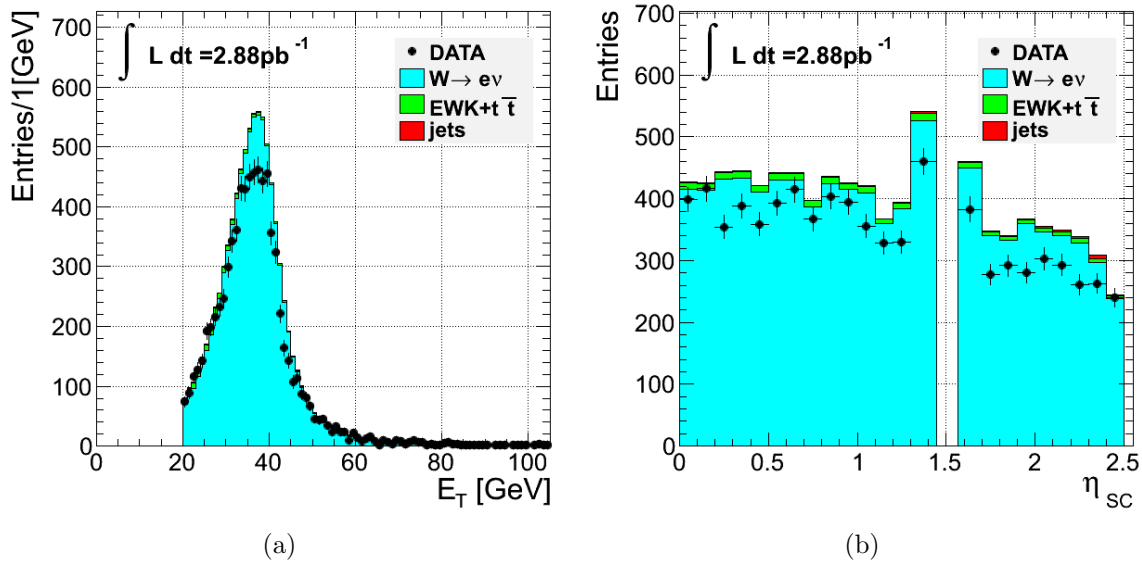


Figure 5.6:  $E_T$  and supercluster  $\eta$  distributions of electron candidates that pass WP80 and they are contained in events with high  $\cancel{E}_T$ . Black points correspond to collision data and histograms to simulated samples.

shown in Appendix A. The agreement between data and simulation in this study consolidates the previously reported evidence that the simulation describes prompt electrons very well.

The electron identification variables can also be examined in the single electron samples after WP80 selection cuts on the electron candidate but without any  $\cancel{E}_T$  restriction. An example of a distribution like this is shown for the ECAL isolation for electron candidates reconstructed in the ECAL barrel and ECAL endcaps in Figs. 5.8(a) and 5.8(b) respectively. Distributions for all the variables are shown in Appendix B. The good agreement between data and simulation shows that the electron backgrounds are also modelled successfully in simulation.

The first CMS  $Z \rightarrow ee$  and  $W \rightarrow e\nu$  cross-section measurements with  $200 \text{ nb}^{-1}$  [71] used the WP95 and WP80 selections respectively. For the cross-section measurements with  $3 \text{ pb}^{-1}$  [72] the WP80 selection was used for both  $Z \rightarrow ee$  and  $W \rightarrow e\nu$ .

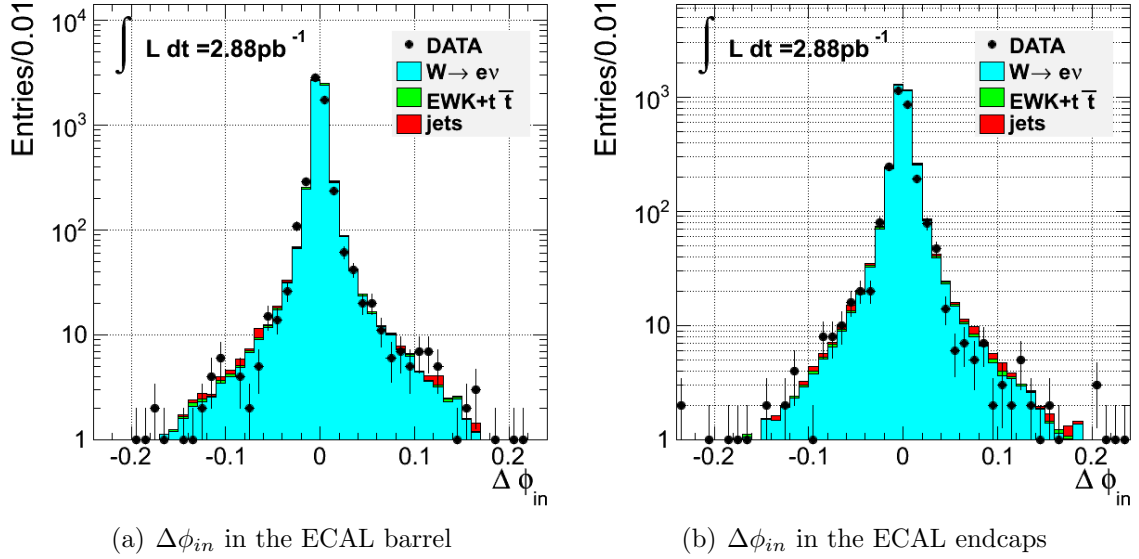


Figure 5.7:  $\Delta\phi_{in}$  distribution for electrons reconstructed in (a) the ECAL barrel and (b) the ECAL endcaps for electrons passing the WP80 cuts on all the variables apart from  $\Delta\phi_{in}$ . A further requirement of  $\cancel{E}_T > 30$  GeV is applied. Black points correspond to collision data and histograms to simulated samples.

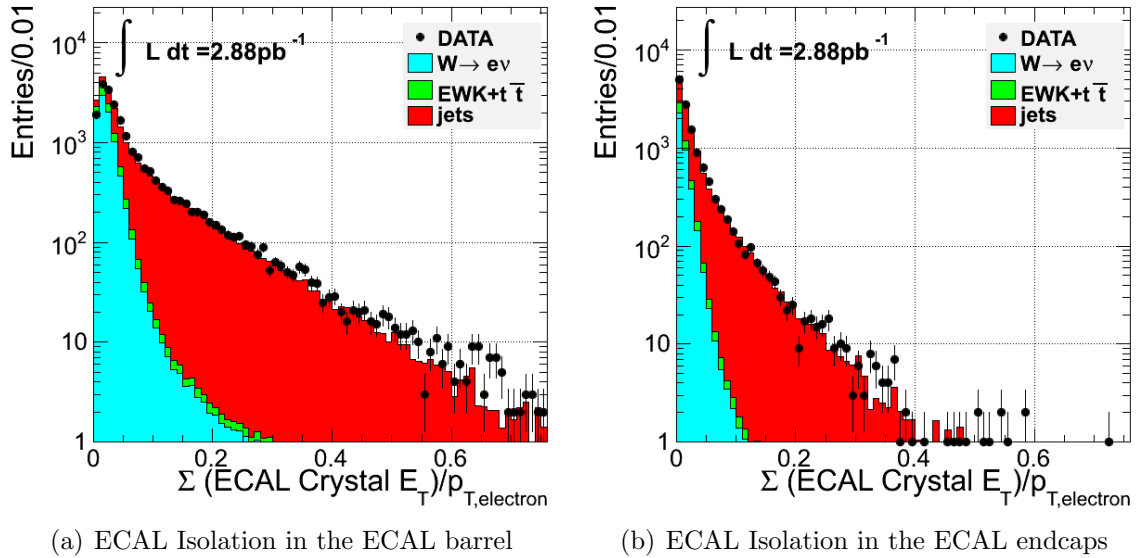


Figure 5.8: ECAL isolation distribution for electrons reconstructed in the ECAL barrel (a) and ECAL endcaps (b) for electrons passing the WP80 cuts apart on all the variables from the ECAL isolation. Black points correspond to collision data and histograms to simulated samples.

## 5.3 Future prospects with the Iterative Technique

Before the beginning of the CMS data-taking in 2010 data-driven methods to perform the selection tuning were studied. Data-driven signal and background electron samples can be derived in a number of ways:

- **A background electron sample** can be easily obtained by requesting an event with low  $\cancel{E}_T$ . From Fig. 5.5 one can see that if we demand electrons in events with  $\cancel{E}_T < 20$  GeV it is possible to obtain a background sample, which as shown later in this Section is pure enough for the needs of the selection tuning. In order to reduce  $Z \rightarrow ee$  events that also have low  $\cancel{E}_T$  we apply the further restriction that events with a second reconstructed electron are vetoed.
- **Signal electron sample** definitions that have been studied here include:
  - **$\cancel{E}_T$ -driven sample**: It is possible to derive a signal sample from  $W \rightarrow e\nu$  decays by requesting high- $\cancel{E}_T$  events, e.g.  $\cancel{E}_T > 30$  GeV.
  - **$\cancel{E}_T$ -driven sample with jet veto**: An improvement on the  $\cancel{E}_T$  selection is to further request that the event passes a jet veto (see Section 5.2). This definition has been used successfully to select samples enriched in prompt electrons for the commissioning of the electron identification variables, e.g. see Fig. 5.4.
  - **Z-driven sample**: A very pure electron sample can be obtained by using electrons from  $Z \rightarrow ee$  decays.

The performance of the Iterative Technique with the data-driven defined signal and background samples was tested on simulated samples. The selection tuning was performed with the data-driven definitions of signal and background samples using a “soup” of events from all the simulated samples. The selections, which were obtained in this way, were subsequently applied on a signal and a background electron sample with the

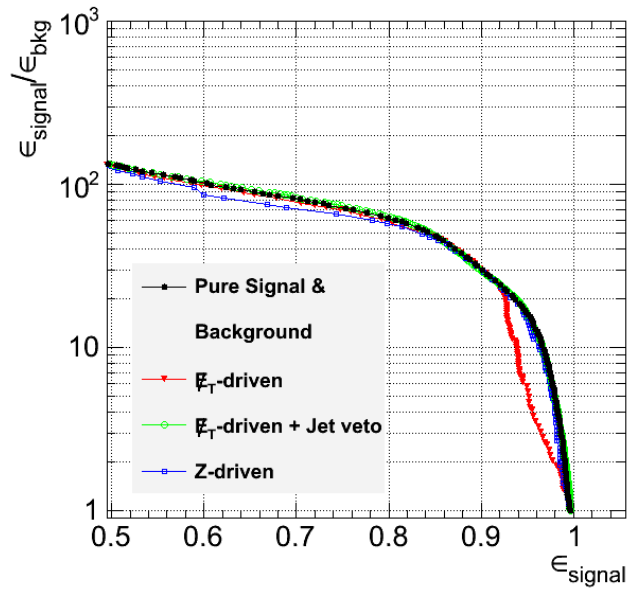


Figure 5.9: Test of the data driven set up for the Iterative Technique with simulated data. See text for details.

same definitions as used previously. The performance of the selections that are derived from the fake data samples is compared to the performance of the selections that were tuned using pure signal and background samples. A comparison is shown in Fig. 5.9, where the electron candidates were required to have  $E_T > 25$  GeV and pass the tight conversion rejection criteria that were defined in the previous section. In the figure, the performance of the  $E_T$ -driven signal sample is poor for high signal electron efficiencies. The reason is the large contamination of the signal sample by background when no further cuts are applied - see also Fig. 5.2. As the cuts become progressively tighter and tighter the  $E_T$ -driven signal sample becomes purer in signal electrons and finally the optimal curve is reached. The bad performance in the low background rejection region can be cured if the purer  $E_T$ -driven with jet veto or the Z-driven signal sample recipes are used.

The implementation and validation of the method with real data will demand a way to measure the selection efficiency and background rejection from data. The selection efficiency can be measured accurately from data using a pure electron sample from Z decays (see Section 6.4). There are also ways to measure the background rejection using

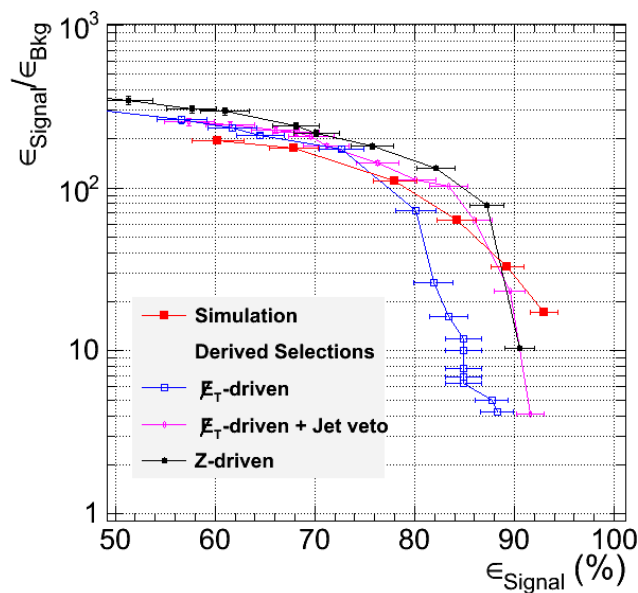


Figure 5.10: Test of the Iterative Technique with real data. Filled red rectangles correspond to the simulation defined selections of Table 4.1. Signal efficiency ( $\epsilon_{Signal}$ ) is measured from data using electrons from Z decays (see Section 6.4) and the background efficiency ( $\epsilon_{Bkg}$ ) is taken simply as the efficiency in the background sample obtained with the  $\cancel{E}_T < 20$  GeV cut. The integrated luminosity of the data sample used is  $850 \pm 94 \text{ nb}^{-1}$ . See text for details.

methods similar to the techniques that are used in the  $W \rightarrow e\nu$  signal extraction (see Section 6.6).

The Iterative Technique was tested on the first  $850 \pm 94 \text{ nb}^{-1}$  of data, using the data-driven signal and background input sample definitions discussed above, and using electron candidates with  $E_T > 25$  GeV passing the tight conversion rejection criteria. The signal efficiency of the selection cuts obtained was measured using electrons from  $Z \rightarrow ee$  decays. The background efficiency was measured from the efficiency of the  $\cancel{E}_T$ -driven background sample. The results of this test are shown in Fig. 5.10. All the errors quoted in the plot are statistical and due to the number of events in the samples that were used. Again the  $\cancel{E}_T$ -driven signal sample (open, blue rectangles) performs poorly in the low background rejection region as compared to the  $\cancel{E}_T$ -driven with the jet veto and the Z-driven signal samples.

## Summary

The simulation of electrons and their backgrounds reproduces the characteristics of data extremely well. The electron selections derived before the start of LHC data taking using simulated events have been used in 2010 with only one minor modification by most CMS physics analyses using electrons.

# Chapter 6

## $W \rightarrow e\nu$ Cross Section Measurement at CMS

*If a man begins with certainties, he will end in doubts;  
but if he is content to begin with doubts, he will end in certainties.*

Sir Francis Bacon

This chapter describes a measurement of  $\sigma(pp \rightarrow W + X) \times BR(W \rightarrow e\nu)$  with  $2.88 \pm 0.32 \text{ pb}^{-1}$  of LHC data recorded by CMS from spring till autumn 2010. The CMS measurement is published in Ref. [72].

### 6.1 Introduction

The measurement of the inclusive W cross section in the electron channel is summarised in the following formula:

$$\sigma(pp \rightarrow W + X) \times BR(W \rightarrow e\nu) = \frac{N_{sel} - N_{bkg}}{A_W \epsilon_W \int L dt}, \quad (6.1)$$

where the symbols have the following meaning:

- $N_{sel} - N_{bkg}$ : the number of events that pass the selection,  $N_{sel}$ , minus events from background processes,  $N_{bkg}$ .
- $\epsilon_W$ : the electron selection efficiency.
- $A_W$ : the acceptance of the kinematic cuts on  $W \rightarrow e\nu$  events.
- $\int Ldt$ : the integrated luminosity of the data samples in use.

In the following each of these items will be discussed in more detail.

## 6.2 Samples and Event Selection

The data samples that are used in this analysis are selected from runs during which the CMS detector was operating without any anomalous or faulty behaviour for the inner tracker, the calorimeters and the muon chambers. The events pass single photon or single electron triggers that are very efficient for high- $E_T$ , isolated electrons and are listed in Table 5.1. The events are required to contain a reconstructed electron which satisfies the following criteria:

- $E_T > 20$  GeV and its ECAL supercluster is in the ECAL fiducial region ( $|\eta| < 1.4442$  or  $1.566 < |\eta| < 2.5$ ).
- is geometrically matched ( $\Delta R < 0.1$ ) to the object that fired the HLT.
- passes the anomalous ECAL deposit veto defined in Table 5.2.
- passes the WP80 selection cuts (see Table 4.1).

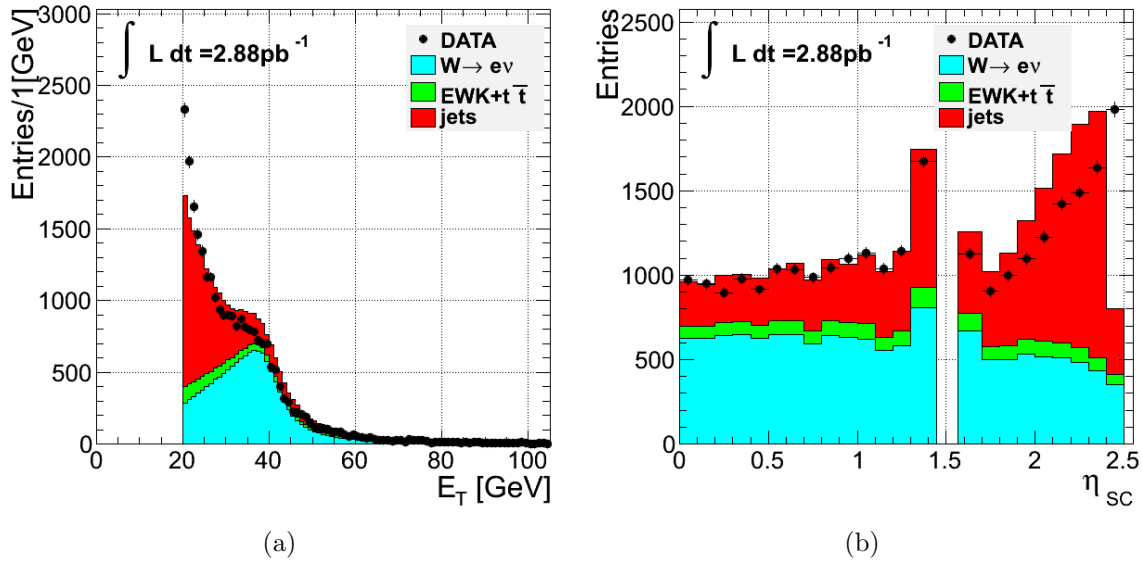


Figure 6.1: (a) The electron transverse energy,  $E_T$ , and (b) the supercluster pseudo-rapidity,  $\eta_{sc}$ , distributions of the  $W \rightarrow e\nu$  selected candidate events.

Finally a Z veto is applied: the event is rejected if it contains a second electron with  $E_T > 20$  GeV that passes the WP95 selection cuts (see Table 4.1).

The number of  $W \rightarrow e\nu$  candidate events that are selected in the data sample that is used in this analysis is 28 601. The  $E_T$  and  $\eta$  distributions of the electron candidate in these events are shown in Fig. 6.1 together with the distributions of simulated signal and background events.

## 6.3 Acceptance

The signal acceptance,  $A_W$ , is calculated from simulation. It is defined as the fraction of  $W \rightarrow e\nu$  events with an ECAL supercluster with  $E_T > 20$  GeV in the ECAL fiducial region ( $|\eta| < 1.4442$  or  $1.566 < |\eta| < 2.5$ ) matched to a generator level electron within  $\Delta R < 0.2$ . The ECAL supercluster  $E_T$  is defined by taking the direction from the event primary vertex in order to maintain consistency in the efficiency definition (see Section 6.4). This definition includes in the acceptance the superclustering efficiency

and the effect of the supercluster energy measurement on the  $E_T$  cut.

The base-line Monte Carlo that is used for the inclusive  $W \rightarrow e\nu$  cross-section measurement is POWHEG [79, 80], which is a next-to-leading-order (NLO) generator. POWHEG is used in conjunction with the CTEQ6.6 parton distribution function (PDF) sets [81].

The uncertainty sources from theory that have been considered for the acceptance calculation are the following:

- uncertainty on the PDFs.
- uncertainty from limitations in the calculation of the parton level cross sections. These can be for example due to the order of the calculation or on the processes that the generator includes and the dependence on the factorization and renormalization scales.

PDF sets include, apart from the best fit, uncertainty sets that can be used to evaluate systematics. The study presented here has considered the 68% CL positive and negative uncertainties obtained with CTEQ6.6, MSTW2008NLO [82] and NNPDF2.0 [83] sets. The final assignment of systematics corresponds to half of the maximum difference observed between positive and negative variations for any combination of the three sets. The whole procedure is consistent with the latest PDF4LHC recommendations [84]. Uncertainties due to the QCD coupling  $\alpha_S$  are also considered, even if they are much below 1%. In summary, the uncertainty due to the PDF set as a fraction of the W acceptance is about 0.8%.

Higher order soft and hard QCD effects and initial state radiation (ISR) effects, which are not included in the base-line Monte Carlo generator, are studied by comparing it to the ResBos generator [85–90] at NNLO. The effect of the QCD factorization scale dependence on NNLO calculations is estimated by comparing the POWHEG result with

Table 6.1: Summary of the theoretical uncertainties in the acceptance calculation.

Source	$W^+ \rightarrow e^+\nu$ (%)	$W^- \rightarrow e^-\bar{\nu}$ (%)
QCD higher order effects and ISR	1.30	0.78
QCD factorisation scale	0.23	0.37
final state radiation	0.08	0.07
other EWK effects	0.07	0.21
Total	1.3	0.9

results from FEWZ [91, 92]. Finally, higher order electroweak effects and final state radiation (FSR) are estimated with HORACE [93–96]. All these effects are calculated separately for  $W^+$  and  $W^-$ . The results are shown in Table 6.1 that lists the relative shift in the acceptance due to the different effects. The difference between the  $W^+$  and  $W^-$  is related to the production mechanism and the associated uncertainties. For more details on the uncertainty estimation see Ref. [97] and Refs. therein. The total uncertainty is a sum in quadrature of all the shifts. For the inclusive  $W \rightarrow e\nu$  acceptance the highest of these uncertainties is used, i.e. the uncertainty quoted for  $W^+$ .

Other uncertainties in the acceptance calculation include the uncertainty in the superclustering efficiency and the supercluster energy scale and resolution. The small deviation from 1 of the superclustering efficiency is mostly due to masked ECAL towers, which is taken into account in the detector simulation and hence no uncertainty is assigned for this effect. The uncertainty due to the supercluster energy resolution was studied by smearing the supercluster energy in simulation such that there is agreement with the width of the  $Z$  peak seen in data. The smearing results in a variation of the acceptance of 0.07%. The error on the acceptance due to imperfect modelling in simulation of the electron energy scale has been studied using the signal extraction and is described in Section 6.6.

The result for the signal acceptance is shown in Table 6.2.

Table 6.2: The calculated values for the  $W \rightarrow e\nu$  signal acceptance ( $A_W$ ) from the simulation. The statistical uncertainties on these numbers are negligible ( $< 0.2\%$ ).

	ECAL barrel	ECAL endcaps	ECAL barrel+endcaps
$A_W$	0.358	0.212	0.571

## 6.4 Efficiency Determination

The efficiency is defined with respect to the acceptance. It can be broken down as follows:

$$\epsilon_W = \epsilon_{reco} \times \epsilon_{selection} \times \epsilon_{trigger}, \quad (6.2)$$

where the components are:

- $\epsilon_{reco}$ , electron reconstruction efficiency: the fraction of ECAL superclusters with  $E_T > 20$  GeV that become reconstructed electrons with  $E_T > 20$  GeV.
- $\epsilon_{selection}$ , electron selection efficiency: the fraction of reconstructed electrons with  $E_T > 20$  GeV that pass the WP80 selection requirements.
- $\epsilon_{trigger}$ , trigger efficiency: the fraction of the reconstructed electrons with super-cluster  $E_T > 20$  GeV and satisfying the WP80 criteria that have passed the trigger.

The order of these factors is such that each of them can be determined with respect to the prior step.

### 6.4.1 The Tag-and-Probe Method

The efficiency is measured using a tag-and-probe method. It is possible to select a pure electron sample from data by taking advantage of the easy-to-identify  $Z \rightarrow ee$  decays. A well-identified electron tags the event. Another electron candidate that makes an invariant mass with the tag close to the mass of the  $Z$  boson is very likely to be an electron and hence can be used as a probe to measure efficiency.

The probe electrons have kinematic distributions that are similar to the electrons from  $W \rightarrow e\nu$  decays. However, there are differences in the  $W$  and  $Z$  kinematics that result in biased efficiency measurements. To study this effect the tag-and-probe method is tested on simulated  $Z \rightarrow ee$  events. The tag is defined as a reconstructed electron with  $E_T > 20$  GeV passing the WP70 selection cuts of Table 4.1 and the probe is a reconstructed electron with  $E_T > 20$  GeV. In order to avoid potential biases due to an invariant mass requirement, no such requirement was demanded here. On the collection of probe electrons selected in this way the various selections of Section 4.3 are applied and the efficiency is compared to the efficiency that is calculated directly from simulated  $W \rightarrow e\nu$  events using the same kinematic requirements. The result of this exercise is shown in Fig. 6.2, where the black dots connected with straight line segments show the difference of the  $W$  sample efficiency minus the efficiency as measured by the tag-and-probe method as a function of the  $W$  sample efficiency. The plot shows that the tag-and-probe method overestimates the efficiency by an amount that is roughly proportional to the tightness of the selection. It has been verified that this effect is insensitive to the tag selection. The remaining lines in the plot show what happens if the probe electron collection is rescaled in bins of  $\eta$  and  $E_T$  before the application of any selection such that the shapes of the distributions agree with those obtained from the  $W$  electron collection. After applying the selection cuts on the rescaled probe electrons the difference with respect to the  $W$  efficiency is significantly reduced suggesting that the difference was in a large part due to the efficiency variation with electron  $\eta$  and

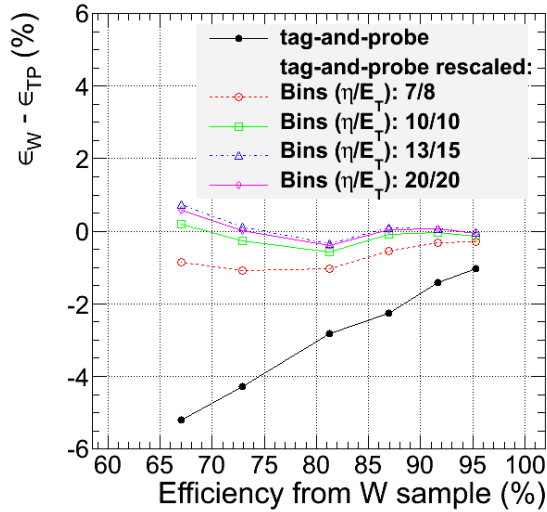


Figure 6.2: The difference between the efficiency of selections calculated directly from  $W \rightarrow e\nu$  simulated events ( $\epsilon_W$ ) and the tag-and-probe method ( $\epsilon_{TP}$ ) on simulated  $Z \rightarrow ee$  events. Black points connected with straight line segments refer to the pure tag-and-probe result. The remaining lines show the tag-and-probe result after a rescaling of the kinematic distributions of the probe electrons in bins of  $\eta$ - $E_T$  such that they agree with the ones of the  $W$  electrons. The binning in  $\eta$ - $E_T$  becomes finer and finer with 7, 10, 13 and 20  $\eta$  bins and 8, 10, 15 and 20  $E_T$  bins respectively.

electron  $E_T$ . The remaining bias can be attributed to kinematic differences in other than the  $\eta$  and  $E_T$  distributions, like hadronic recoil related effects, and effects due to the tag selection, which has been shown to bias the efficiency measurement at a level similar to the remaining bias that is shown in Fig. 6.2.

The efficiencies that are used to calculate the  $W$  cross section are calculated in a slightly more sophisticated way which accounts for the non-negligible background which is present when the probe is a supercluster. The number of passing and failing probe electrons is determined with an unbinned extended likelihood fit of the tag-probe invariant mass distribution using separate templates for signal and background. The background template consists of an exponential distribution. The signal template is the convolution of the  $Z$  invariant mass distribution taken from simulation, and a Gaussian to account for the worse energy resolution in data. The tag-probe invariant mass is restricted to the range 60-120  $\text{GeV}/c^2$  and the tag electron definition is an electron that passes WP80 selection cuts.

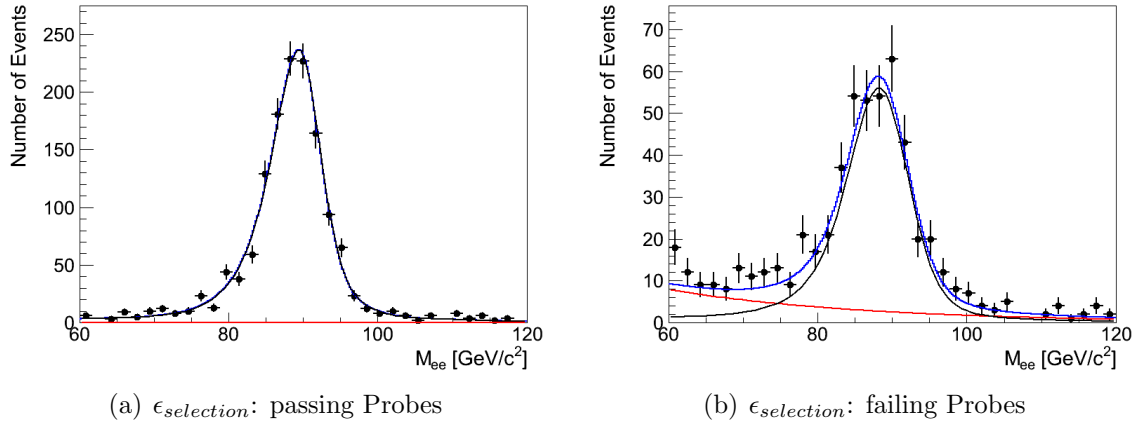


Figure 6.3: Example of fits to the tag-probe invariant mass distribution for the efficiency calculation. The probes are reconstructed electrons. On the left (right) the distribution of the probe electrons that pass (fail) the WP80 selection cuts is shown. In the plots data are shown with black points, the signal template with a black line, the background template with a red line and the combined result of the fit with a blue line.

### 6.4.2 Efficiency for the $W \rightarrow e\nu$ Electron Selection

To avoid the bias due to the differing kinematic distributions of electrons from  $W$ 's and  $Z$ 's, each of the efficiency terms in Eq. (6.2) is calculated with the following formula:

$$\epsilon_W = \epsilon_{WMC} \times \frac{\epsilon_{TP,data}}{\epsilon_{TP,MC}} \equiv \epsilon_{MC} \times \rho_{eff}, \quad (6.3)$$

where  $\epsilon_{WMC}$  is the efficiency calculated for simulated  $W \rightarrow e\nu$  samples and  $\epsilon_{TP,data}$  ( $\epsilon_{TP,MC}$ ) is the tag-and-probe efficiency of data (simulated  $Z \rightarrow ee$  events). The ratio  $\rho_{eff} \equiv \epsilon_{TP,data} / \epsilon_{TP,MC}$  will be referred to as the efficiency correction factor. An example of the fits to the tag-probe invariant mass distributions in data for the calculation of  $\epsilon_{selection}$  is shown in Fig. 6.3.

The efficiencies are calculated separately for electrons with their supercluster in the ECAL barrel and ECAL endcaps. The results are subsequently combined by weighting the barrel-only and endcaps-only efficiencies with the ECAL barrel and ECAL endcaps signal acceptance that is quoted in Table 6.2. The tag-and-probe efficiency values from both data and simulation along with the efficiency correction factors are shown in

Table 6.3.

Table 6.3: Results from the efficiency calculation with the tag-and-probe method. Quoted uncertainties are of statistical nature only apart from the last row. The combined ECAL efficiency (barrel+endcaps) is calculated by re-weighting the efficiencies with the acceptance values quoted in Table 6.2.

Efficiency	Data (%)	Simulation (%)	$\rho_{eff}$
<b>ECAL barrel (stat. uncertainty only)</b>			
$\epsilon_{reco}$	$98.6 \pm 0.5$	$98.50 \pm 0.02$	$1.001 \pm 0.005$
$\epsilon_{selection}$	$79.1 \pm 1.8$	$85.50 \pm 0.05$	$0.925 \pm 0.021$
$\epsilon_{trigger}$	$98.9 \pm 0.3$	$99.70 \pm 0.01$	$0.992 \pm 0.003$
Total	$77.1 \pm 1.8$	$83.90 \pm 0.05$	$0.919 \pm 0.022$
<b>ECAL endcaps (stat. uncertainty only)</b>			
$\epsilon_{reco}$	$96.2 \pm 0.8$	$96.30 \pm 0.04$	$0.999 \pm 0.009$
$\epsilon_{selection}$	$69.2 \pm 2.0$	$74.90 \pm 0.10$	$0.924 \pm 0.027$
$\epsilon_{trigger}$	$99.2 \pm 0.5$	$98.80 \pm 0.03$	$1.003 \pm 0.005$
Total	$66.0 \pm 2.0$	$71.30 \pm 0.10$	$0.926 \pm 0.028$
<b>ECAL barrel and endcaps (stat. uncertainty only)</b>			
Total	$73.0 \pm 2.5$	$79.20 \pm 0.05$	$0.921 \pm 0.032$
<b>ECAL barrel and endcaps (total uncertainty)</b>			
Total	$73.0 \pm 2.9$	$79.20 \pm 0.05$	$0.921 \pm 0.036$

The quoted tag-and-probe efficiency results have been cross-checked in a number of ways and the different methods all give results that are consistent with the values quoted in Table 6.3:

- Alternative signal and background templates have been tried. For the background template a polynomial function was used and for the signal template the choice was a Breit-Wigner distribution with nominal Z mass and width convolved with a “Crystal Ball” asymmetric resolution function with floating parameters (see Appendix E of Ref. [98]).
- Electron isolation efficiency can be estimated independently using a random cone technique. This method is based on the fact that electrons from  $W \rightarrow e\nu$  decays are isolated. Random cones are aimed at measuring the activity around a W

Table 6.4: Efficiency of the  $W$  selection criteria calculated directly from  $W \rightarrow e\nu$  simulated events for the ECAL barrel, endcaps and combined. Statistical uncertainties on these numbers are negligible.

ECAL barrel (%)	ECAL endcaps (%)	ECAL barrel+endcaps (%)
83.1	70.1	78.2

electron, which is mainly due to underlying event, pile-up and zero-suppressed electronics noise.

- The trigger efficiency is confirmed by measurements made with samples of minimum-bias events selected with scintillator counters and of events selected by an HLT algorithm which has minimum-bias requirements at the Level-1 trigger and a complete emulation of the offline ECAL cluster reconstruction.

In the efficiency measurements shown in Table 6.3 the most important source of uncertainty is due to the imperfect modelling of the tag-probe invariant mass distribution in the case where the probe fails the selection. This uncertainty is estimated by using templates for the tag-failing probe invariant mass distribution constructed by demanding cuts on the tag that are tighter than the nominal tag criteria. The efficiency variation with respect to the nominal result is about 1.6%. The uncertainty due to imperfections in the background parameterisation is estimated by assuming a polynomial background distribution which is fitted to the templates that are used to measure the efficiency on data. This uncertainty is found to be about 0.3%. Uncertainties in the efficiency related to the electron energy scale are estimated by shifting the electron energies in simulation by the energy scale uncertainty, and found to be about 0.2%. The systematic uncertainties of the efficiency measurement are added in quadrature to the statistical uncertainty to form the total uncertainty that is shown in the last row of Table 6.3.

The selection efficiency as calculated directly from  $W \rightarrow e\nu$  simulated events is shown in Table 6.4.

## 6.5 Luminosity

The instantaneous luminosity ( $\mathcal{L}_{inst}$ ) can be calculated from:

$$\mathcal{L}_{inst} = C\mu f_{BX}, \quad (6.4)$$

where  $f_{BX}$  the bunch crossing frequency,  $\mu$  is the mean number of interactions per bunch crossing and  $C$  a proportionality constant.

The mean number of interactions per bunch crossing,  $\mu$ , is measured by examining the occupancy of the individual towers of the hadronic forward (HF) calorimeter (see also Section 2.2.4). It is assumed that the number of empty towers in a single interaction event follows a binomial distribution with probability  $p$ . If there are  $n$  interactions in the event, then the binomial distribution parameter will be simply  $p^n$ . Given that  $n$  follows a Poisson distribution with mean  $\mu$  then the average fraction of empty towers,  $\langle f_0 \rangle$  is:

$$\langle f_0 \rangle = \sum_k \frac{e^{-\mu} \mu^k}{k!} p^k = e^{\mu(p-1)}, \quad (6.5)$$

where the sum is over all the possible number of interactions per bunch crossing. It can be deduced from Eq. (6.5) that the logarithm of the average number of empty towers is proportional to the mean number of interactions per bunch crossing and hence proportional to the luminosity.

The constant  $C$  is determined by measuring the size and shape of the interacting beams with van der Meer scans and calculating the luminosity using the measured beam current [99]. The absolute luminosity of the CMS data samples is estimated with this method with a total uncertainty of 11%. The dominant source of uncertainty is due to the beam current measurement. More details for the CMS luminosity measurement can be found in Ref. [100].

The integrated luminosity of the data set used in this analysis is measured to be

$2.88 \pm 0.32 \text{ pb}^{-1}$ .

## 6.6 Signal Extraction

The selection of  $W \rightarrow e\nu$  decay candidates described in Section 6.2 is based on selecting events with a high- $p_T$ , well-identified electron. Despite the stringent selection criteria, the W candidate collection contains background events and a procedure has to be defined to subtract this residual background and extract the number of the  $W \rightarrow e\nu$  events. One such method is an unbinned maximum likelihood fit to the missing transverse energy ( $\cancel{E}_T$ ) distribution using separate templates for the signal and jet background events after subtracting the small electroweak background contribution using an estimate directly from simulation.

The modelling of the background contribution from hadronic jets is the most difficult, since the electron selection makes these events unrepresentative of a typical jet. The shape of the  $\cancel{E}_T$  distribution of these events can be parameterised with a modified Rayleigh function:

$$P_{jet}(x; \sigma_0, \sigma_1) = x \exp\left(-\frac{x^2}{2(\sigma_0 + \sigma_1 x)^2}\right), \quad (6.6)$$

with two floating parameters,  $\sigma_0$  and  $\sigma_1$ . Alternatively a jet background template can be defined by using an inverted electron selection on data. This template can be used to cross-check the modified Rayleigh template (see Fig. 6.4) and the cross-section result (see later in this Section).

The signal simulation does not provide a signal template accurate enough for the precise extraction of the signal (see Fig. 5.5(d)). The differences in the  $\cancel{E}_T$  resolution between data and simulation can be corrected by parameterising in terms of the boson recoil. This parametrisation is used because it separates the effects due to imperfectly modelled overall hadronic response, and the effects due to imperfectly modelled electron

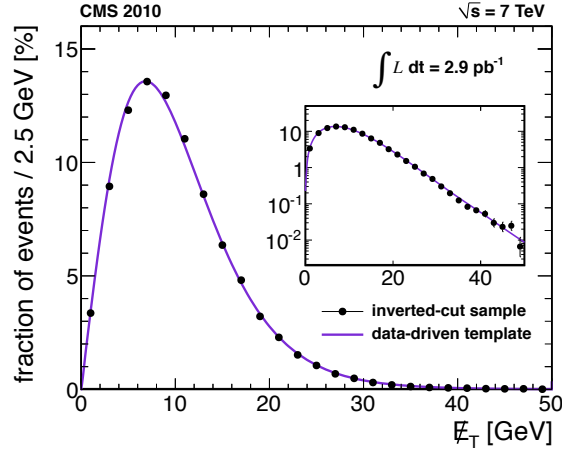


Figure 6.4: The  $\cancel{E}_T$  template based on a modified Rayleigh function of Eq. 6.6 fitted to a distribution derived from data by inverting track-ECAL cluster matching electron identification cuts.

measurement (predominantly the energy scale).

The description of the recoil response in simulation can be improved with the help of a clean sample of  $Z \rightarrow ee$  events from data. In a  $Z \rightarrow ee$  event the transverse recoil vector,  $\vec{u}_T$ , is defined by  $\vec{u}_T \equiv -(\vec{q}_T + \vec{\cancel{E}}_T)$ , where  $\vec{q}_T$  is the boson transverse momentum. The recoil  $\vec{u}_T$  is decomposed to a component that is parallel to  $\vec{q}_T$ ,  $u_1$ , and a component that is perpendicular to  $\vec{q}_T$ ,  $u_2$ . The distributions of  $u_1$  and  $u_2$  are fitted with a Gaussian for  $Z \rightarrow ee$  events in data and in simulation in different bins in  $q_T$ . The means (variances) of the Gaussians are fitted to a first (second) order polynomial that is a function of  $q_T$  in order to get the response (resolution) function. The same procedure is done for simulated  $W \rightarrow e\nu$  events. The correction is applied by multiplying the coefficients of the response and resolution polynomials that were calculated for the  $W \rightarrow e\nu$  sample by the ratio of the same coefficients in  $Z \rightarrow ee$  data over simulation. Then for a given simulated  $W \rightarrow e\nu$  event the transverse recoil is recalculated by sampling a Gaussian with mean and variance that are calculated with the data-corrected  $W \rightarrow e\nu$  response and resolution functions. Finally, the event  $\cancel{E}_T$  in the simulation can be corrected to be  $\vec{\cancel{E}}_T = -(\vec{q}_T - \vec{E}_e + \vec{u}'_T)$ , where  $\vec{E}_e$  is the electron energy as a vector and  $\vec{u}'_T$  is the recalculated value of the transverse recoil vector.

An alternative method of deriving a signal template using the information contained in the  $Z \rightarrow ee$  events, is to take the  $Z \rightarrow ee$  events and subtract or remove one of the electrons to directly emulate the neutrino in the  $W \rightarrow e\nu$  decay. It is possible that with increased Z events available for large integrated luminosity this method may prove to have a smaller systematic uncertainty.

The  $\cancel{E}_T$  distributions due to the various electroweak backgrounds are taken directly from simulation and they are added to the  $W \rightarrow e\nu$   $\cancel{E}_T$  distribution to create a template,  $P_{ewk+W}$ , which is finally used in the fit. The electroweak processes that are included in the template are  $Z \rightarrow ee$ , diboson production (WW, WZ, ZZ),  $W \rightarrow \tau\nu$  and  $Z \rightarrow \tau\tau^1$  and  $t\bar{t}$ .

In summary, the fit template is:

$$P(x; N_{jet}, N_W, \sigma_0, \sigma_1) = N_{jet} P_{jet}(x; \sigma_0, \sigma_1) + N_W P_{ewk+W}(1 - f_{ewk}), \quad (6.7)$$

where  $f_{ewk}$  is the fraction of the electroweak backgrounds in  $P_{ewk+W}$ , which is fixed from the simulation. The fit has four floating parameters: the jet background yield,  $N_{jet}$ , the W signal yield,  $N_W$ , and the background shape parameters,  $\sigma_0$  and  $\sigma_1$ .

The following systematic uncertainties in the signal extraction have been identified and studied:

- electron energy scale and resolution. The energy scale corrections obtained from the shift in the Z mass peak are applied to the reconstructed electrons before the  $E_T$  cut is applied and the  $\cancel{E}_T$  is recomputed. The variation of the signal yield from the fit is 2.0% and this difference is quoted as the systematic uncertainty due to the uncertainty in the electron energy scale. This procedure allows for both the energy scale effect on the signal extraction and the acceptance with the

---

<sup>1</sup>Events containing  $\tau$  decays for the signal extraction were generated with PYTHIA6 [73] interfaced to TAUOLA [103] for an accurate description of  $\tau$  decays.

dominant contribution to the uncertainty being due to the effect on the signal extraction. The effect on the energy resolution of the signal template is estimated by recomputing the signal template after smearing the electron energy in the W and Z simulated samples such that the width of the Z peak is the same as in data. The induced signal yield variation is 0.1% and this difference is taken as the systematic uncertainty due to the energy resolution.

- modelling of the signal  $\cancel{E}_T$  distribution. This uncertainty is estimated by examining how good are the the response and resolution function fits that are calculated to define the  $\cancel{E}_T$  correction that is applied to the simulation. Based on these fits, upper and lower bounds for the  $\cancel{E}_T$  correction can be calculated. The difference in the signal yield using the signal templates obtained using these two extreme bounds for the  $\cancel{E}_T$  correction is about 1.8%. This difference is considered as the systematic uncertainty due to the  $\cancel{E}_T$  scale and resolution.
- modelling of the jet background: the parameterization used to extract the signal in Eq. (6.6) is modified, giving it an additional degree of freedom:

$$P_{jet}(x; \sigma_0, \sigma_1) = x \exp\left(-\frac{x^2}{2(\sigma_0 + \sigma_1 x + \sigma_2 x^2)^2}\right),$$

with one extra parameter  $\sigma_2$ . This functional form is fitted to 3 different samples and a value for  $\sigma_2$  is extracted for each of them. The 3 samples are the following: (a) a data sample enriched in background by demanding that certain selection cuts are failed (b) the simulated jet sample after applying the same background enrichment procedure as in (a), and (c) the full simulated jet sample. The values of  $\sigma_2$  obtained are then used along with the values of  $\sigma_0$  and  $\sigma_1$  obtained when fitting the data to generate distributions with the same number of events as that observed in data. Then a signal distribution is added, and the signal extraction fit is performed on the resulting composite distribution. The largest difference in the yields is 1.3% and this is taken as the estimate for the systematic uncertainty

Table 6.5: Electroweak contributions to the backgrounds in the  $W \rightarrow e\nu$  cross section measurement as estimated from simulation.

source	fraction of the signal yield (%)
$Z \rightarrow ee, Z \rightarrow \tau\tau$	8.3
$W \rightarrow \tau\nu$	4.5
di-bosons ( $WW, WZ, ZZ$ )	0.13
$t\bar{t}$	0.4
total	13.3

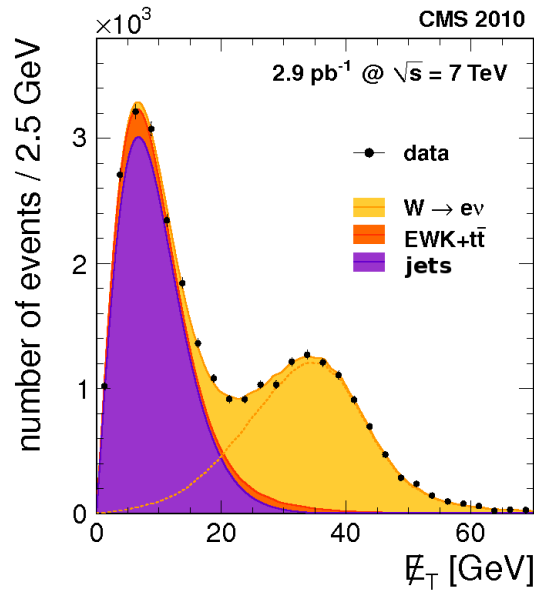


Figure 6.5: The  $\cancel{E}_T$  distribution for the selected  $W \rightarrow e\nu$  candidate sample. The markers represent the data. The component contributions of the fitted template of Eq. (6.7). are also shown.

due to the jet shape modelling.

The final fit to data is shown in Fig. 6.5. The recoil correction can be seen to have significantly improved the description of the signal shape (c.f. Fig. 5.5(d) that has no recoil correction applied). The number of extracted  $W \rightarrow e\nu$  signal events from this fit is  $11\,895 \pm 115$ . The quoted uncertainty is only the statistical error from the fit. The estimate of the jet component of the background from the fit is about 1.3 times the extracted value for the signal. The electroweak contributions to the background are shown in Table 6.5.

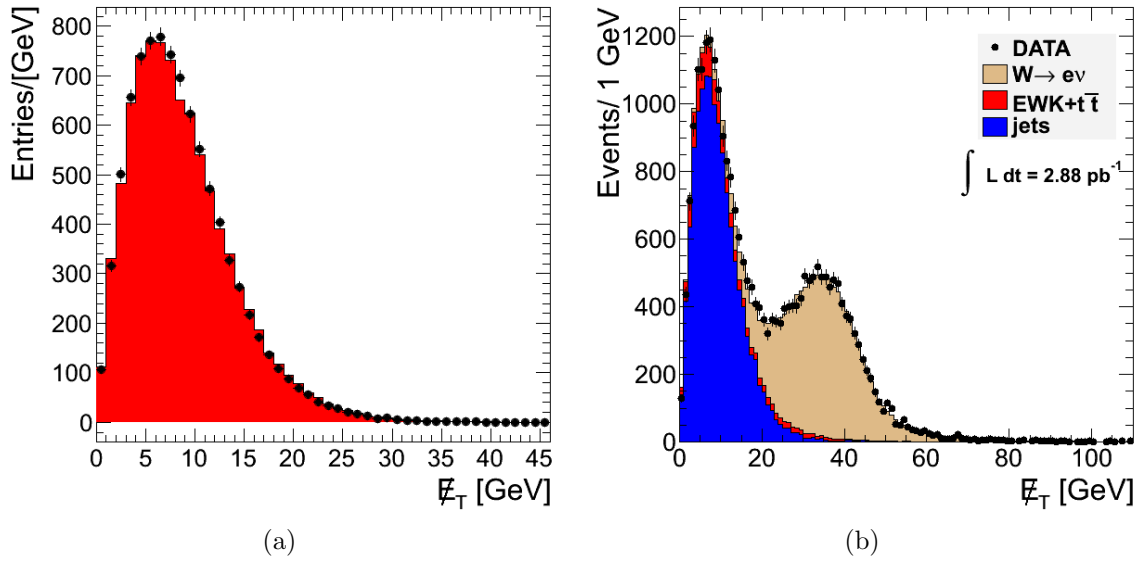


Figure 6.6: (a) Comparison of the  $E_T$  shape of the jet enriched sample described in the text (black points) with the jet distribution after the WP80 selection cuts (histogram). Both distributions are derived from simulated jet events. (b) The data  $E_T$  distribution after the WP80 selection criteria (black points). The result of the maximum likelihood fit is shown in histograms with the contribution of each component shown. The fit is performed in bins of 1 GeV.

The result for the extracted signal yield can be cross-checked with alternative signal and background templates. In the following an alternative jet template is used constructed using an event selection very similar to the candidate event selection, but with the inversion of 2 electron selection cuts<sup>2</sup> so that events from  $W \rightarrow e\nu$  are efficiently excluded. When this template definition is used with simulated jet events the resulting template is found to match the  $E_T$  distribution of simulated jet background events passing the candidate selection, see Fig. 6.6(a). For the signal the same template as before was used. The electroweak background is subtracted using a distribution taken from simulation. The result of the fit is shown in Fig. 6.6(b) and the extracted signal yield is  $11\,760 \pm 116$  events with the uncertainty being the statistical uncertainty of the fit. This number is in agreement within 1.2% with the Rayleigh parameterisation result.

<sup>2</sup>The inverted selection cuts were  $|\Delta\eta_{in}| > 0.004$  (0.007) and  $|\Delta\phi_{in}| > 0.06$  (0.03) for reconstructed electrons in the ECAL barrel (endcaps).

Table 6.6: Numerical values of the terms that appear in Eq. (6.8). The uncertainties shown here include both statistical and systematic uncertainties apart from  $N_W$ , where the uncertainty is purely statistical.

quantity	value
$N_W$	11 895 $\pm$ 115
$A_W\epsilon_{WMC}$	0.446 $\pm$ 0.006
$\rho_{eff}$	0.921 $\pm$ 0.036
$\mathcal{L}$	2.88 $\pm$ 0.32 pb <sup>-1</sup>

## 6.7 Results

The cross section formula quoted in Eq. (6.1) will be rewritten to accommodate the specific methods that have been chosen for this analysis:

$$\sigma(pp \rightarrow W + X) \times BR(W \rightarrow e\nu) = \frac{N_W}{A_W\epsilon_{WMC}\rho_{eff}\mathcal{L}}, \quad (6.8)$$

where the number of  $W \rightarrow e\nu$  signal events,  $N_W$ , is extracted from the fit,  $A_W\epsilon_{WMC}$  is the product of the signal acceptance times the  $W \rightarrow e\nu$  selection efficiency as calculated from simulation,  $\rho_{eff}$  the efficiency correction factor and  $\mathcal{L}$  the integrated luminosity of the data sample.

The numerical values of the terms in Eq. (6.8) are shown in Table 6.6. The uncertainties shown on this table include both statistical and systematic uncertainties apart from  $N_W$ , where the uncertainty is purely statistical. The breakdown of the systematic uncertainties considered for this measurement is shown in detail in Table 6.7.

The systematic uncertainties are listed in Table 6.7. The efficiency uncertainty is the total uncertainty on the correction factor  $\rho_{eff}$  propagated to the cross section result. The signal acceptance uncertainty is the combination of the PDF uncertainty in the generator acceptance and the theoretical uncertainties that are discussed in Section 6.3. The uncertainties in the signal extraction have been discussed in detail in Section 6.6.

Table 6.7: List of systematic uncertainties for the  $W \rightarrow e\nu$  cross section measurement as a percentage of the final cross section result. The luminosity error is considered separately and is not shown here.

source	uncertainty value (%)
Efficiency	3.9
PDF uncertainty on acceptance	0.8
Theoretical uncertainties on acceptance	1.3
Electron energy scale/resolution	2.0
Jet $\cancel{E}_T$ shape modelling	1.3
Signal $\cancel{E}_T$ shape modelling	1.8
Total	5.1

The final cross section measurement result for the inclusive W production is:

$$\sigma(pp \rightarrow W + X) \times BR(W \rightarrow e\nu) = 10.04 \pm 0.10 \text{ (stat)} \pm 0.52 \text{ (syst)} \pm 1.10 \text{ (luminosity) nb,}$$

where the statistical uncertainty in the number of signal events,  $N_W$ , is propagated as the statistical uncertainty on the cross section measurement. The luminosity uncertainty, which is the largest one, is shown separately.

This result is in good agreement with the theoretical prediction:

$$\sigma_{\text{theory}} = 10.44 \pm 0.52 \text{ nb,}$$

which is computed at NNLO with FEWZ [91,92] and the MSTW08 PDF sets [82]. The uncertainties are 68% confidence levels obtaining by combining the NLO PDF and  $\alpha_S$  errors from MSTW08, CTEQ6.6 and NNPDF2.0 groups and adding the NNLO scale uncertainties in quadrature, as prescribed by the PDF4LHC working group [84].

## Summary

In this chapter the electron selections that were derived in Chapter 4 and validated in Chapter 5 are used to select  $W \rightarrow e\nu$  events. The efficiency of the selection criteria for electrons in  $W$  decays were determined by correcting simulation by the measured difference between the efficiency seen in data and simulation in  $Z \rightarrow ee$  decays. The background is subtracted by fitting templates for signal and backgrounds to the data. The measured cross section is in excellent agreement with the theoretical expectations.

# Chapter 7

## Summary and Conclusions

*All truths are easy to understand once they are discovered;  
the point is to discover them.*

Galileo Galilei

### **Electron Identification**

Prompt electrons produced in proton-proton collisions suffer from large backgrounds from either fake electron candidates or real, non-prompt electrons. The majority of this background comes from jets. Simulation was used to study several handles that are helpful in selecting prompt electrons with high efficiency and simultaneously rejecting background electron candidates. In particular, the variables that were studied and optimised are separated into 3 groups: (a) electron candidate isolation sums, calculated as sums of track  $p_T$ , ECAL transverse energy or HCAL tower transverse energy in a cone around the electron candidate and (b) tight requirements in the  $\eta$  and  $\phi$  matching of the track and the clustered energy in the ECAL, ECAL shower width and the ratio of the energy deposited in HCAL behind the electron candidate over the ECAL clustered energy, and (c) variables to reject electrons arising from conversion of photons.

## Electron Selection Tuning

The electron selections that were used for the first CMS measurement of the inclusive  $W \rightarrow e\nu$  and  $Z \rightarrow ee$  cross sections are based on simple cuts on a few key variables. The Iterative Technique can be used to produce electron selections that maximise background rejection for a given electron efficiency. The electron selection cuts used were derived from simulated samples.

## Electron Commissioning with Data

The electron identification variables were studied with collision data and the simulation is found to be in generally good agreement for both prompt electrons and their backgrounds. This validates the electron selections that were derived from simulation with data. The simulation-tuned selections of Chapter 4 were used for electron selection by most CMS physics analyses in 2010.

## Inclusive W cross-section measurement in the electron channel

The inclusive  $W \rightarrow e\nu$  cross section has been measured with  $2.88 \pm 0.32 \text{ pb}^{-1}$  of data. Events were selected to contain a high- $E_T$  ( $E_T > 20 \text{ GeV}$ ) electron that passes a set of electron identification criteria with efficiency close to 80% for  $W \rightarrow e\nu$  electrons. The efficiency of the selection was measured from data using  $Z \rightarrow ee$  events and corrected for the kinematic differences between Z and W electrons using simulation. The remaining backgrounds in the W candidate sample were subtracted using an unbinned maximum likelihood fit of the data  $\cancel{E}_T$  distribution to templates constructed using input from both simulation and data. The measured value for the inclusive W production cross section times the branching ratio of the  $W \rightarrow e\nu$  decay is:

$$\sigma(pp \rightarrow W + X) \times BR(W \rightarrow e\nu) = 10.04 \pm 0.10 \text{ (stat)} \pm 0.52 \text{ (syst)} \pm 1.10 \text{ (lumi.) nb.}$$

where the statistical (stat.) uncertainty reflects the statistical error of the maximum likelihood fit and the systematic error from luminosity (lumi.) is given separately from the rest of the systematic uncertainties (syst.). The measured cross section is in excellent

agreement with the theoretical expectations.

### Conclusions and future prospects

The measurement of the inclusive W cross section in the electron channel that has been presented in this thesis has led to the commissioning of the electron identification variables, the electron selection and the method to measure its efficiency based on Z electrons. Moreover, it provided an opportunity to develop and commission an iterative technique for electron selection tuning, which is proven to be simple, easy-to-implement and faster than other conventional methods.

The dominant uncertainties in this measurement are statistical in nature. This is a motivation of the new cross-section measurement with the whole CMS 2010 dataset (about  $35 \text{ pb}^{-1}$ ) that is currently ongoing. The most important uncertainty now is due to the efficiency measurement and amounts to 3.9% as a fraction of the cross-section result. This figure is related mostly to the available number of Z events and it is expected that it could drop to a total uncertainty of 1.0% with 10 times more integrated luminosity.

More data will enable the application of alternative methods to extract the signal that may lead to a smaller uncertainty than the currently used methods. A potentially more accurate jet template may be studied with the full 2010 dataset that is based on a selection that rejects signal by inverting some of the identification cuts. This approach has the potential to describe the high- $\cancel{E}_T$  tail of the jets better than the Rayleigh-based template since it can account for effects that are difficult or even impossible to parameterise. Preliminary results [104] on this template show that the current 1.3% uncertainty due to the jet template can be reduced to about 0.5%. Other methods beyond the use of templates will also become possible with more data. Methods based on the extrapolation of the jet shape from a background rich to a signal rich region of the phase space, which have also been used at the Tevatron [105,106], need at least twice as much as the current integrated luminosity in order to produce competitive results,

---

but this will not be a problem with the full 2010 dataset. Preliminary studies [104] have shown that the potential of this method is such that the total uncertainty in the signal extraction could drop to around 1%, which is to be compared to the more than 2% that is currently the combined uncertainty due to the signal and jet shape modelling.

The conclusion of the previous discussion is that with increased statistics it is feasible to have a cross-section measurement with total uncertainty<sup>1</sup> of about 2%, which is also the level of the most precise measurement of the  $W$  inclusive cross section at the Tevatron [106]. This measurement will pave the way for a possible future use of the  $W$  production rate as a more precise luminosity estimator as well as a competitive indirect measurement of  $W$  width (see [106] and [5]).

## Epilogue

*No experimental result should be believed until confirmed by theory.*

Michael Turner quoting Sir Arthur Stanley Eddington

This year marks 16 years after the submission of the Technical Proposals for the construction of the ATLAS [107] and CMS [108] experiments and it is the first year that the detectors collect a significant amount of collision data. The first physics papers are being published. Cross-section measurements of  $W$  and  $Z$  production are being published and early measurements for  $t\bar{t}$  production are available, demonstrating the successful commissioning of the experiments.

It is hoped and expected that measurements of Standard Model processes, like the  $W \rightarrow e\nu$  decay that has been the topic of this thesis, will soon be joined by physics discoveries. As the integrated luminosity increases it will become possible to study in detail more and more processes and this will gradually increase the ability of the

---

<sup>1</sup>Excluding the luminosity induced uncertainty.

experiments to distinguish signals indicative of beyond the SM phenomena or so far unobserved SM processes. Establishing signals of any new process will be just the beginning of an even more challenging endeavour. As the quotation in the opening of this section suggests, science is not a mere collection of facts, but rather a quest for understanding what the experimental results indicate about the natural world.

# Bibliography

- [1] W. Lamb and R. Retherford, *Fine Structure of the Hydrogen Atom by a Microwave Method*, Phys. Rev. 72, 241 (1947).
- [2] J. Chadwick, *The intensity distribution in the magnetic spectrum of beta particles from radium* (in German), Verhandl Dtsch. Phys. Ges. 16, 383 (1914).
- [3] W. Pauli, *Letter to L. Meitner*, Wissenschaftlicher Briefwechsel mit Bohr, Einstein, Heisenberg, u.a., Bd.2, Letter 259 (1930). CERN Archive Record URL: <http://cdsweb.cern.ch/record/83282>
- [4] D.H. Perkins, *Introduction to High Energy Physics*, Third Edition, Addison - Wiley Publishing Company, Inc., (1987).
- [5] K. Nakamura et al. (Particle Data Group), *Review of Particle Physics*, J. Phys. G 37, 075021 (2010).
- [6] E. Fermi, *An attempt of a theory of beta radiation* (in German), Z. Phys. 88, 161 (1934).
- [7] P. W. Higgs, *Broken symmetries, massless particles and gauge fields*, Phys. Lett. 12, 132 (1964).
- [8] F. Englert and R. Brout, *Broken Symmetry and the Mass of Gauge Vector Mesons*, Phys. Rev. Lett. 13, 321 (1964).

- [9] G. S. Guralnik et al., *Global Conservation Laws and Massless Particles*, Phys. Rev. Lett. 13, 585 (1964).
- [10] E. Leader and E. Predazzi, *An Introduction to Gauge Theories and Modern Particle Physics, Volume I*, Cambridge University Press (1996).
- [11] M. S. Sozzi, *Discrete Symmetries and CP violation*, Oxford University Press (2008).
- [12] M. Chanowitz, *The No-Higgs Signal: Strong WW Scattering at the LHC*, Physics at LHC 2004 Conf. Proc., Czech.J.Phys. 55 B45-B58 (2005). Preprint: arXiv:hep-ph/0412203v1.
- [13] D. Balin and A. Love, *Supersymmetric gauge field theory and string theory*, Taylor & Francis, (1996).
- [14] I. Aitchison, *Supersymmetry and the MSSM: An Elementary Introduction*, preprint: hep-ph/0505105v1 (2005).
- [15] E. Komatsu et al., *Five-Year Wilkinson Microwave Anisotropy Probe (WMAP) Observations: Cosmological Interpretation*, ApJS, 180, 330-376 (2009).
- [16] T Bringmann, *Particle models and the small-scale structure of dark matter*, New J. Phys. 11 105027 (2009).
- [17] H. Baer et al., *Collider, direct and indirect detection of supersymmetric dark matter*, New J. Phys. 11 105024 (2009).
- [18] R. Technini and C. Verzegnassi, *The Physics of the Z and W Bosons*, World Scientific (2008).
- [19] D. Denegri, *The discovery of the W and Z*, Phys. Reports 403-404, 107 (2004).

- [20] The UA1 Collaboration, *Experimental Observation of Isolated Large Transverse Energy Electrons with Associated Missing Energy at  $\sqrt{s} = 540$  GeV*, Phys. Lett. B 122, 103 (1983).
- [21] The UA1 Collaboration, *Further Evidence for Charged Intermediate Vector Bosons at the SPS Collider.*, Phys. Lett. B 129, 273 (1983).
- [22] G. Altarelli and M. Grunewald, *Precision Electroweak Tests of the Standard Model*, CERN-PH-TH/2004-067 (2004).
- [23] LEP Electroweak Working Group, <http://lepewwg.web.cern.ch/LEPEWWG>
- [24] Tevatron Electroweak Working Group, <http://tevewwg.fnal.gov/>
- [25] The LEP Working Group, *LEP Design Report*, CERN-LEP/84-01, Internal report, CERN (1984).
- [26] SLC Working Group, *SLAC Linear Collider Conceptual Design Report*, SLAC-R-229, Internal report, SLAC (1980).
- [27] The ALEPH Collaboration, *ALEPH: A Detector for electron-positron annihilations at LEP*, Nucl. Instrum. Meth. A294, 121-178 (1990).
- [28] The DELPHI Collaboration, *The DELPHI Detector at LEP*, Nucl. Instrum. Meth. A303, 233 (1991).
- [29] The L3 Collaboration, *The Construction Of The L3 Experiment*, Nucl. Instrum. Meth. A289, 35 (1990).
- [30] The OPAL Collaboration, *The OPAL Detector at LEP*, Nucl. Instrum. Meth. A305, 275 (1991).
- [31] The CDF Collaboration, *The CDF Detector: An Overview*, Nucl. Instrum. Meth. A271, 387 (1988).
- [32] The D0 Collaboration, *The D0 Detector*, Nucl. Instrum. Meth. A338, 185 (1994)

- [33] Hasert et al., *Search For Elastic Muon-Neutrino Electron Scattering*, Phys. Lett. B46, 138 (1973).
- [34] The ALEPH, DELPHI, L3, OPAL, SLD Collaborations, the LEP Electroweak Working Group, the SLD Electroweak and Heavy Flavour Groups, *Precision Electroweak Measurements on the Z Resonance*, Phys. Rept. 427, 257 (2006).
- [35] R. Ofierzynski, *W boson mass and properties at LEP*, J. of Phys.: Conf. Series 110, 042019 (2008).
- [36] D. Glenzinski and U. Heintz, *Precision Measurements of the W Boson Mass*, Annu. Rev. Nucl. Part. Sci. 50, 207 (2000).
- [37] S.D. Drell and T.M. Yan, *Massive lepton-pair production in hadron-hadron collisions at high energies*, Phys. Rev. Lett. 25, 316 (1970).
- [38] The CMS Collaboration, *Measurement of the W-boson charge asymmetry*, CMS PAPER EWK-10-006 (2010).
- [39] A. Martin et al., *Parton distributions and the LHC: W and Z production*, Eur. Phys. J., C14, 133 (1999).
- [40] The LHC Study Group, *The Large Hadron Collider Conceptual Design*, CERN-AC-95-05 (1995).
- [41] L. Evans and P. Bryant (editors), *The LHC Machine*, JINST 3, S08001 (2008).
- [42] CERN Press Release PR09.08 (20.9.2008)  
URL: <http://press.web.cern.ch/press/PressReleases/Releases2008/PR09.08E.html>
- [43] S. Myers, *Report on the LHC*, to appear in the Proceedings of ICHEP '10, 35th International Conference on High Energy Physics, 22-28 July, Paris.
- [44] The ALICE Collaboration, *The ALICE Experiment at the CERN Large Hadron Collider*, JINST 3, S08002 (2008).

- [45] The ATLAS Collaboration, *The ATLAS Experiment at the CERN Large Hadron Collider*, JINST 3, S08003 (2008).
- [46] The CMS Collaboration, *The CMS Experiment at the CERN Large Hadron Collider*, JINST 3, S08004 (2008).
- [47] The LHCb Collaboration, *The LHCb Detector at the Large Hadron Collider*, JINST 3, S08005 (2008).
- [48] The LHCf Collaboration, *The LHCf Detector at the CERN Large Hadron Collider*, JINST 3, S08006 (2008).
- [49] The TOTEM Collaboration, *The TOTEM Experiment at the CERN Large Hadron Collider*, JINST 3, S08007 (2008).
- [50] The ATLAS Collaboration, *ATLAS high-level trigger, data-acquisition and controls: Technical Design Report*, CERN-LHCC-2003-022 (2003).
- [51] V. I. Klyukhin et al., *Measurement of the CMS magnetic field*, IEEE Trans. on Applied Superc. 18, No 2, 395 (2008).
- [52] The CMS Collaboration, *Precise mapping of the magnetic field in the CMS Barrel Yoke using cosmic rays*, CMS PAPER CFT-09-015 (2009).
- [53] V. Ciulli, *The CMS Silicon Strip Tracker: from integration to start-up*, CMS CR-2008/001 (2008).
- [54] The CMS Collaboration, *Tracking and Vertexing Results from First Collisions*, CMS PAS TRK-10-001 (2010).
- [55] The CMS Collaboration, *Tracking and Primary Vertex Results in First 7 TeV Collisions*, CMS PAS TRK-10-005 (2010).
- [56] The Worldwide LHC Computing Grid,  
URL: <http://lcg.web.cern.ch/lcg/>

- [57] M.Campanella and I.Perini, *The analysis model and the optimisation of the geographical distribution of computing resources*, MONARC Note 98/1 (1998).  
URL: <http://monarc.web.cern.ch/MONARC>
- [58] The CMS Collaboration, *Jet performance in pp collisions at 7 TeV*, CMS PAS JME-10-003 (2010).
- [59] Wigmans, *Calorimetry: Energy Measurement in Particle Physics*, Oxford University Press (2000).
- [60] P. Lecoq et al., *Lead tungstate (PbWO<sub>4</sub>) scintillators for LHC EM calorimetry*, Nucl. Instrum. Meth. A 365, 291 (1995).
- [61] H.F. Chen et al., *Radiation damage measurements of undoped lead tungstate crystals for the CMS electromagnetic calorimeter at LHC*, Nucl. Instrum. Meth. A 414, 149 (1998).
- [62] I. Dafinei et al., *Lead tungstate for high energy calorimetry*, Mat. Res. Soc. Symp. Proc. 348, 99 (1994).
- [63] H. Jung and A. D. Roeck (editors), *HERA and the LHC*, DESY-PROC-2009-02, (2009).
- [64] R. Frhwirth, *Application of Kalman filtering to track and vertex fitting*, Nucl. Instr. and Meth. A 262, 144 (1987).
- [65] W. Adam et al., *Reconstruction of electrons with the Gaussian-sum filter in the CMS tracker at the LHC*, J. Phys. G: Nucl. Part. Phys. 31 N9-N20 (2005).
- [66] S. Baffioni et al., *Electron reconstruction in CMS*, Eur. Phys. J. C 49, 1099 (2007).
- [67] F. James, *Statistical Methods in Experimental Physics*, 2nd Edition, World Scientific (2006).
- [68] C. Bishop, *Pattern Recognition and Machine Learning*, Springer (2006).

- [69] Goldberg D., *Genetic Algorithms in Search, Optimization and Machine Learning*, Addison Wesley (1989).
- [70] The CMS Collaboration, *Towards a Measurement of the Inclusive  $W \rightarrow e\nu$  and  $\gamma^*/Z \rightarrow ee$  Cross Section in  $pp$  Collisions at  $\sqrt{10}$  TeV*, CMS PAS EWK-09-004 (2009).
- [71] The CMS Collaboration, *Measurements of Inclusive  $W$  and  $Z$  Cross Sections at 7 TeV*, to appear in the Proceedings of ICHEP '10, 35th International Conference on High Energy Physics, 22-28 July, Paris.
- [72] The CMS Collaboration, *Measurements of Inclusive  $W$  and  $Z$  Cross Sections at 7 TeV*, JHEP 01, 080 (2011).
- [73] T. Sjöstrand et al., *PYTHIA 6.4, Physics and Manual*, JHEP05, 026 (2006).
- [74] U. Baur et al., *QCD corrections to hadronic  $W\gamma$  production with nonstandard  $WW\gamma$  couplings*, Phys. Rev. D 48, 5140 (1993).
- [75] S. Agostinelli et al., *GEANT 4: A simulation toolkit*, Nucl. Instr. and Meth. in Phys. Res. Section A 506, 3, 250 (2003).
- [76] The CMS Collaboration, *Commissioning of the Particle-flow Event Reconstruction with the first LHC collisions recorded in the CMS detector*, CMS PAS PFT-10-001 (2010).
- [77] The CMS Collaboration, *Commissioning of the Particle-Flow reconstruction in Minimum Bias and Jet events at  $pp$  Collisions at 7TeV*, CMS PAS PFT-10-002 (2010).
- [78] M. Cacciari et al., *The anti- $k_T$  jet clustering algorithm*, JHEP 04, 063 (2008).
- [79] P. Nason, *A new method for combining NLO QCD with shower Monte Carlo algorithms*, JHEP 11, 040 (2004).

- [80] S. Frixione et al., *Matching NLO QCD computations with Parton Shower simulations: the POWHEG method*, JHEP 11, 070 (2007).
- [81] P.M. Nadolsky et al., *Implications of CTEQ global analysis for collider observables*, Phys. Rev. D 78, 013004 (2008).
- [82] A.D Martin et al., *Parton distributions for the LHC*, Eur. Phys. J. C63, 189 (2009).
- [83] R. D. Ball et al., *A first unbiased global NLO determination of parton distributions and their uncertainties*, preprint: arXiv:1002.4407 (2010)
- [84] PDF4LHC Working Group,  
<http://www.hep.ucl.ac.uk/pdf4lhcrecom.pdf>
- [85] G. A. Ladinsky and C. P. Yuan, *The Nonperturbative regime in QCD resummation for gauge boson production at hadron colliders*, Phys. Rev. D50, 4239 (1994).
- [86] C. Balazs et al., *Effects of QCD resummation on distributions of leptons from the decay of electroweak vector bosons*, Phys. Lett. B355, 548 (1995).
- [87] C. Balazs and C. P. Yuan, *Testing multiple gluon dynamics at the Tevatron*, Phys. Rev. Lett. 79, 2398 (1997).
- [88] C. Balazs and C. P. Yuan, *Soft gluon effects on lepton pairs at hadron colliders*, Phys. Rev. D56, 5558 (1997).
- [89] F. Landry et al., *Tevatron Run-1 Z boson data and Collins-Soper-Sterman resummation formalism*, Phys. Rev. D67, 073016 (2003).
- [90] A. V. Konychev and P. M. Nadolsky, *Universality of the Collins-Soper-Sterman nonperturbative function in gauge boson production*, Phys. Lett. B633, 710 (2006).
- [91] K. Melnikov and F. Petriello, *Electroweak gauge boson production at hadron colliders through  $O(\alpha_s^2)$* , Phys. Rev. D74 (2006) 114017.

- [92] K. Melnikov and F. Petriello, *The W boson production cross section at the LHC through  $O(\alpha_s^2)$* , Phys. Rev. Lett. 96, 231803 (2006).
- [93] C. M. Carloni Calame et al., *Precision electroweak calculation of the production of a high transverse-momentum lepton pair at hadron colliders*, JHEP 10, 109 (2007).
- [94] C. M. Carloni Calame et al., *Precision electroweak calculation of the charged current Drell-Yan process*, JHEP 12, 016 (2006).
- [95] C. M. Carloni Calame et al., *Multiple photon corrections to the neutral-current Drell-Yan process*, JHEP 05, 019 (2005).
- [96] C. M. Carloni Calame et al. *Higher-order QED corrections to W-boson mass determination at hadron colliders*, Phys. Rev. D69, 037301 (2004).
- [97] N. Adam et al., *Theoretical Uncertainties in Electroweak Boson Production Cross Sections at 7, 10, and 14 TeV at the LHC*, JHEP 11, 074 (2010).
- [98] M. J. Oreglia, *A Study of the Reactions  $\psi' \rightarrow \gamma\gamma\psi$* , Ph.D. Thesis, SLAC-R-236 (1980).  
URL: <http://www.slac.stanford.edu/pubs/slacreports/slac-r-236.html>
- [99] S. Van der Meer, *Calibration of the effective beam height in the ISR*, CERN-ISR-PO/68-31 (1968).
- [100] The CMS Collaboration, *Measurement of CMS Luminosity*, CMS PAS EWK-10-004 (2010).
- [101] The CMS Collaboration, *Electromagnetic calorimeter commissioning and performance with 7 TeV data*, CMS PAS EGM-10-002 (2010).
- [102] The CMS Collaboration, *Electromagnetic calorimeter calibration with 7 TeV data*, CMS PAS EGM-10-003 (2010).

- [103] Z. Was, *TAUOLA the library for  $\tau$  lepton decay, and KKMC/KORALB/KORALZ status report*, Nucl. Phys. B, Proc. Suppl. 98, 96 (2001).
- [104] The CMS Collaboration, *Measurement of the inclusive W and Z cross sections in pp collisions at  $\sqrt{s} = 7$  TeV*, CMS PAS EWK-10-005 (2010), in preparation.
- [105] The D0 Collaboration, *Extraction of the width of the W boson from measurements of the  $\sigma(p\bar{p} \rightarrow W + X)B(W \rightarrow e\nu)$  and  $\sigma(p\bar{p} \rightarrow Z + X)B(Z \rightarrow ee)$  and their ratio*, Phys. Rev. D 61, 072001 (2000).
- [106] The CDF Collaboration, *Measurement of the inclusive W and Z cross sections in  $p\bar{p}$  collisions at  $\sqrt{s} = 1.96$  TeV*, J. Phys. G: Nucl. Part. Phys. 34, 2457 (2007).
- [107] The ATLAS Collaboration, *ATLAS Technical Proposal*, CERN/LHCC 94-43 (1994).
- [108] The CMS Collaboration, *The Compact Muon Solenoid Technical Proposal*, CERN/LHCC 94-38 (1994).

# Appendix A

## Electron Candidates after WP80

### and $\cancel{E}_T > 30 \text{ GeV}$

This appendix contains the distributions of the electron identification variables (see Section 3.3) for the single electron samples defined in Section 5.1 for electrons satisfying all the WP80 selection cuts (see Table 4.1) apart from the cut in the variable that is plotted. The cut on the  $\Delta\eta_{in}$  variable is not applied to electrons reconstructed in the ECAL endcaps. The events are further demanded to have  $\cancel{E}_T > 30 \text{ GeV}$  in order to enrich the samples in electrons from W decays. Black points correspond to data and histograms to simulated samples. See Section 5.2 for details.

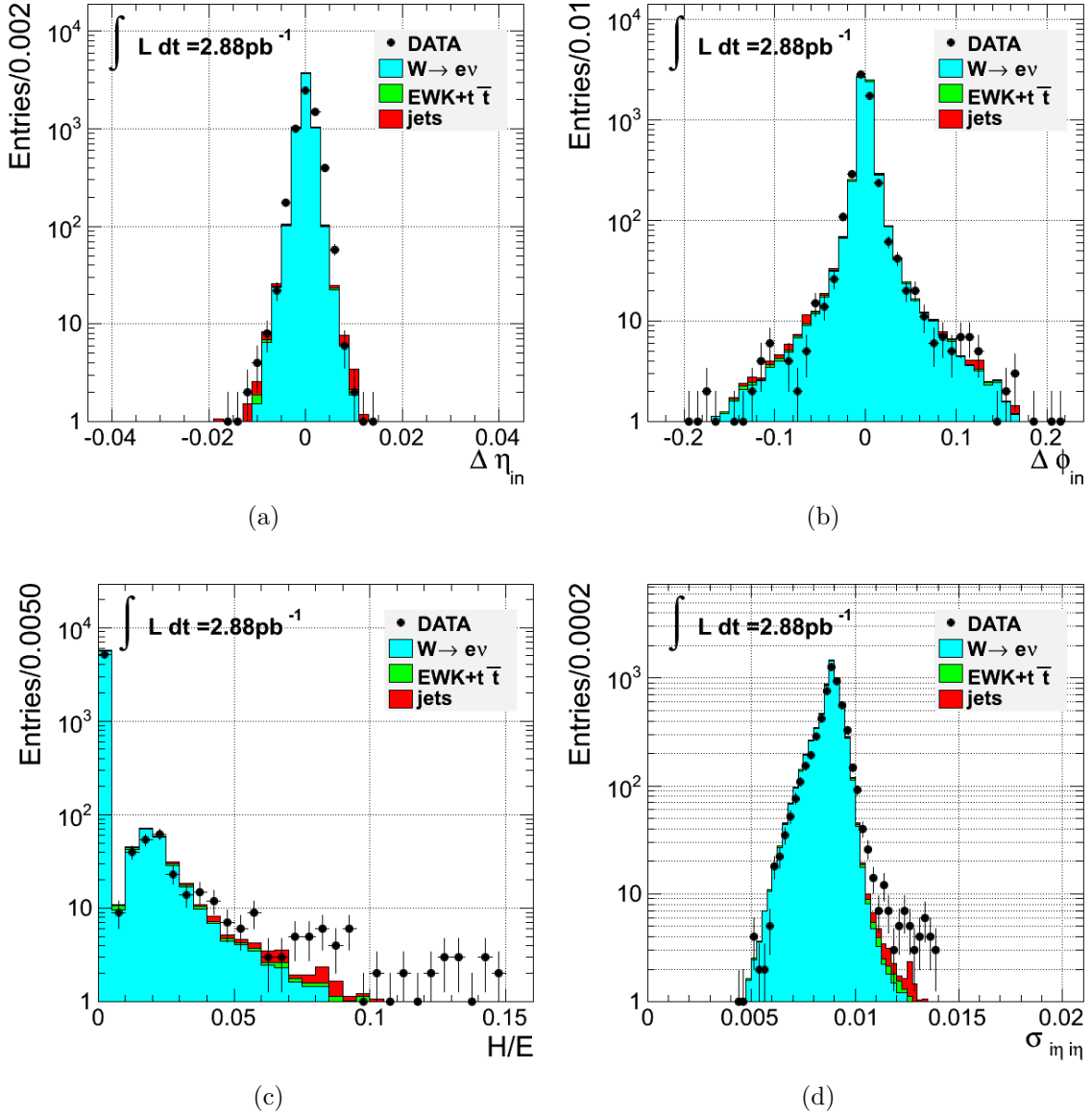


Figure A.1: Distributions of shower shape and track-supercluster matching variables used in electron identification for electrons in the ECAL barrel that pass the cuts of the WP80 selection excluding the cut on the variable that is being plotted. A further requirement of  $\cancel{E}_T > 30$  GeV is applied. See Section 5.2 for details.

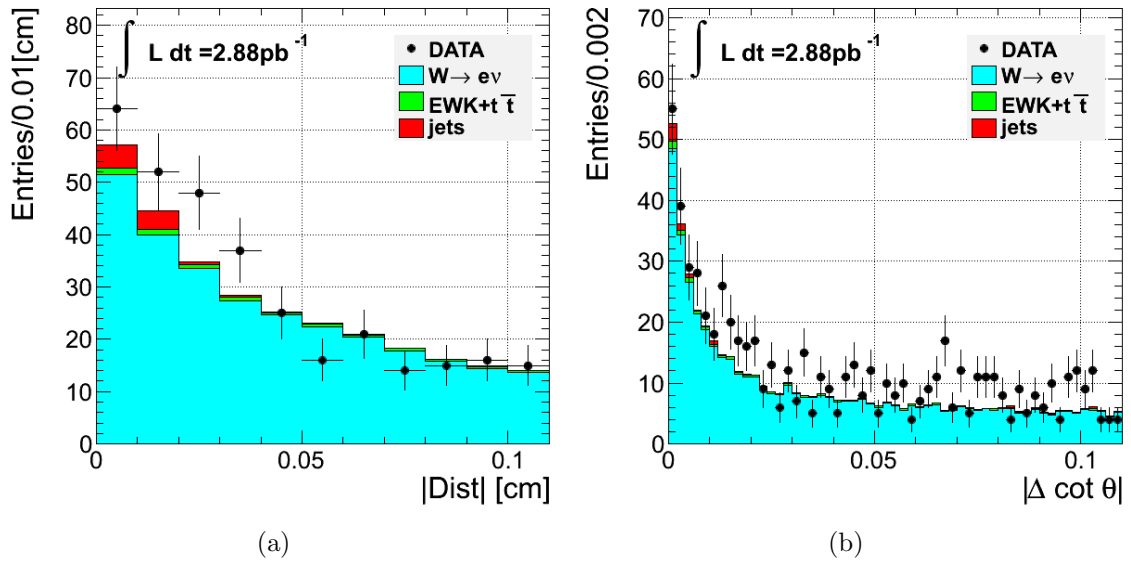


Figure A.2: Distributions of  $\Delta \cot \theta$  and  $\text{Dist}$  variables for electrons with a conversion partner track candidate in the ECAL barrel that pass the cuts of the WP80 selection without the conversion rejection criterion based on the identification of a conversion partner track. A further requirement of  $\cancel{E}_T > 30$  GeV is applied. See Section 5.2 for details.

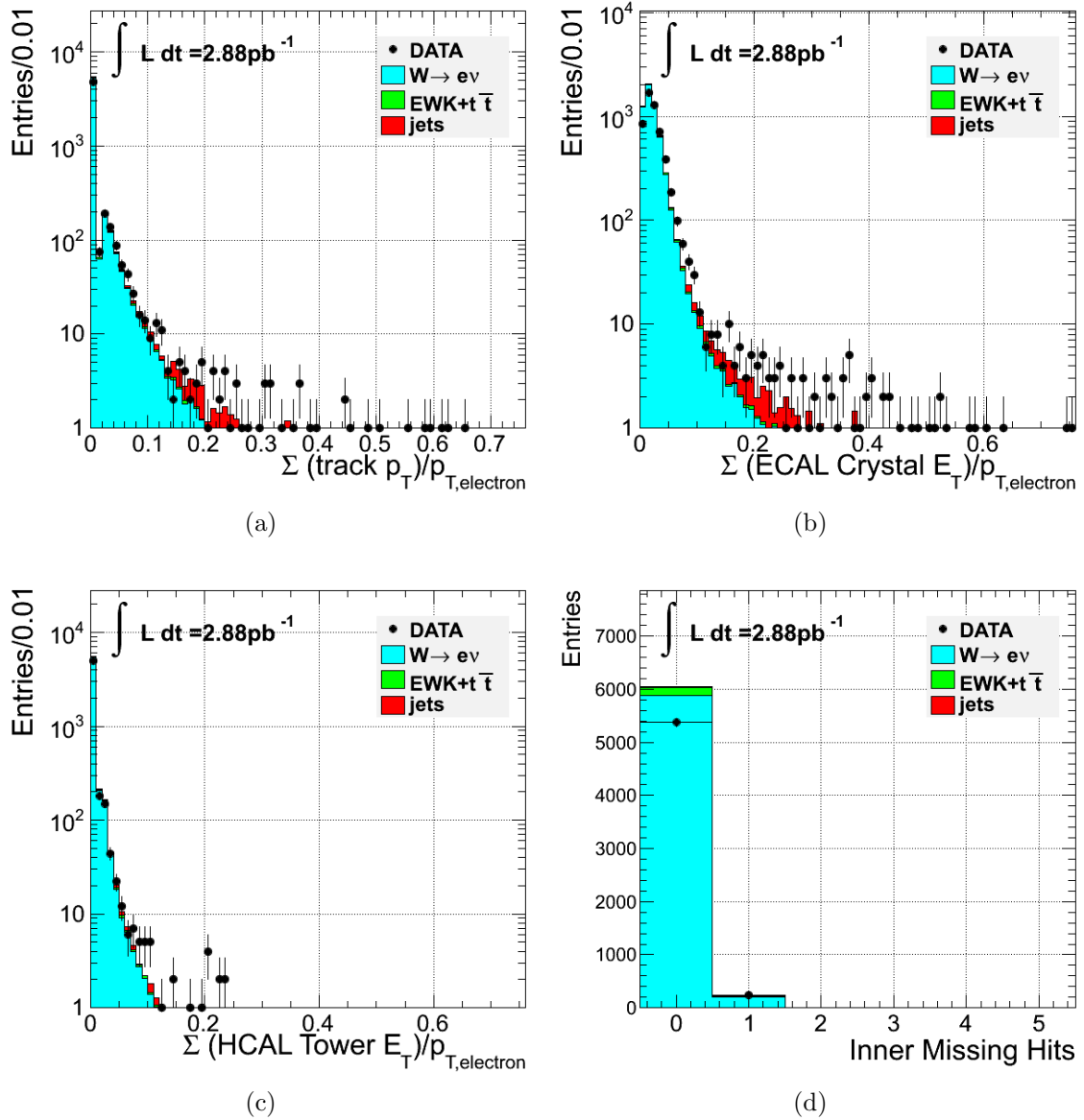


Figure A.3: Distributions of isolation variables and missing inner hits used in electron identification for electrons in the ECAL barrel that pass the cuts of the WP80 selection excluding the cut on the variable that is being plotted. A further requirement of  $\cancel{E}_T > 30$  GeV is applied. See Section 5.2 for details.

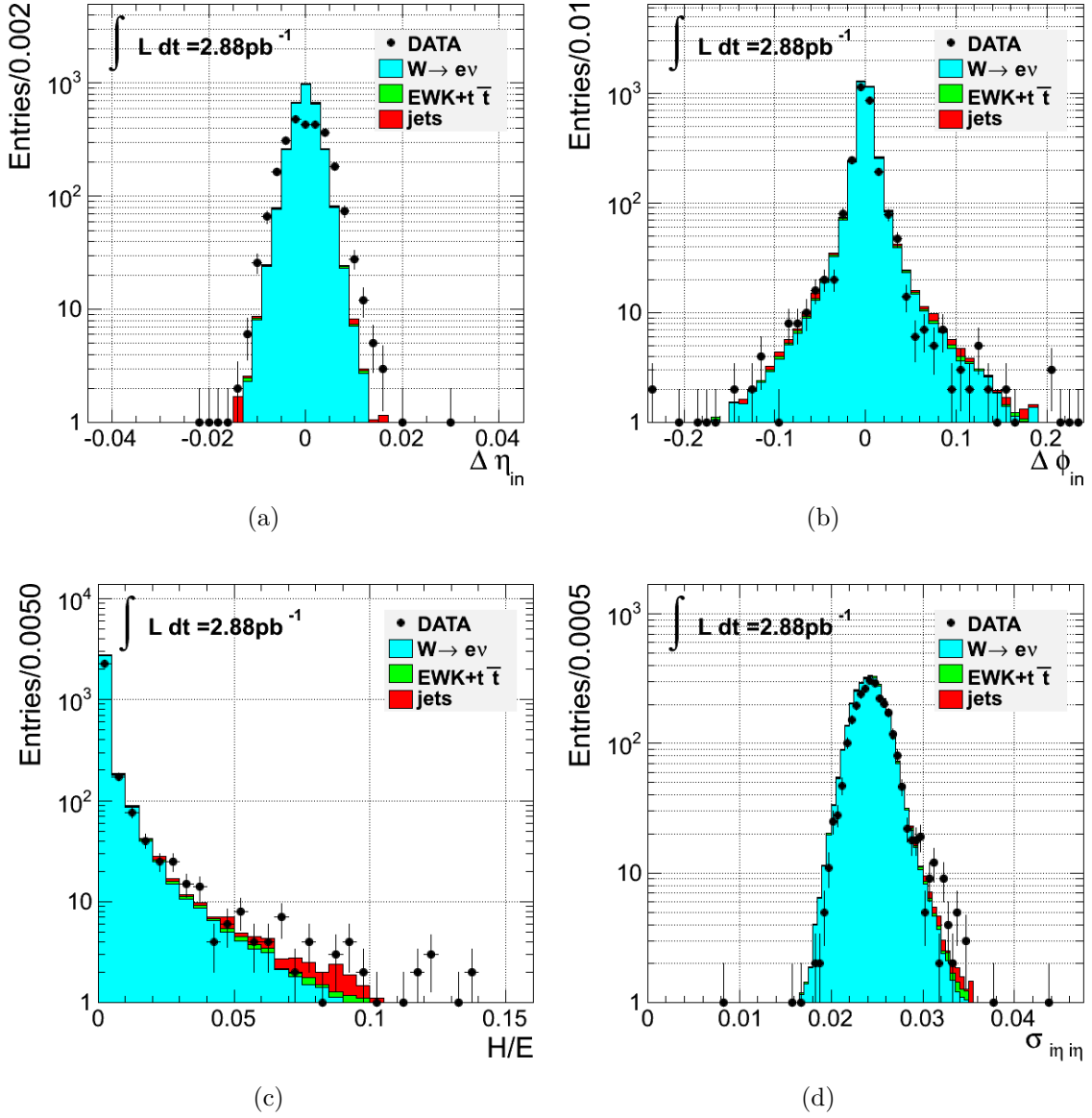


Figure A.4: Distributions of shower shape and track-supercluster matching variables used in electron identification for electrons in the ECAL endcaps that pass the cuts of the WP80 selection excluding the cut on the variable that is being plotted. The  $\Delta\eta_{in}$  variable is corrected using an *ad hoc* correction, which, however, is not perfect. A further requirement of  $\cancel{E}_T > 30$  GeV is applied. See Section 5.2 for details.

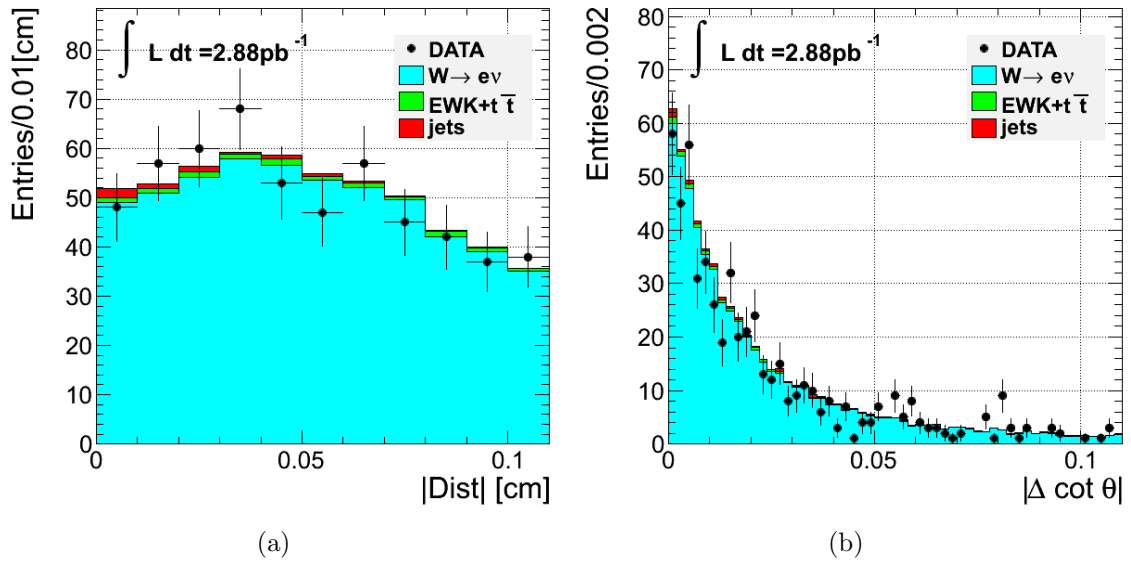


Figure A.5: Distributions of  $\Delta \cot \theta$  and  $Dist$  variables for electrons with a conversion partner track candidate in the ECAL endcaps that pass the cuts of the WP80 selection without the conversion rejection criterion based on the identification of a conversion partner track. A further requirement of  $\cancel{E}_T > 30$  GeV is applied. See Section 5.2 for details.

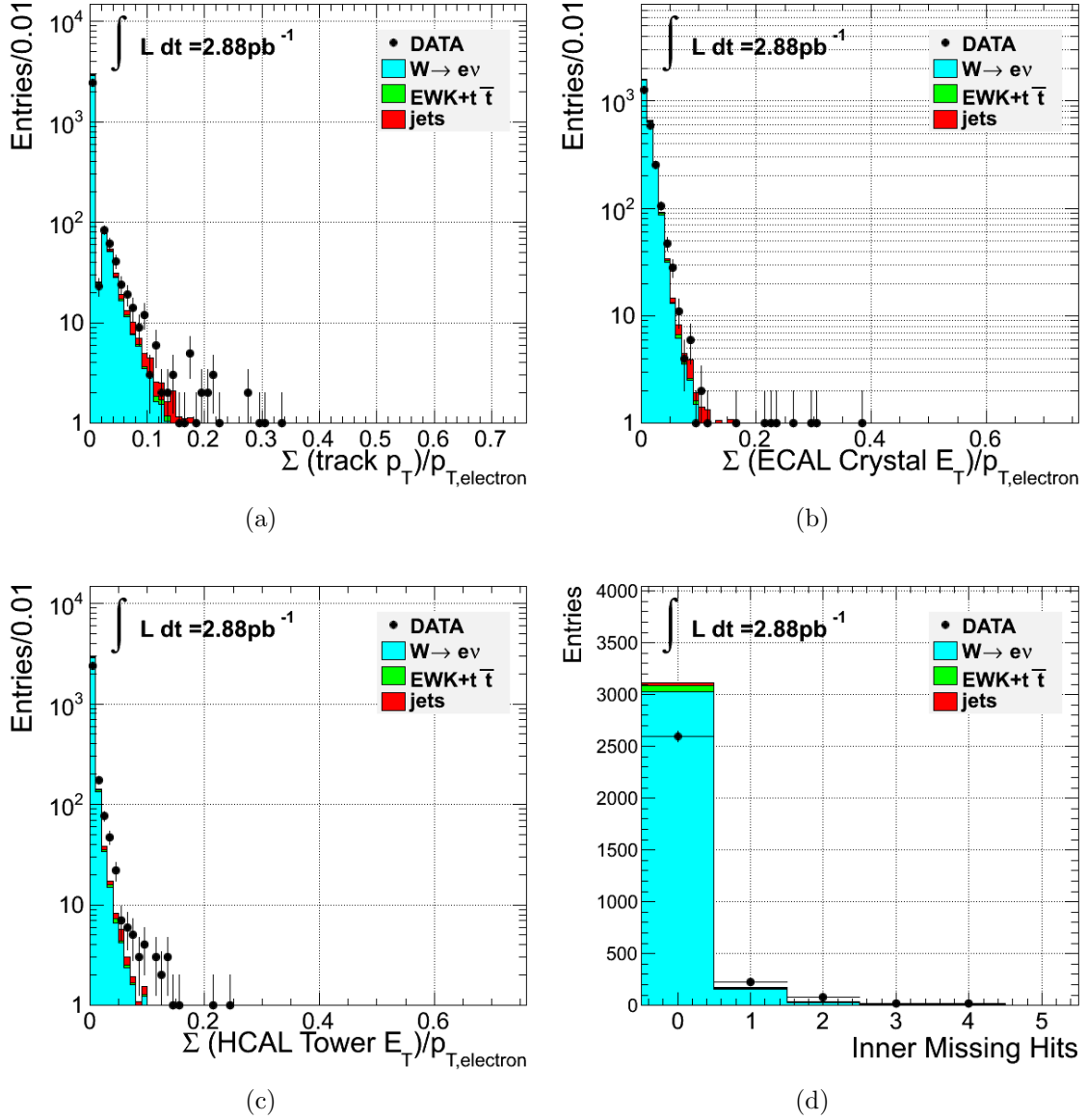


Figure A.6: Distributions of isolation variables and inner missing hits used in electron identification for electrons in the ECAL endcaps that pass the cuts of the WP80 selection excluding the cut on the variable that is being plotted. A further requirement of  $E_T > 30 \text{ GeV}$  is applied. See Section 5.2 for details.

# Appendix B

## Electron Candidates after WP80

This appendix contains the distributions of the electron identification variables (see Section 3.3) for the single electron samples defined in Section 5.1 for electrons satisfying all the WP80 selection cuts (see Table 4.1) apart from the cut in the variable that is plotted. The cut on the  $\Delta\eta_{in}$  variable is not applied to electrons reconstructed in the ECAL endcaps. Black points correspond to data and histograms to simulated samples. See Section 5.2 for details.

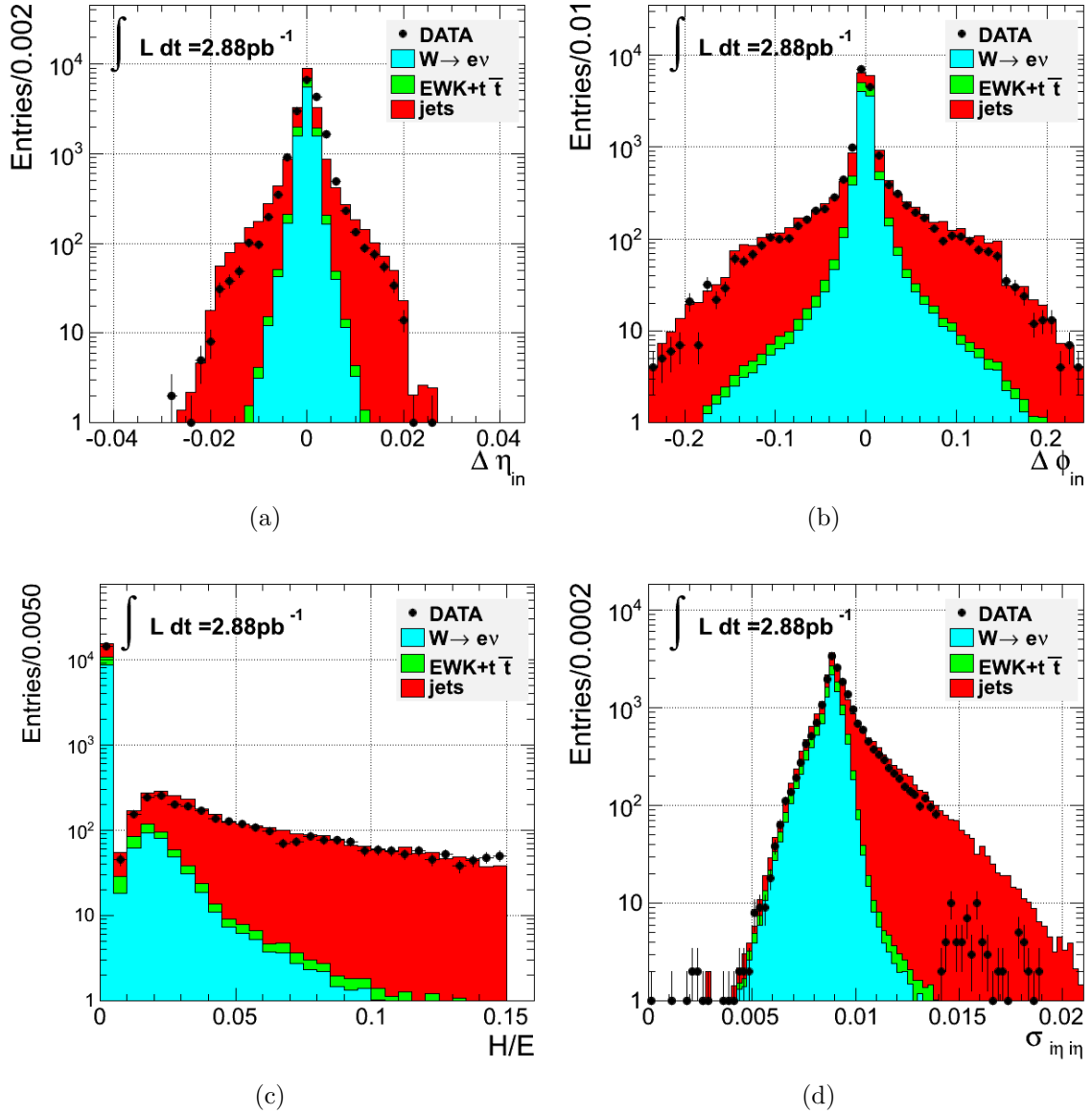


Figure B.1: Distributions of shower shape and track-supercluster matching variables used in electron identification for electrons in the ECAL barrel that pass the cuts of the WP80 selection excluding the cut on the variable that is being plotted. The discrepancy in the high values of  $\sigma_{\eta_{in}}$  is due to the trigger path that is used in the data, which implements a loose cut, as far as prompt electrons are concerned, on this variable (see Section 5.1). This cut is not applied on the simulated data. See Section 5.2 for details.

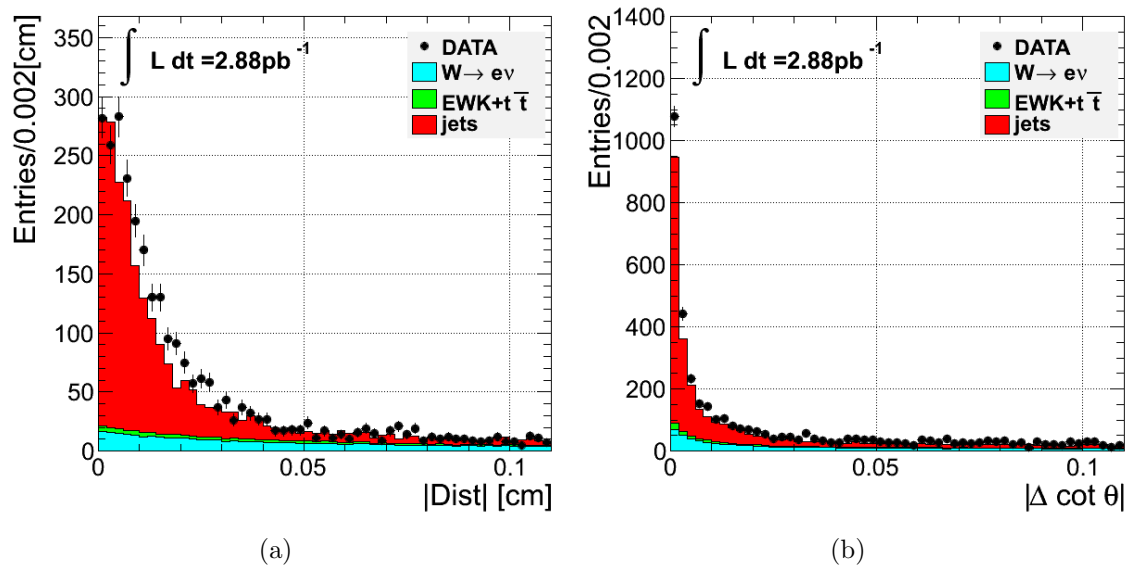


Figure B.2: Distributions of  $\Delta \cot \theta$  and  $\text{Dist}$  variables for electrons with a conversion partner track candidate in the ECAL barrel that pass the cuts of the WP80 selection without the conversion rejection criterion based on the identification of a conversion partner track. See Section 5.2 for details.

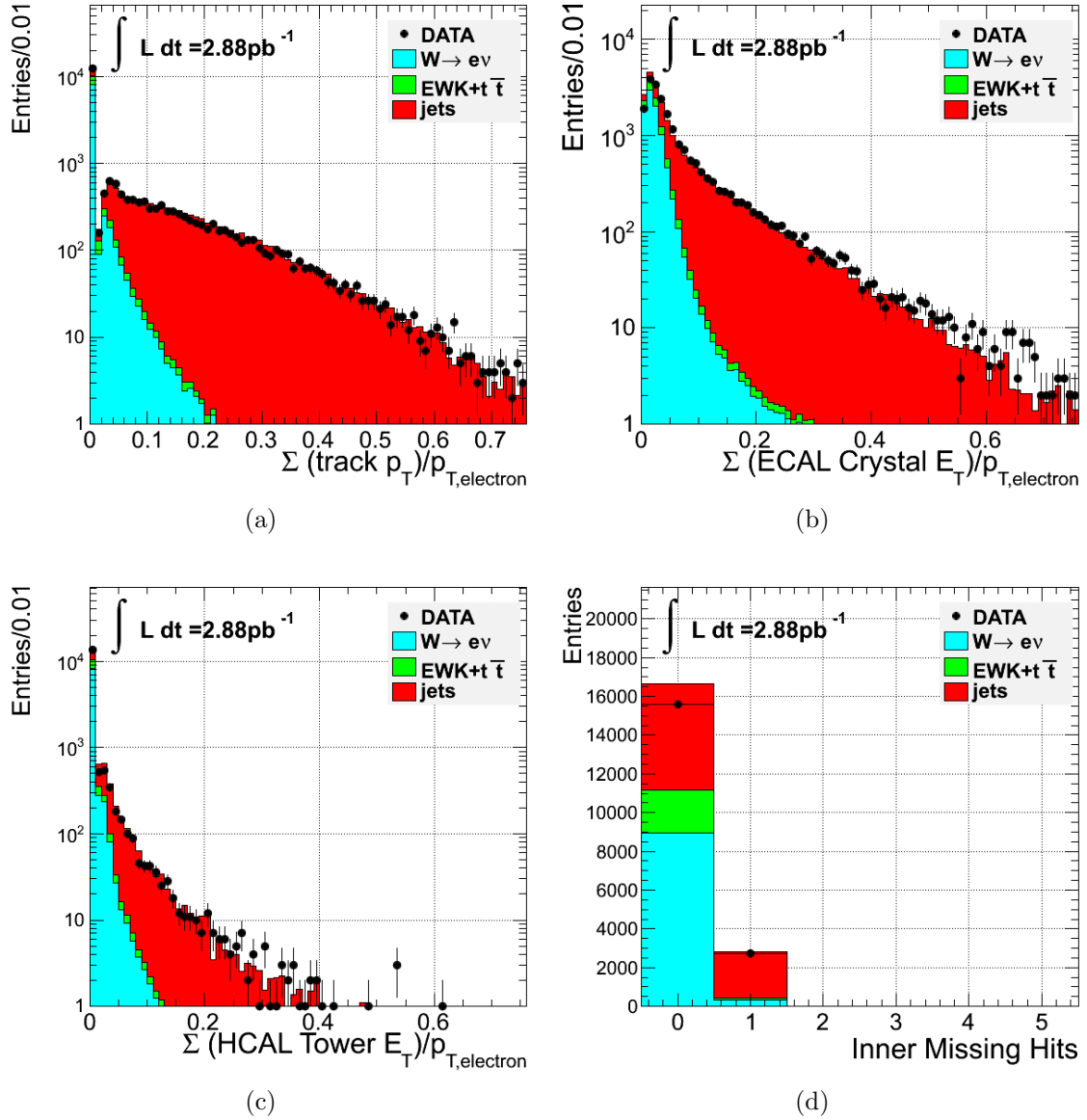


Figure B.3: Distributions of isolation variables and missing inner hits used in electron identification for electrons in the ECAL barrel that pass the cuts of the WP80 selection excluding the cut on the variable that is being plotted. See Section 5.2 for details.

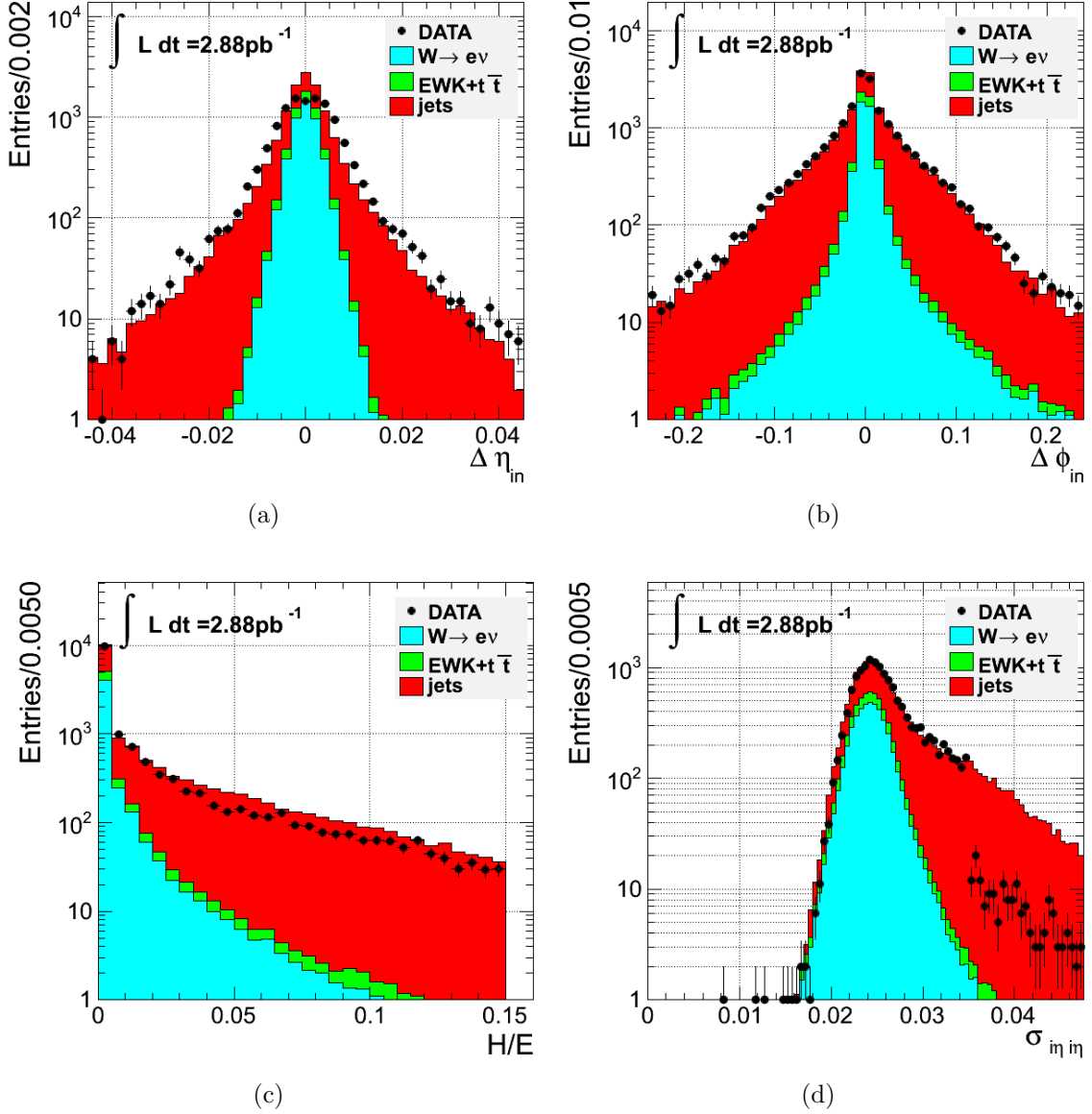


Figure B.4: Distributions of shower shape and track-supercluster matching variables used in electron identification for electrons in the ECAL endcaps that pass the cuts of the WP80 selection excluding the cut on the variable that is being plotted. The  $\Delta\eta_{in}$  variable is corrected using an *ad hoc* correction, which, however, is not perfect. The discrepancy in the high values of  $\sigma_{in\ in}$  is due to the trigger path that is used in the data, which implements a loose cut, as far as prompt electrons are concerned, on this variable (see Section 5.1). This cut is not applied on the simulated data. See Section 5.2 for details.

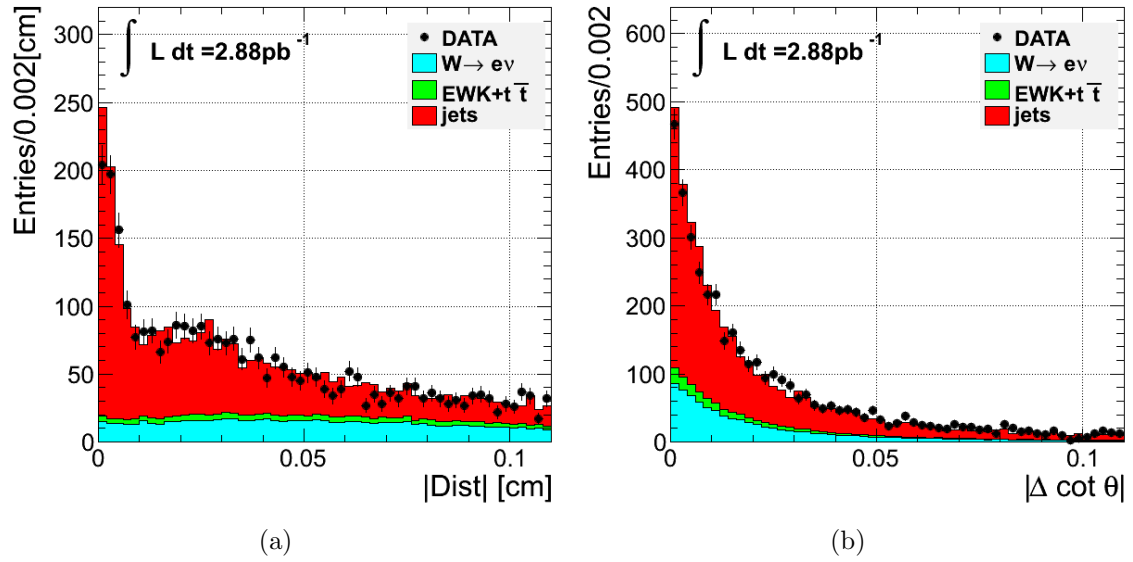


Figure B.5: Distributions of  $\Delta \cot \theta$  and Dist variables for electrons with a conversion partner track candidate in the ECAL endcaps that pass the cuts of the WP80 selection without the conversion rejection criterion based on the identification of a conversion partner track. See Section 5.2 for details.

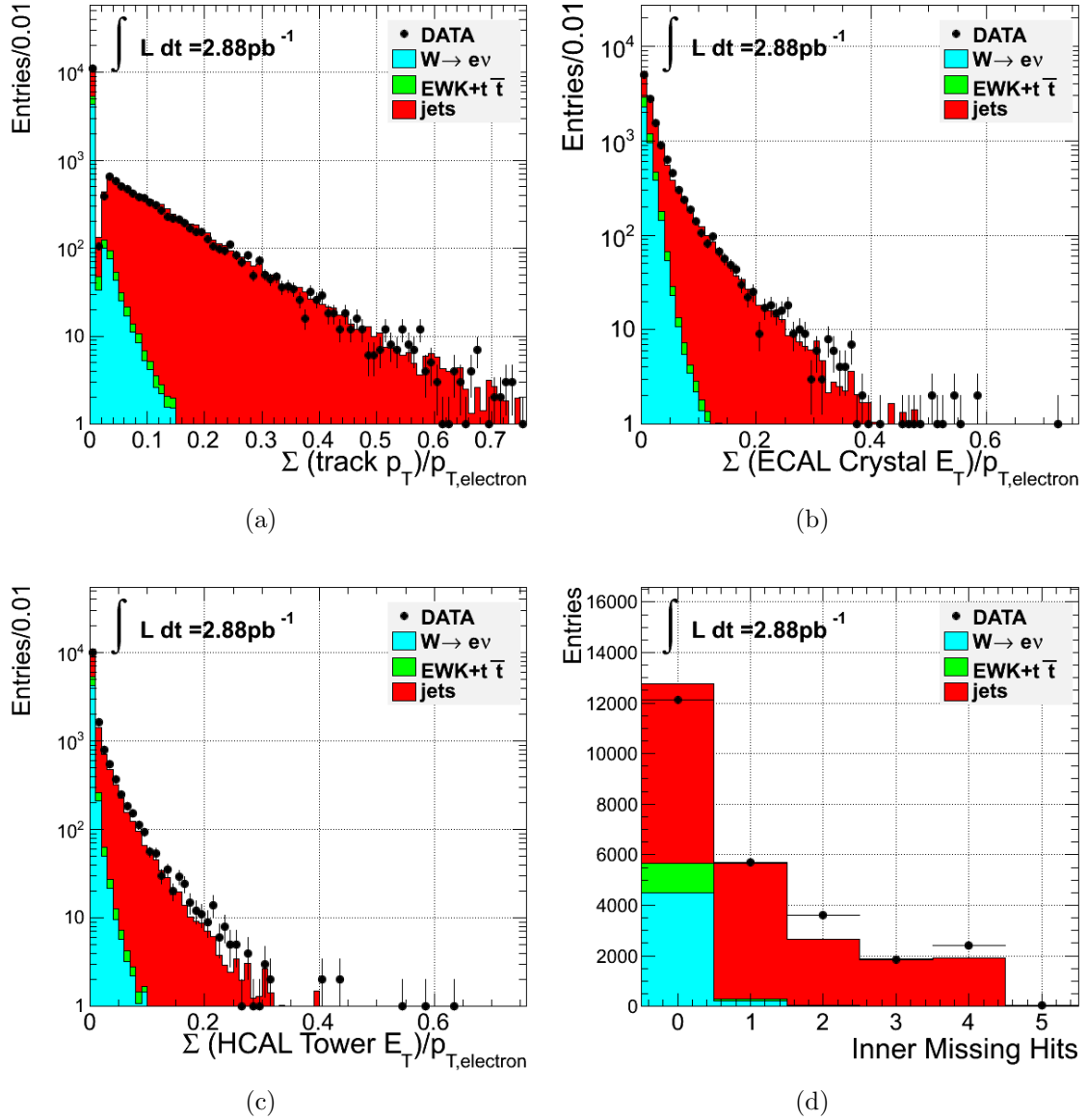


Figure B.6: Distributions of isolation variables and inner missing hits used in electron identification for electrons in the ECAL endcaps that pass the cuts of the WP80 selection excluding the cut on the variable that is being plotted. See Section 5.2 for details.